DEVELOPMENT OF DATA-DRIVEN CONSTITUTIVE MODELS FOR AEROSPACE MATERIALS



Burcu Tasdemir

Linacre College

University of Oxford

Department of Engineering Science

A thesis submitted for the degree of

Doctor of Philosophy

Trinity 2023

ABSTRACT

DEVELOPMENT OF DATA-DRIVEN CONSTITUTIVE MODELS FOR AEROSPACE MATERIALS

Tasdemir, Burcu

DPhil., Department of Engineering Science, University of Oxford.

Supervisor: Dr. Antonio Pellegrino

Co-Supervisor: Dr. Vito Tagarielli

August 2023, 137 pages

This study presents novel techniques to develop data-driven constitutive models. The adoption of data-based machine learning-driven models obtained from mechanical loading experiments allows for the accurate and computationally efficient prediction of the mechanical behaviour of materials eliminating the need for theoretical assumptions and potential constraints associated with traditional models.

The research is divided into four phases. In the first phase, uniaxial compression experimental data is used to develop surrogate models for the temperature and strain-rate dependent stress-strain response of a polymeric syntactic foam. In the second phase, the proposed techniques are applied to the history-dependent non-monotonic uniaxial

response of commercially pure titanium. The third phase introduces a strategy to formulate data-driven constitutive models from random multiaxial experiments. The obtained surrogate constitutive models are capable of capturing the in-plane stress response of isotropic, elastic-plastic materials loaded by combined normal and shear stresses. The feasibility of this approach is evaluated by conducting virtual experiments by means of Finite Element (FE) simulations in which a hollow, cylindrical, thin-walled test specimen is subjected to random histories of axial displacement and rotation. Finally, in the fourth phase, the methodology developed in the third phase is applied to the real experimental combined normal and shear response of aluminium specimens.

To validate the surrogate models, their predictions are compared against experimental data not used in the training process. The results demonstrate a very good agreement between the measurements and the predictions of the data-driven surrogate models.

In conclusion, this research proposes an innovative approach to data analytics and materials constitutive modelling based on machine learning techniques, offering significant potential to enhance the accuracy and efficiency of predicting the mechanical behaviour of aerospace materials.

Keywords: *Machine learning, Surrogate model, Plasticity, Data-driven, Constitutive models*

To my family…

ACKNOWLEDGMENTS

First and foremost, I would like to express my sincere gratitude to my supervisors, Dr. Antonio Pellegrino and Dr. Vito Tagarielli, for their invaluable support and guidance throughout my doctoral research. Without their tireless efforts, this work would not have been possible.

I am also thankful to my examiners, Prof. Barbara Rossi and Prof. Francesco Montomoli, for their time, valuable insights, and thoughtful suggestions.

I extend my heartfelt appreciation to my office mates, Yuan Xu, Gustavo Quino, Yue Chen, Govind Gour, Junyi Zhou, Huifang Liu, Kai Liu, and Longhui Zhang, for creating a positive work environment. Their friendship has made the long hours of research much more enjoyable.

Furthermore, I would like to acknowledge the Ministry of National Education of the Republic of Turkey for supporting my PhD research under the YLSY program.

I would also like to thank my besties Elif Alavanda and Buket Ikizoglu for their endless support and friendship.

Last but not least, I wish to express my deepest appreciation to my family, including my adorable cats Joey and Leblebi. My father, Adnan Taşdemir, and my mother, Menşure Taşdemir, have always been my unwavering support, providing me with strength and encouragement at every step of my life. Without their love and support, I could not have achieved my goals. Finally, I would like to thank my beloved sister and

best friend, Büşra Taşdemir, for her constant companionship and encouragement. And my tiny little brother Tolga Sarikaya.

Thank you all…

TABLE OF CONTENTS

ABSTRACT iii

ACKNOWLEDGMENTS vii

TABLE OF CONTENTS ix

LIST OF TABLES xiii

LIST OF FIGURES xiv

LIST OF ABBREVIATIONS xviii

1 INTRODUCTION 1

1.1 Motivation and Problem Definition 1

1.2 Objective 2

1.3 Approach and the Overview 3

2 LITERATURE REVIEW 7

2.1 Introduction to Machine Learning Techniques 7

2.2 Applications of Machine Learning to Materials Engineering 16

2.3 References 21

3 A DATA-DRIVEN RATE- AND TEMPERATURE-DEPENDENT CONSTITUTIVE MODEL OF THE COMPRESSION RESPONSE OF A SYNTACTIC FOAM 25

3.1 Introduction 27

3.2 Design and Analysis of the Mechanical Tests 29

3.2.1 Material and specimen geometry 29

3.2.2 Experimental Method 30

3.2.3 Experimental Results 33

3.3 Implementation of the Surrogate Models 36
3.3.1 Training data sets 36
3.3.2 Surrogate models 37
3.3.3 Assessment of the accuracy of the surrogate model 40
3.4 Results and Discussion 42
3.5 Conclusions 46
3.6 References 46
4 A DATA-DRIVEN MODEL OF THE YIELD AND STRAIN HARDENING RESPONSE OF COMMERCIALLY PURE TITANIUM IN UNIAXIAL STRESS51
4.1 Introduction 53
4.2 Mechanical Tests 55
4.2.1 Material and specimen geometry 55
4.2.2 Experimental setup and procedure 55
4.3 Implementation of the Surrogate Model 59
4.3.1 Training data set 59
4.3.2 Surrogate model 61
4.3.3 Assessment of the accuracy of the surrogate model 64
4.4 Results and Discussion 65
4.5 Conclusions 74
4.6 References 74
5 A STRATEGY TO FORMULATE DATA-DRIVEN CONSTITUTIVE MODELS FROM RANDOM MULTIAXIAL EXPERIMENTS 79
5.1 Introduction 81
5.2 Design and Analysis of the Virtual Experiments 83

5.2.1 Virtual test specimen 83
5.2.2 Finite Element analyses 84
5.3 Implementation of the Surrogate Models 86
5.3.1 Generation of the training data set 86
5.3.2 Separation of elastic and elastic-plastic increments 90
5.3.3 Surrogate models 91
5.3.4 Assessment of the accuracy of the surrogate models 96
5.4 Results and Discussion 98
5.5 Conclusions 100
5.6 Supplementary Material- Appendix 101
5.7 References 106
6 AN EXPERIMENTALLY GENERATED MACHINE LEARNING-BASED MATERIAL MODEL FOR NON-MONOTONIC AND NON-PROPORTIONAL LOADING 111
6.1 Introduction 113
6.2 Design and Analysis of the Mechanical Tests 116
6.2.1 Material and specimen geometry 116
6.2.2 Experimental setup and procedure 118
6.3 Implementation of the Surrogate Models 122
6.3.1 Training data set 122
6.3.2 Surrogate models 123
6.3.3 Assessment of the accuracy of the surrogate models 126
6.4 Results and Discussion 128
6.5 Conclusions 130

6.6 References 130

7 CONCLUSIONS 135

LIST OF TABLES

TABLES

Table 2.1 Loss Functions [6]-[7]. 13
Table 3.1 Number of tests performed for quasi-static and high-rate experiments. 33
Table 4.1 Kinematic/isotropic hardening model parameters. 71

LIST OF FIGURES

FIGURES

Figure 1.1 Summary of the scientific papers presented in the present integrated format thesis. 4
Figure 2.1. Structure of an ANN. 10
Figure 2.2. Comparison between the micro-model and the RNN model proposed by Ghavamian and Simone on load-displacement curves for different ranges of u [23].. 17
Figure 2.3. Comparisons between the material network proposed by Liu et al. and direct numerical simulations under the complex loading path shown in (a); stress-strain responses for three different materials (b), (c), and (d) [24]. 18
Figure 2.4. Example of strain versus time (a) and stress versus strain (b–d) histories for an elastic–plastic heterogeneous material [25]. 19
Figure 3.1. Specimen geometry and optical microscope image illustrating the microstructure of the syntactic foam. 30
Figure 3.2. Schematic of the Split Hopkinson pressure bar apparatus. 32
Figure 3.3. Summary of the experimental results obtained on the investigated epoxy syntactic foam: (a) temperature dependence of quasi-static and (b) high-rate mechanical responses; (c) rate dependence of room temperature compressive response; (d) attainment of dynamic equilibrium conditions; (e) densification strain and (f) absorbed energy density at densification for quasi-static and high-rate experiments conducted at different temperatures. 35
Figure 3.4. Experimental datasets utilised by the two data-driven models. Quasi static data, for surrogate model I (a) and II (b); high-rate data for surrogate model I (c) and surrogate model II (d). 38
Figure 3.5. Schematic of the two surrogate models. 39
Figure 3.6. Comparison between the predictions of the surrogate models and the experiments; (a) Model I and (b) Model II. (For Model I only 10% of the datapoints is shown for clarity) 41

Figure 3.7. Definition of densification strain and energy dissipation (a) and (b) results provided by the surrogate models. 44
Figure 3.8. Comparison of classical binning and specialised binning; (a) description and (b) predictions of model II for a high-rate experiment conducted at 75 °C. 45
Figure 4.1. Specimen geometry (all dimensions in mm). 56
Figure 4.2. (a) View of the experimental setup; (b) close-up of the specimen and loading fixtures. 56
Figure 4.3. (a) Example of a random imposed nominal strain history; (b) stress-strain behaviour measured during the corresponding random cyclic loading experiment. ... 58
Figure 4.4. A summary of the data used in this study. The measurements used for training and testing are shown in grey; the experiments used for validation are in red and blue. Only 20% of the datapoints is shown for clarity. 60
Figure 4.5. Evolution of the material's Young's modulus with increasing number of loading steps, for a selected experiment. 61
Figure 4.6. The evolution of NN inputs in a selected experiment (only the first 10 steps of the experiment are shown for clarity). 62
Figure 4.7. Comparison between the predictions of the surrogate model and the experiments; (a, b) validation set-1; (c, d) validation set-2. 64
Figure 4.8. Evolution in time increments and probability density distributions of (a, b) true stress, (c, d) total true strain, (e, f) accumulated plastic strain, (g, h) ε_{min}, ε_{max}, ε_{last}, and (i, j) increments of strain. 67
Figure 4.9. Armstrong and Frederik model: a) cyclically loaded specimen b) stress-strain response c) yield surface motion and expansion in the π plane. 69
Figure 4.10. Calibration experiments and predictions of the theoretical hardening model. 72
Figure 4.11. Comparison of the surrogate model and the cyclic hardening model of Abaqus. 73
Figure 4.12. Comparison of the errors of the surrogate and theoretical models..... 73
Figure 5.1. The geometry of the virtual specimen; (a) cross-sectional view; (b) 3-D view; (c) FE mesh and boundary conditions (all dimensions in mm). 85

Figure 5.2. (a) Example of a 16-step history of imposed random displacement and rotation; (b) corresponding path in strain space. 88
Figure 5.3. Visualisation of the training dataset (a) in strain space; (b) in stress space; (c) in axial stress versus strain space; (d) in shear stress versus strain space. Each of the fifty different loading paths is associated to a different colour according to the colour code displayed on the right.....89
Figure 5.4. PDF and CDF of the applied axial and shear strains. 90
Figure 5.5. Visualisation of the plastic increments in the training dataset (a) in strain space; (b) in stress space; (c) in axial stress versus strain space; (d) in shear stress versus strain space. Each of the fifty different loading paths is associated to a different colour according to the colour code displayed on the right.....92
Figure 5.6. Schematic of the two surrogate models. 93
Figure 5.7. (a) One of the random strain histories used to assess the surrogate models; (b) Stress history corresponding to the strain history in (a), including the predictions of the surrogate models; (c) normal stress versus strain history and predictions of the surrogate models; (d) shear stress versus strain history and predictions of the surrogate models.....97
Figure 5.8. (a) Strain histories corresponding to seven random simulations used to assess the surrogate models; (b) Stress history corresponding to the strain history in (a), including the predictions of the surrogate models; (c) normal stress versus strain history and predictions of the surrogate models; (d) shear stress versus strain history and predictions of the surrogate models. 99
Figure 6.1. Specimen geometry. 117
Figure 6.2. (a) View of the combined loading fixture; (b) CAD drawing of the combined loading fixture depicting the details. 118
Figure 6.3. (a) Example of a 10-step history of imposed random displacement and rotation; (b) corresponding path in strain space. 120
Figure 6.4. Visualisation of the plastic increments composing the training dataset and the validation experiments (a) in the strain space; (b) in the stress space; (c) in axial stress versus axial strain space; (d) in shear stress versus shear strain space. 121

Figure 6.5. Schematic of the surrogate model. 123
Figure 6.6. Stress-strain histories corresponding to the four validation experiments (two tension-torsion and two compression-torsion) used to assess the surrogate models; (a),(c),(e),(g) normal stress versus normal strain histories and predictions of the surrogate models; (b),(d),(f),(h) shear stress versus shear strain histories and predictions of the surrogate models. 127

LIST OF ABBREVIATIONS

ABBREVIATIONS

2D	Two-Dimensional
3D	Three-Dimensional
ANN	Artificial Neural Network
CDF	Cumulative Distribution Function
FE	Finite Element
MAE	Mean Absolute Error
ML	Machine Learning
MSE	Mean Squared Error
NN	Neural Network
PDE	Partial Differential Equations
PDF	Probability Density Function
PE	Plastic Energy
PINNs	Physics-Informed Neural Networks
ReLU	Rectified Linear Unit
RMSE	Root mean squared error
RVE	Representative Volume Element
SGD	Stochastic Gradient Descent
SHPB	Split Hopkinson Pressure Bar

CHAPTER 1

INTRODUCTION

This section serves as a comprehensive introduction to the PhD thesis being presented, covering essential aspects including the underlying motivation and problem statement, the primary objective, the approach adopted, the novel contributions, and an overview of the research structure. Furthermore, within the overview section, particular attention is given to highlighting the relevance of the four research papers that will be presented in the subsequent chapters of this integrated format thesis.

1.1 Motivation and Problem Definition

Machine learning is a branch of artificial intelligence (AI) that focuses on the development of algorithms and statistical models. It is based on the idea that computer systems can learn from data patterns and identify them without the need for any external description. The data-driven nature of artificial neural network models provides an opportunity for researchers to describe a functional relationship between the variables of interest, even in the absence of a comprehensive theoretical framework. This capability enables the modelling of complex phenomena that may be theoretically unknown.

The behaviour of engineering materials can exhibit significant complexity, especially when subjected to real operational loads. It encompasses diverse characteristics,

including temperature dependence, strain-rate dependence, anisotropy, moisture absorption, and more.

Consequently, traditional constitutive models developed can become exceedingly complicated and challenging to handle. In light of these complexities, an important question arises: Can the material behaviour be accurately predicted and reproduced using data-driven models fed by experimental data?

Data-driven models offer numerous advantages compared to classical theoretical models, with the direct utilization of experimental data being one of the most significant. This advantage enables accurate predictions of the mechanical behaviour of materials while reducing or eliminating the reliance on extensive theoretical assumptions.

1.2 Objective

The main aim of this study is to develop material models for different classes of materials and loading modes using machine learning techniques. The adoption of data-based machine learning-driven models obtained from mechanical loading experiments allows for the accurate and computationally efficient prediction of the mechanical behaviour of materials, removing the potential constraints of traditional models . This research introduces a novel approach to data analytics and materials constitutive modelling based on machine learning techniques fed with actual experimental data. The goal is to model the mechanical behaviour of engineering materials.

1.3 Approach and the Overview

The accurate modelling of the stress-strain characteristics of engineering materials has vital importance in structural design and optimisation analysis. However, formulating the mechanical response of materials is particularly challenging when they are exposed to complex environmental or loading conditions. The traditional material models available to engineers often rely on simplifying assumptions. Due to the complexities associated with non-monotonic or non-proportional plastic behaviour, temperature dependence, strain rate dependence etc., most of the existent models may have some limitations in predicting the actual behaviour of the material observed during experiments. Our approach is to model the actual material behaviour and its complexities using exclusively the results of carefully designed measurements, by applying supervised machine learning, eliminating the theoretical assumptions and difficulties associated with traditional material models.

Machine learning has been increasingly utilized in materials science and engineering to accelerate or enable complex material design and optimisation. Several researchers have introduced pioneering applications of machine learning in this field. Nevertheless, the existing literature still lacked data-driven material models that fully capture the genuine complexity of actual material behaviour, obtained directly from experimental measurements conducted under complex and realistic loading conditions.

To address this necessity, in this study, we propose a data-based approach for the modelling of:

1. Uniaxial monotonic response of syntactic foams,

2. Uniaxial non-monotonic response of metal alloys,

3. Multiaxial non-monotonic and non-proportional response of a virtual material, utilizing numerically produced data,

4. Multiaxial non-monotonic and non-proportional response of a metal, using actual experimental data.

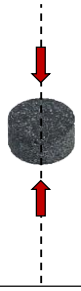
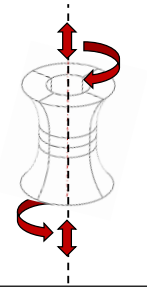
	Paper 1	***Paper 2***	***Paper 3***	***Paper 4***
Specimen:				
Data:	Experimental	Experimental	Numerical	Experimental
Loading:	Compression	Tension- Compression Cyclic	Tension- Compression- Torsion	Tension- Compression- Torsion
Rate:	High rate & Quasi-static	Quasi-static	Quasi-static	Quasi-static
Temperature:	-25,0,RT,50,75,100 °C	RT	RT	RT
Material:	Syntactic foam	Commercially Pure Titanium	Virtual material	Aluminium

Figure 1.1 Summary of the scientific papers presented in the present integrated format thesis.

The research is structured into four main chapters (given above) within the thesis, each of which serves as a standalone scientific paper. The intention behind this organization is to methodically incorporate the complexities associated with temperature and rate dependence, non-monotonic and multiaxial non-proportional loadings. By adopting a step-by-step approach, these four main chapters progressively introduce and examine

the intricacies involved. Figure 1.1 provides a summary of each paper, presenting pertinent details such as the data type, applied loading conditions, loading rate, temperature, and the materials investigated.

Paper 1 (Chapter 3) focuses on the modelling of the uniaxial monotonic response of a syntactic foam. This initial stage aimed at successfully predicting the temperature and strain rate dependant behaviour of the material under compression. Subsequently, the investigation progressed to encompass the modelling of non-monotonic, history-dependent material behaviour. The second paper (Chapter 4) specifically delved into modelling the uniaxial tension-compression cyclic response of commercially pure titanium.

Building upon the insights gained from the preceding papers, the research then incorporated the complexities of non-proportional axial-torsional combined loading. In the third paper (Chapter 5), a virtual material was employed to model the multiaxial non-monotonic and non-proportional response of a real sample, employing virtual experiments as a cost-effective and streamlined approach to develop the methodology before embarking on a multiaxial experimental campaign.

Having achieved favourable outcomes in the third paper, the developed methodology was subsequently applied to real experimental data in the fourth paper (Chapter 6). It is important to note that throughout these four papers, the methodologies have been constructed based on meticulous experimental measurements. Even in the case of paper three, where numerical data was employed, the methodology was deliberately designed to ensure applicability to experimental settings. In the thesis, each paper will be accompanied by its respective introduction within the dedicated chapters.

CHAPTER 2

LITERATURE REVIEW

This chapter aims to provide a comprehensive literature review, delving into various aspects of machine learning. It encompasses an examination of the fundamental principles and concepts of machine learning, along with its specific applications within the domain of materials science and engineering. Additionally, each subsequent paper chapter of this integrated format thesis will feature a focused literature review tailored to the specific subject matter.

2.1 Introduction to Machine Learning Techniques

Machine learning, a subset of artificial intelligence, provides algorithms that analyse and interpret patterns in the data using statistical methods. These algorithms are well known for their ability to automatically learn and progress from experience without human interaction.

Machine learning algorithms are commonly categorized into three main groups based on their learning processes and purpose of usage: supervised learning, unsupervised learning and reinforcement learning [1]. These categories correspond to different ways in which a machine can acquire knowledge.

Supervised learning requires the operator to provide the algorithm with labelled data, comprising input-output pairs that guide the learning process towards the desired

outcome. Its primary goal is to achieve generalization, enabling accurate predictions on unseen test input data. Supervised learning algorithms can be further classified into two subtypes: classification and regression. Classification is used to make decisions, while regression focuses on examining the relationship between variables [2].

On the other hand, unsupervised learning requires the algorithm to autonomously explore unlabelled data to discover patterns and structures independently. Its main objective is to cluster the data into meaningful categories, providing valuable insights.

Finally, reinforcement learning relies on the machine interacting with an environment and learning through trial and error. The algorithm receives feedback in the form of rewards or penalties, allowing it to improve its decision-making process over time. Initially, the model makes many mistakes but gradually learns to minimize errors based on positive and negative signals [2].

In this research, supervised learning was employed as the chosen approach, given that the primary objective is to develop surrogate models that accurately learn material behaviour based on experimental data. By utilizing supervised learning, it is possible to train the surrogate models using labelled data, where the input consists of the characteristics of the material, and the corresponding output represents its observed behaviour. The models will learn from this labelled data and subsequently make predictions for unseen data points.

Neural networks (NN) serve as the base of machine learning, mirroring the structural principles of the human brain. Similarly, to the biological neurons in the human brain, these networks are designed to process datasets, learning to recognize patterns within

the data and subsequently making predictions for unseen data instances. An artificial neural network (ANN) consists of key components: an input layer, one or more hidden layers, and an output layer. These layers are composed of artificial neurons, which perform computations to propagate information through the network. If an ANN contains two or more hidden layers, it is referred to as a "deep neural network". This architecture of the neural network, organized in layers, is also known as a feed-forward network [3].

Figure 2.1 provides an example of a neural network (NN) structure, consisting of six input neurons and two output neurons. This particular NN structure is depicted with two hidden layers. The hyperparameters in Figure 2.1 are chosen arbitrarily with the sole purpose of providing an example with a clear visualisation. It's important to note that the number of hidden layers and neurons within the network can be adjusted based on the judgement of the operator. The determination of the appropriate number of hidden layers and neurons is typically influenced by the complexity of the training dataset and often involves an iterative process of trial and error [4]. Researchers experiment with different configurations to find the optimal structure that yields a satisfactory performance for the specific task.

As illustrated in Figure 2.1, each neuron in a layer is connected to every neuron in the subsequent layer through artificial links. For instance, the inputs (x_1, x_2, ..., x_i) are connected to neuron "j" through individual links, each associated with a weight (w_{1j}, w_{2j}, ..., w_{ij}). These weights determine the strength and significance of the connections between neurons.

At each neuron, signals from all connected inputs are collected, and then each signal undergoes processing through various computations and activation functions to produce an output. This iterative process of signal propagation and transformation enables the network to learn and make predictions based on the provided input data.

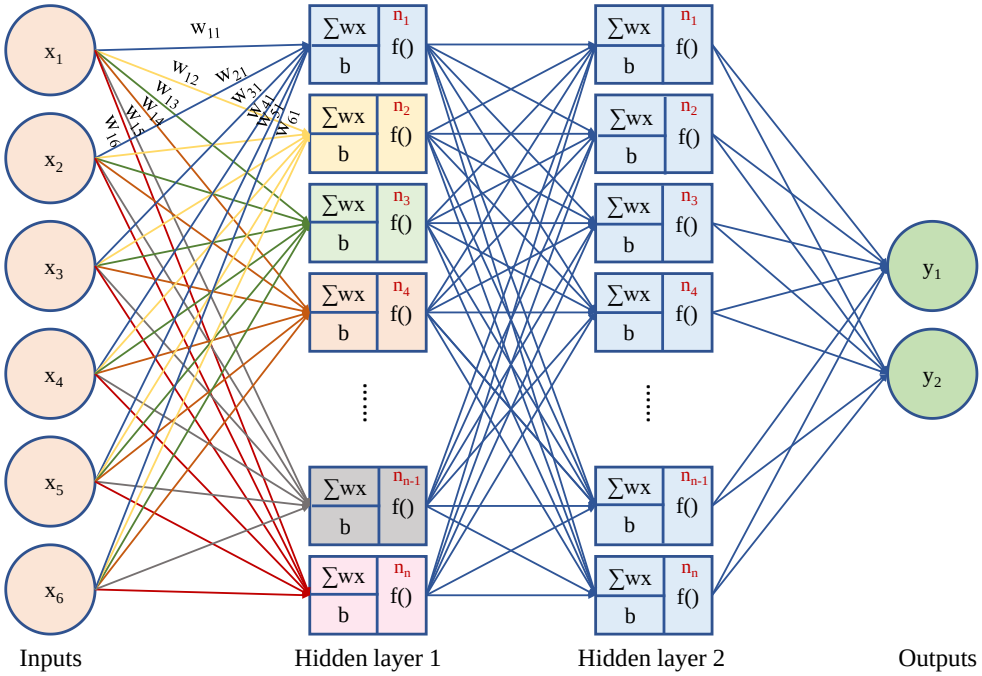


Figure 2.1. Structure of an ANN.

The functioning of each neuron in the hidden layers can be explained using simple mathematical logic. In a neural network, the parameters that govern the behaviour of each neuron are the weights (w_{ij}) and biases (b). When inputs are propagated through the network, they are distributed among the neurons in the hidden layers. Each input is multiplied by its corresponding weight and then combined with the bias term. The weights determine the influence of the input on the output of the neuron, representing the strength of the connection. The bias, on the other hand, acts as a constant value that helps offset the results toward the positive or negative side. It ensures that there is

always some level of activation in the neuron, even if the inputs are zero. By adjusting the biases, the neural network can introduce a certain level of bias towards specific outcomes or behaviours. The mathematical representation of the working principle of neural networks is given below [3].

$$Y = f_A\left(\sum(w.x) + b\right)$$

where Y denotes the output(s), f_A is the activation function, w is the weight matrix, x is the input(s) and b is the bias vector. To model non-linear problems, a non-linear function, known as the activation function, is applied to the linear combination of the parameters. This activation function introduces non-linearities into the neural network, allowing it to capture complex relationships and patterns in the data. The choice of the activation function depends on the nature of the data and on the specific problem. While there are various activation functions available, certain ones are used more commonly in neural network structures [5].

The sigmoid function maps the weighted sum of inputs to a range between 0 and 1. It is a non-linear, continuously differentiable, and monotonic function. However, it has some limitations. Firstly, it can be computationally expensive. Secondly, the sigmoid function suffers from an optimisation convergence issue named as the vanishing gradient problem. Since the output values are fixed between 0 and 1, the gradients can become extremely small, leading to slow convergence or no change during the learning process.

The hyperbolic tangent function (tanh) maps real values to the range between -1 and 1. It is zero-centred, unlike the sigmoid function. While the gradient of tanh is stronger

than sigmoid due to steeper derivatives, it still faces the issue of the vanishing gradient. The gradients can become very small for extreme input values, impacting the speed of the learning process.

The rectified linear unit (ReLU) is the most commonly used activation function. It is computationally efficient due to its simple formulation, and it converges faster. ReLU has a simple structure defined as max(0, x), and despite its name suggesting linearity, it is a non-linear function. ReLU does not suffer from the vanishing gradient problem, as long as the input is positive. However, a potential issue with ReLU is the occurrence of "dead ReLU" units. If the weighted sum of inputs is negative, ReLU always outputs 0, making the neuron inactive.

To address the "dead ReLU" problem, the leaky ReLU was introduced as a modification of ReLU. It allows a small, non-zero gradient for negative inputs, preventing neurons from becoming completely inactive. The leaky ReLU retains all the properties of ReLU but overcomes the "dead ReLU" issue. It is also possible to adjust the multiplication factors and create variations of the leaky ReLU.

The objective of a neural network algorithm is to minimize the prediction error by adjusting the weights and biases through a process called backpropagation [3]. The core component of this process is the minimization of a specific objective function known as the loss function, which quantifies the disparity between the predicted output and the actual output. Backpropagation is a fundamental technique employed in the training of feed-forward neural networks. It works iteratively adjusting the network's weights and biases based on the computed error between the network's prediction and the actual

output. During the forward pass, input data propagates through the network, sequentially activating neurons and generating the outputs. Subsequently, the backpropagation algorithm employs the chain rule of calculus to compute the gradients of the loss function with respect to the network's weights. These gradients provide guidance for updating the weights, enabling the network to progressively enhance its predictions through multiple training iterations. By iteratively adjusting the weights in a manner that minimizes the loss function, backpropagation facilitates the network's learning process and improves its performance over time.

For regression tasks, the focus is on evaluating the performance of the model in predicting continuous numerical values. Various regression loss functions are used to measure the discrepancy between the predicted and actual values. Some commonly used regression loss functions are listed in Table 2.1.

Table 2.1 Loss Functions [6]-[7].

Name of Loss Function	Formula
Mean Absolute Error (MAE)	$\frac{1}{n}\sum_{i=1}^{n}\lvert y_i - \hat{y}_i\rvert$
Mean Squared Error (MSE)	$\frac{1}{n}\sum_{i=1}^{n}(y_i - \hat{y}_i)^2$
Root Mean Squared Error (RMSE)	$\sqrt{\frac{1}{n}\sum_{i=1}^{n}(y_i - \hat{y}_i)^2}$

Mean absolute error (MAE) calculates the average absolute value difference between the predicted values and the actual values. It does not give extra weight to large errors as it directly uses the differences. In other words, MAE treats all errors equally, regardless of their magnitude. This characteristic of MAE may make it less sensitive to

outliers or extreme values in the data. Another popular choice for evaluating the prediction accuracy of neural networks is mean squared error (MSE) is. It takes the average of the squared differences between the predicted values and the actual values. By squaring the errors, MSE places greater emphasis on large errors compared to MAE. This property makes MSE more suitable for applications where large errors should be penalized more heavily in the overall loss calculation. Similarly, root mean squared error (RMSE) is closely related to MSE. RMSE is obtained by taking the square root of MSE. Like MSE, RMSE also emphasizes large errors, but it has the added advantage of providing a loss value in the same unit as the output variable. This characteristic makes it easier to interpret the magnitude of the error, as the RMSE value corresponds directly to the scale of the output variable [6-8].

These loss functions play a crucial role in machine learning as they quantify the quality of the predictions made by the trained model. A higher magnitude of the loss function indicates larger deviations between the predicted and actual values. By utilizing optimization algorithms, the model learns and adjusts its parameters to minimize the loss function, thereby reducing prediction errors.

Gradient descent is an optimization algorithm widely employed for the training of machine learning models and neural networks [2]. Stochastic gradient descent (SGD) is a type of gradient descent learning algorithm that instead of using the whole dataset at each iteration, selects only a single random training data point (or a small batch) to calculate the gradient and update the model parameters.

The Adam algorithm is an extension of the stochastic gradient descent and offers improved efficiency for training deep learning models [9]. The choice of the optimization function plays a crucial role in determining the training time required for the deep learning model. The Adam optimizer is recognized as one of the most efficient algorithms and has gained popularity in recent years for various deep-learning applications [10]. Its effectiveness lies in its ability to adaptively adjust the learning rate during training, making it well-suited for optimizing complex neural network architectures.

It is important to note that the smallest loss value does not always indicate the best model. Overfitting and underfitting are two common problems that can affect the accuracy and generalization ability of a trained model. Overfitting occurs when a model becomes overly complex and starts fitting the training data too closely, to the extent that it fails to generalize appropriately to unseen data. As a result, the model may exhibit very low error on the training data but higher errors on testing or validation data. This indicates that the model has learned the specific patterns and noise present in the training data instead of capturing the underlying general trends. Overfitting can lead to poor performance when applied to new data. On the other hand, underfitting occurs when a model is too simple to capture the underlying patterns and relationships in the data. An underfit model tends to have high errors not only on the training data but also on the testing data. It fails to capture the complexities and nuances present in the data, resulting in a lack of accuracy and predictive power [11]. Increasing the size of the training data set is indeed a helpful approach to mitigate overfitting, as it provides the model with more diverse examples to learn from.

When it comes to deep learning libraries, TensorFlow is a renowned and widely used open-source library developed by Google [12]. It has gained significant popularity in the machine-learning community due to its extensive capabilities and ease of use. In this research, TensorFlow 2.0 is specifically utilized for machine learning applications in the field of mechanics of materials.

2.2 Applications of Machine Learning to Materials Engineering

Machine learning has been applied to materials science and engineering to accelerate or enable complex material design and optimisation. Several researchers have used the machine learning approach in different areas of materials science and engineering including, among the others, the prediction of the multiaxial strain sensing response [13], and electrical conductivity [14] of multifunctional composites, identification of material properties and friction coefficient for sheet metal forming applications [15], flow behaviour of low alloy steel [16], temperature and rate dependent plasticity [17], or mechanical properties of composite materials [18]. Specifically, some pioneering research have proposed data-driven approaches as a valid alternative to classical constitutive modelling [19-22].

In addition to these applications, there are also some very relevant and noteworthy examples of the utilization of machine learning in materials modelling. These are briefly summarized below.

Ghavamian and Simone presented a methodology for acquiring stress-strain data from a micro level model utilised in multiscale simulations [23]. Their approach involved

training a recurrent neural network (RNN) model and subsequently integrating it into a finite element analysis routine. It was observed that the RNN model exhibited nearly impeccable predictions within the range of its training, as depicted in Figure 2.2 (a), (b), (c), and (d). However, outside of this range, the RNN model displayed reduced accuracy, as evidenced in Figure 2.2 (e). The authors concluded that the RNN model solely acquires and generalizes patterns within its training domain.

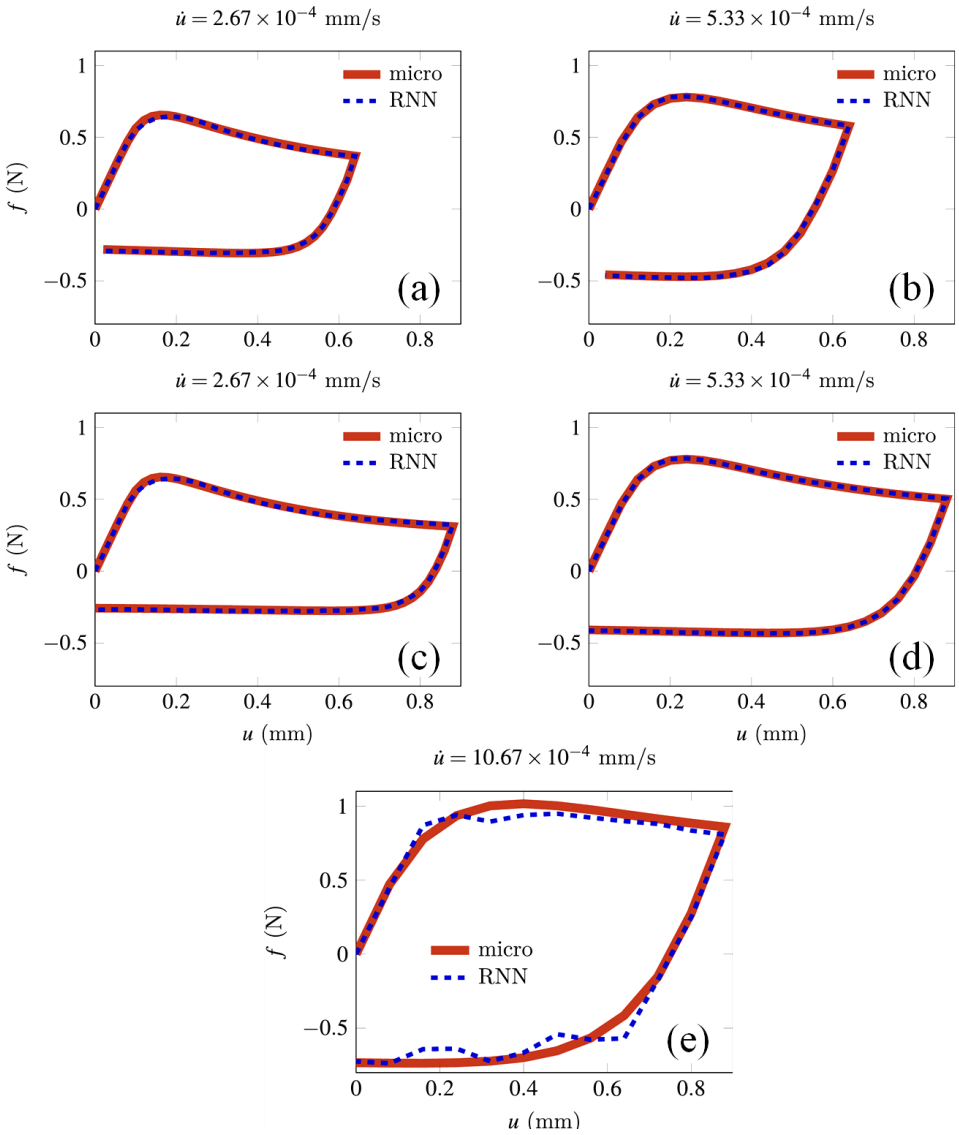


Figure 2.2. Comparison between the micro-model and the RNN model proposed by Ghavamian and Simone on load-displacement curves for different ranges of $\dot{u}$ [23].

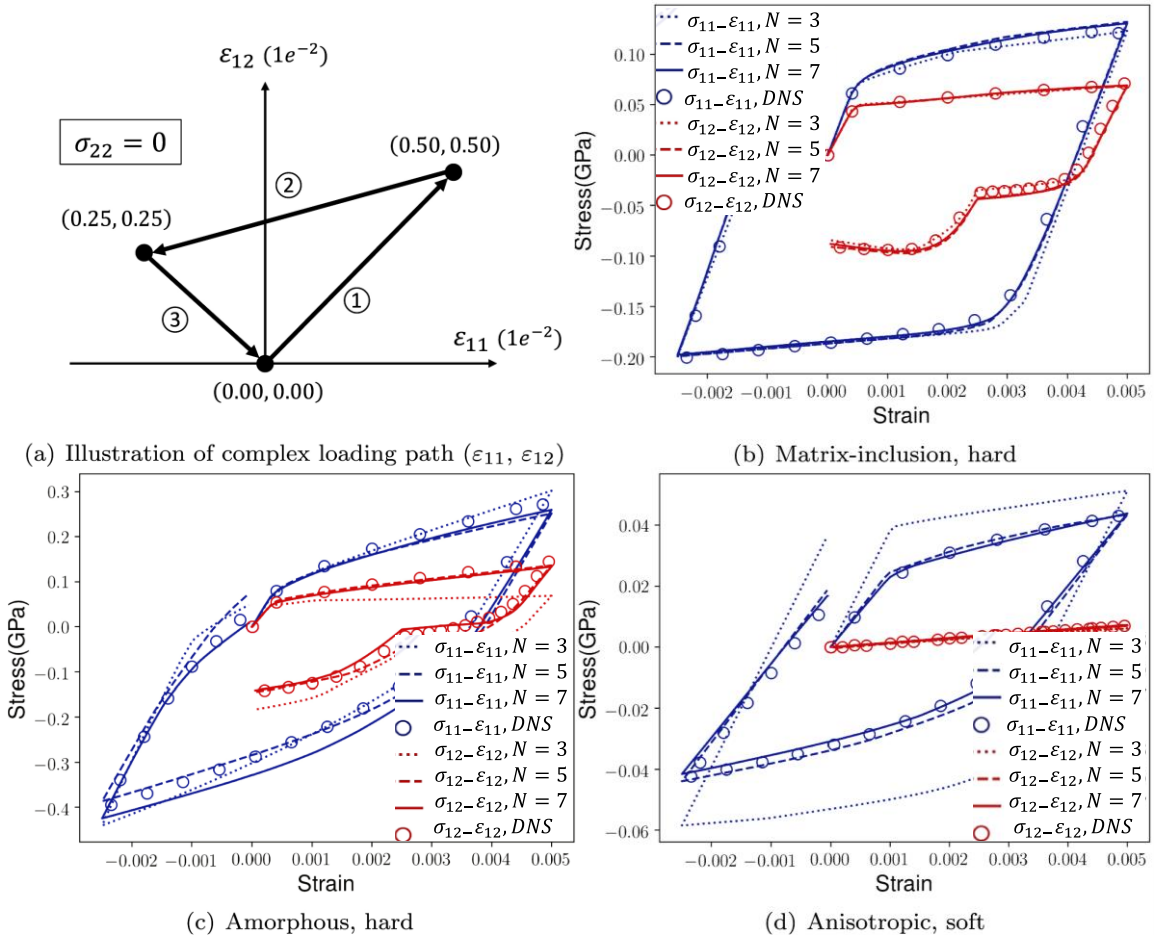


Figure 2.3. Comparisons between the material network proposed by Liu et al. and direct numerical simulations under the complex loading path shown in (a); stress-strain responses for three different materials (b), (c), and (d) [24].

Liu, Wu, and Koishi developed a data-driven multiscale material modelling method capable of predicting nonlinear material behaviours both accurately and efficiently by adopting a building block approach an advanced machine learning techniques [24]. Specifically, the authors examined the response of three RVEs with different phases along the 3-step loading path depicted in Figure 2.3(a) and compared the stress-strain

behaviour obtained using their model and direct numerical simulations. The resulting comparative analyses are presented in Figure 2.3 (b), (c), and (d).

More recently Ge and Tagarielli introduced a computational framework aimed at developing machine learning-based constitutive models for heterogeneous materials. In their study, they subjected volume elements to multiaxial random loads and employed neural networks to train constitutive models for heterogeneous composites with hyperelastic, viscoelastic, or elastic-plastic characteristics [25]. They compared their NN predictions with the ground truth represented by numerical simulations along complex loading paths, obtaining a very good agreement, as seen in Figure 2.4.

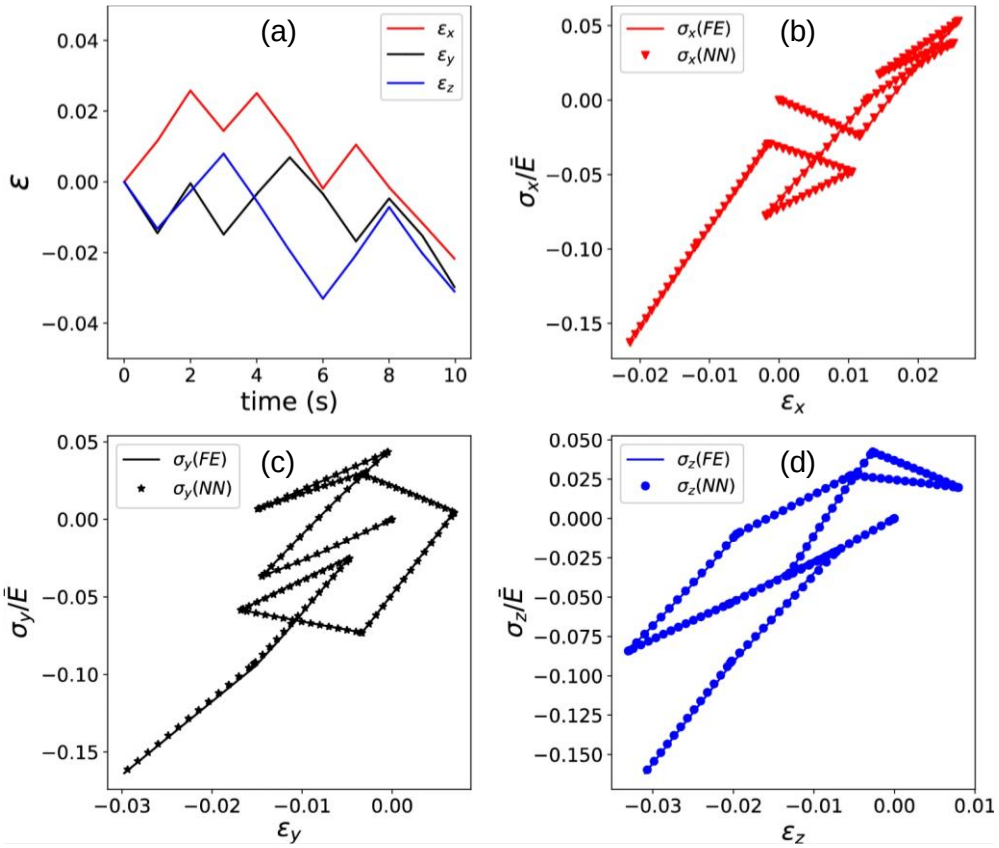


Figure 2.4. Example of strain versus time (a) and stress versus strain (b–d) histories for an elastic–plastic heterogeneous material [25].

All the aforementioned research shares a common characteristic: the training data utilized originates from numerical simulations rather than experimental observations. While these studies have achieved remarkable success and provided valuable insights, they do not utilize machine learning concepts and tools to develop data-driven models based on real experimental data and realistic loading scenarios.

The mechanical response of engineering materials is often affected by multiple variables such as the imposed rate of deformation, the previous strain history, the external temperature, other environmental variables such as moisture, chemical reactants, and their interaction. The sensitivity of the mechanical behaviour to the above variables is often complex and the dependency of the stress-strain characteristic on each of them can be coupled. A typical example is represented by the dynamic response of polymers and metal alloys subjected to impulsive loading. In this case their mechanical response is determined by the balance of two competing effects, the strain rate dependent hardening and the softening due to adiabatic heating.

It is therefore desirable to utilise machine learning to incorporate these effects, measured experimentally, into reliable and accurate models.

The primary objective of the research work presented in this thesis revolves around leveraging experimental data to construct accurate data-driven surrogate models. These models are created based on the actual behaviour of materials, obtained directly from precise measurements and observations.

By incorporating experimental data into the modelling process, our research aims to construct material models that exhibit enhanced realism, leading to improved efficiency and optimal designs for structural applications.

These concepts are applied to the temperature and rate dependent behaviour of polymer syntactic foams in paper 1 (chapter 3), to cyclic plasticity in titanium alloys in paper 2 (chapter 4) and to the non-monotonic, non-proportional multiaxial response of elasto-plastic solids in paper 3 (chapter 5) and paper 4 (chapter 6).

2.3 References

[1] Ayodele T.O., Types of machine learning algorithms. New advances in machine learning, 3, 19-48,2010.

[2] Goodfellow I., Bengio Y., Courville A., Deep Learning,Press, The M.I.T, 2016.

[3] Aggarwal C.C., Neural networks and deep learning. Springer, 10(978), 3, 2018.

[4] Ortiz-Rodriguez J.M., Martinez-Blanco M.A., Viramontes J.M.C., and Vega-Carrillo H., Robust Design of Artificial Neural Networks Methodology in Neutron Spectrometry, Kenji Suzuki, editor. Artificial Neural Networks – Architectures and Applications, Ch. 4, Publisher: INTECH; p.28., 2013.

[5] Nwankpa C., Ijomah W., Gachagan A., Marshall S., Activation functions: Comparison of trends in practice and research for deep learning, arXiv preprint arXiv:1811.03378, 2018.

[6] Wang Q., Ma Y., Zhao K. et al. A Comprehensive Survey of Loss Functions in Machine Learning. Ann. Data. Sci. 9, 187–212 ,2022.

[7] Pedregosa F., Varoquaux G., Gramfort A., Michel V., Thirion B., Grisel O., Blondel M., Prettenhofer P., Weiss R., Dubourg V., Vanderplas J., Passos A., Cournapeau D.,

Brucher M., Perrot M., Duchesnay É., Scikit-learn: Machine Learning in Python, J. Mach. Learn. Res., 12, pp. 2825-2830,2011.

[8] Nie F., Hu Z., and Li X., An investigation for loss functions widely used in machine learning, Communications in Information and Systems, 18(1), 37-52, 2018.

[9] Kingma D. P., Ba J.L., Adam: A method for stochastic optimization, ICLR 2015, 1412, 6980, 2014.

[10] Paoletti M.E., Haut J.M., Plaza J., and Plaza A., Deep learning classifiers for hyperspectral imaging: A review, ISPRS Journal of Photogrammetry and Remote Sensing, 158, 279-317, 2019.

[11] Data Science Notes5: Deep Learning: ANN (2020), Retrieved from: https://www.kaggle.com/ mrhippo/data-science-notes5-deep-learning-ann.

[12] Singh P., Manure A., Introduction to TensorFlow 2.0, Learn TensorFlow 2.0, Apress, Berkeley, CA, pp. 1-24.,2020.

[13] Matos M.A.S., Pinho S.T., and Tagarielli V.L., Application of machine learning to predict the multiaxial strain-sensing response of CNT-polymer composites, Carbon, 146, 265-275, 2019.

[14] Matos M.A.S., Pinho S.T., and Tagarielli V.L., Predictions of the electrical conductivity of composites of polymers and carbon nanotubes by an artificial neural network, Scripta Materialia, 166, 112-12, 2019.

[15] Zhaoa J. and Wang F., Parameter identification by neural network for intelligent deep drawing of axisymmetric workpieces, Journal of Materials Processing Technology, 166(3),387-391, 2005.

[16] Lin Y.C., Zhang J., and Zhong J., Application of neural networks to predict the elevated temperature flow behavior of a low alloy steel, Computational Materials Science, 43, 752-758, 2008.

[17] Li X., Roth C.C., and Mohr D., Machine-learning based temperature-and rate-dependent plasticity model: application to analysis of fracture experiments on DP steel, International Journal of Plasticity, 118, 320-344, 2019.

[18] Pathan M.V., Ponnusami S.A., Pathan J., Pitisongsawat R., Erice B., Petrinic N., and Tagarielli V.L., Predictions of the mechanical properties of unidirectional fibre composites by supervised machine learning, Scientific reports, 9(13964), 1-10, 2019.

[19] Kirchdoerfer T. and Ortiz M., Data-driven computational mechanics, Comput. Methods Appl. Mech. Engrg. 304, 81–101, 2016.

[20] Ibañez R., Borzacchiello D., Aguado J. V., Abisset-Chavanne E., Cueto El., Ladeveze P., and Chinesta F., Data-driven non-linear elasticity: constitutive manifold construction and problem discretization, Comput. Mech., 60 (5), 813–826, 2017.

[21] Tang S., Zhang G., Yang H., Li Y., Liu W. K., and Guo X., Map123: A data-driven approach to use 1d data for 3d nonlinear elastic materials modeling, Comput. Methods Appl. Mech. Engrg. 357, 112587, 2019.

[22] Stainier L., Leygue A., and Ortiz M., Model-free data-driven methods in mechanics: material data identification and solvers, Comput. Mech., 64,381-393, 2019.

[23] Ghavamian F., and Simone A., Accelerating multiscale finite element simulations of history-dependent materials using a recurrent neural network, 357,112594, 2019.

[24] Liu Z., Wu C.T., and Koishi M., A deep material network for multiscale topology learning and accelerated nonlinear modeling of heterogeneous materials, 345,1138-1168, 2019.

[25] Ge W., Tagarielli V.L., A computational framework to establish data-driven constitutive models for time- or path-dependent heterogeneous solids, Sci. Rep., 11 (15916), 2021.

CHAPTER 3

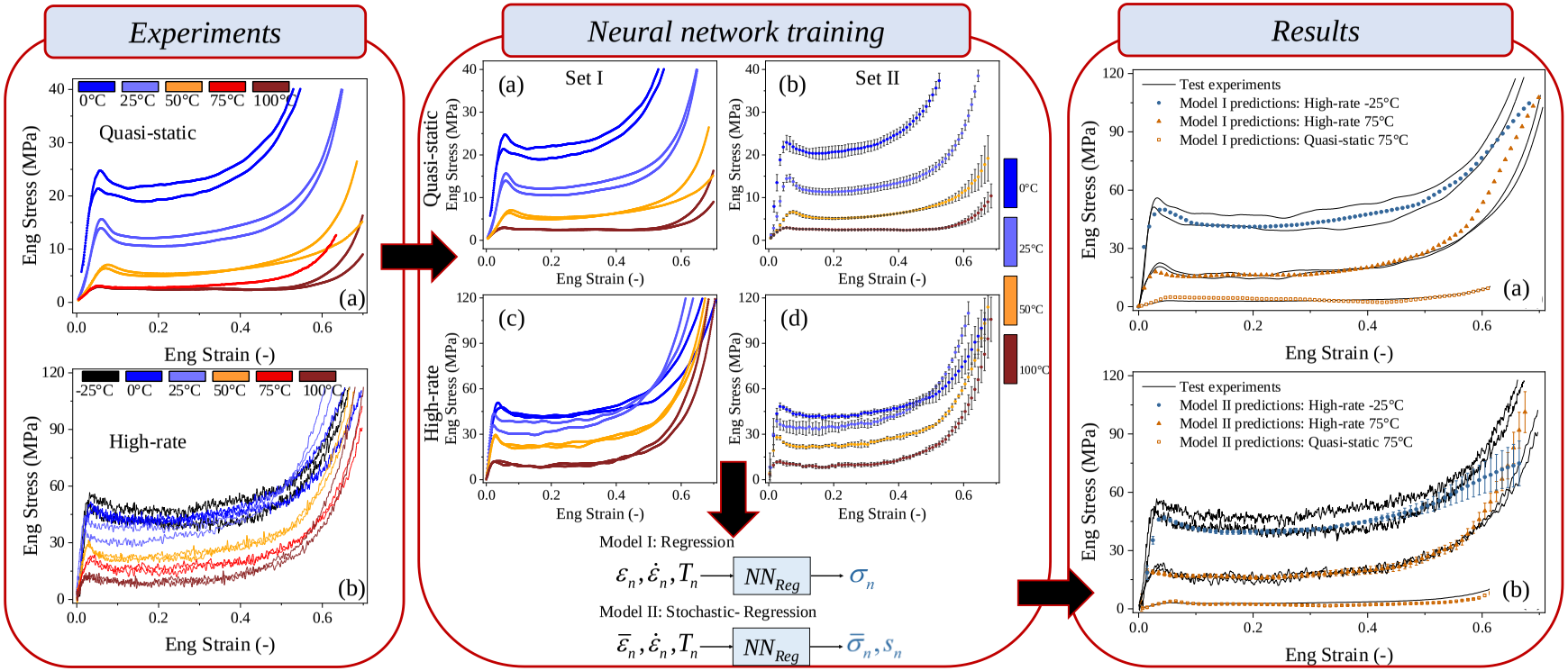
A DATA-DRIVEN RATE- AND TEMPERATURE-DEPENDENT CONSTITUTIVE MODEL OF THE COMPRESSION RESPONSE OF A SYNTACTIC FOAM

This chapter focuses on the modelling of the uniaxial monotonic response of a syntactic foam. The main novelty of this study is to provide a surrogate model, governed by experimental data, able to predict the exact material behaviour observed experimentally, including peak, collapse, plateau and densification regions for different temperatures and strain rates.

Abstract

This study presents a technique to develop data-driven surrogate models for temperature and strain-rate dependent stress-strain response of a polymeric syntactic foam. We comprehensively examine the effect of temperature and strain rate on the mechanical behaviour of an epoxy syntactic foam under compression. Polymeric syntactic foams are widely used in aerospace and submarine applications due to their low density, low moisture absorption, high strength, and stiffness. However, they are sensitive to changes in temperature, and their physical and mechanical properties can be significantly affected by temperature variations. To address this, an extensive experimental campaign was carried out at both quasi-static and high strain rates, over a temperatures range of -25°C to 100°C. The resulting dataset was used to develop data-driven surrogate constitutive models that can accurately capture the stress-strain behaviour of the

B. Tasdemir, V. Tagarielli, & A. Pellegrino, A data-driven rate- and temperature-dependent constitutive model of the compression response of a syntactic foam.



Keywords : Foams; Impact behaviour; Mechanical testing; Machine learning.

material. Two machine learning-based surrogate models were developed and compared. Additionally, methods for further improving their accuracy are suggested.

3.1 Introduction

Polymer syntactic foams are a kind of composites consisting of a polymer matrix and micro-balloons. The presence of hollow glass microspheres enhances their mechanical properties, their specific energy absorption and reduces the moisture intake due to the closed-cell structure of the hollow microspheres compared to conventional polymer foams [1]. These characteristics render them appropriate for implementation in the submarine, automotive, and aerospace industries. The mechanical behaviour of syntactic foams depends on the rate of deformation, owing to the inherent strain rate dependency of the polymer matrix and the dissipative nature of deformation and failure of the microspheres [2-4].

Several studies have been conducted to investigate the dynamic behaviour of syntactic foams at room temperature [5-9]. However, syntactic foams are used in a wide range of environmental conditions, including extreme temperatures, due to their thermal insulation properties [10-11]. Due to the temperature sensitivity of the polymer matrix [12], the physical and mechanical behaviours of these foams are highly sensitive to temperature changes. Therefore, investigating the temperature dependence of their properties is of critical importance.

In this study, we model the strain rate and temperature-dependent response of an epoxy syntactic foam under compression, using exclusively the results of experimental

measurements over a range of temperatures between -25°C and 100°C, by applying supervised machine learning. Machine learning has found various applications in the field of solid mechanics with the purpose to accelerate or enable complex material design and optimization. These applications include, among the others, the development of constitutive models for metallic materials [13-14], reverse engineering [15], structure generation [16] of additively manufactured materials as well as modelling and design of composite materials [17]. However, the existing literature does not include any application of machine learning aiming at predicting the temperature and strain rate-dependent response of syntactic foams.

This study presents an extensive investigation into the mechanical behaviour of an epoxy-based syntactic foam. The investigation focuses on the combined effects of temperature and strain rate during compression loading. The study examines both quasi-static and high strain rate conditions. The range of temperatures considered spans from -25°C to 100°C. The data from experiments are utilised to construct a surrogate model that captures the mechanical response of the syntactic foam for different ranges of temperatures and strain rates. The proposed technique can be applied to any solid material; however, a syntactic foam is chosen for this study due to its wide availability, extensive industrial usage, and significant dependence on temperature and strain rate. Feed-forward Neural Networks (NNs) are used to construct rate and temperature dependant surrogate models of high accuracy that are independent of any theoretical assumptions on the mechanical response of the material. We use the surrogate models to predict the stress consequent to the application of a strain under quasi-static or high strain rates over a wide range of temperature values.

The paper is structured as follows. In Section 3.2 we illustrate the details of the employed experimental method and the corresponding experimental results, while Section 3.3 presents the implementation of the data-driven surrogate models; the results of the proposed surrogate models are presented and discussed in Section 3.4.

3.2 Design and Analysis of the Mechanical Tests

3.2.1 Material and specimen geometry

The material investigated is an epoxy-based syntactic foam, made of microspheres with a diameter ranging from 15 to 60 μm, an average wall thickness of 0.8 μm, and a volume fraction equal to 0.5. The microstructure of the foam was visualized by cutting a small block of material to expose the microspheres. A compressed air diffuser was used to minimize the dust on the surface for clear visualization. The microstructure, captured utilising a ZEISS Axio Lab.A1 optical microscope, is shown in Figure 3.1. Microbubbles of varying sizes are clearly observable in the micrograph; their dimensions are consistent with the expected sizes reported in the datasheet of the material.

Samples of circular cylindrical shape with a diameter of 5 mm and height of 2.5 mm were used for high-rate and quasi-static compression experiments (Figure 3.1). Previous research indicated that the optimal aspect ratio (the ratio of height to diameter) for compression specimens should be between 0.5 and 1 [18]. The lower bound of this range is adopted to favour the attainment of dynamic force equilibrium conditions and increase the achievable strain rates.

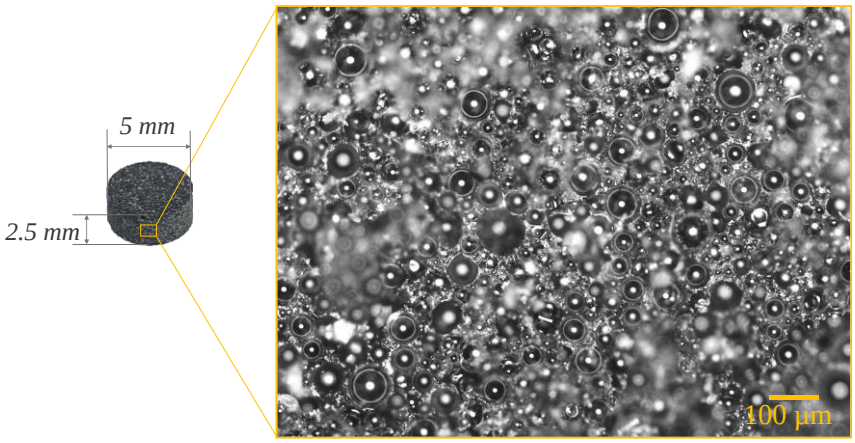


Figure 3.1. Specimen geometry and optical microscope image illustrating the microstructure of the syntactic foam.

3.2.2 Experimental Method

3.2.2.1 Quasi-static set-up

The cylindrical syntactic foam specimens were speckled, and the quasi-static experiment were recorded by a high-resolution camera (JAI BM-500GE monochrome progressive scan camera) to measure the deformations. The quality of the speckle pattern was verified using the mean intensity gradient (MIG) [19,20]. The obtained MIG values were between 35 and 37, ensuring a mean bias error of displacement of less than 1% [19]. The specimens were loaded by a screw-driven testing machine (Zwick Z250) via compression fixtures. A lubricant was used to minimize the effect of friction between the anvils and the sample. The uniaxial compression experiments were conducted under displacement control at a nominal strain rate 10-3 s-1 in all tests. The compressive forces were measured using a 20 kN load cell. The strain histories were analysed using the GOM Aramis DIC software.

The temperature dependence of the mechanical responses of the syntactic foam was examined at temperatures ranging from 0℃ to 100℃. These temperatures were chosen based on the typical service and glass transition temperatures of the selected syntactic foam. The ambient temperature was regulated using a feedback-controlled environmental chamber, while sub-ambient temperatures were achieved by connecting a liquid nitrogen dewar to the inlet of the chamber. The flow rate of the liquid nitrogen was automated, and the temperature was monitored using a built-in thermocouple and an additional type-K thermocouple positioned in close proximity to the specimen. Once the target temperature was reached the sample was left in the chamber for an additional 20 minutes to reach temperature equilibrium prior to compression.

3.2.2.2 High-rate set-up

The assessment of the high-rate response of polymeric syntactic foams presents unique challenges both in terms of their mechanical response and acoustic properties. To begin with, the compression of the specimens beyond their densification strain requires the generation of stress pulses with relatively long duration, particularly for ductile polymer foams. To fulfil this requirement, the high-rate compression experiments were conducted using a Split Hopkinson Pressure Bar (SHPB) [21] setup, which can produce stress pulses lasting longer than 1.1 ms. The incident and transmitted bars were made of titanium 6Al4V with solid circular cross-sections of 16 mm in diameter. The length of the input bar, output bar, and striker was equal to 2.7 m, and they were supported by low-friction bearings spaced 300 mm apart. The superposition of incident and reflected elastic stress waves into the input bar at the gauge location becomes inevitable when

the projectile length matches the input bar length. Consequently, it becomes challenging to directly differentiate between the incident and reflected waves based on strain measurements alone. To address this issue, a data analysis technique was employed, utilizing the method of characteristics and D'Alambert's solution of wave equations. This approach allowed determining the magnitude of forward and backward travelling waves at the interfaces between bars and specimen over time. Further details regarding the procedure can be found in [22]. Additionally, polymer-based materials have low-stress wave propagation, making it challenging to achieve dynamic equilibrium conditions. This was facilitated by interposing 1 mm thick cardboard pulse shapers (436 g/m2) between the striker and the input bar. A schematic of the setup used during the experiments, analogous to that utilised in [23], is shown in Figure 3.2. The temperature dependence of the high-rate mechanical response of the syntactic foam was examined at temperatures ranging between -25℃ and 100℃. The ambient temperature was regulated using a bespoke feedback-controlled environmental chamber (schematic in Figure 3.2) following a procedure analogous to that employed during the quasi-static experiments.

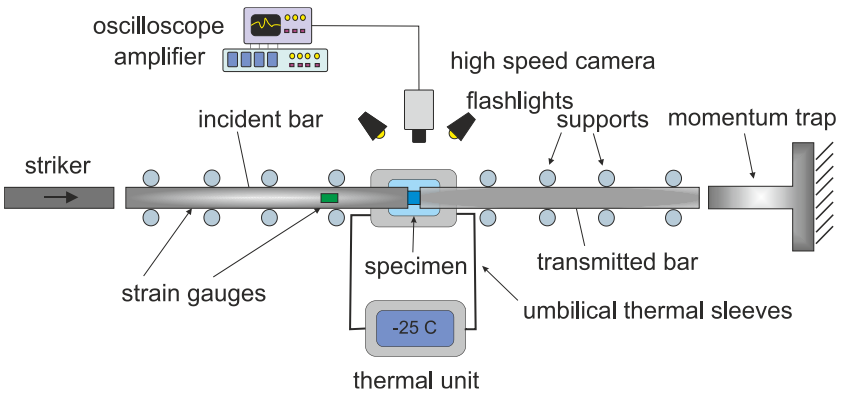


Figure 3.2. Schematic of the Split Hopkinson pressure bar apparatus.

3.2.3 Experimental Results

A total of twelve high-rate and nine quasi-static experiments were conducted over a temperature range of -25°C to 100°C, as given in Table 3.1, detailing the number of repetitions. Two experiments were conducted for each loading case except for the quasi-static experiments conducted at of -25°C and 75°C due to limited sample availability.

Table 3.1 Number of tests performed for quasi-static and high-rate experiments.

	-25 °C	**0 °C**	**25 °C**	**50 °C**	**75 °C**	**100 °C**
Quasi-static	0	2	2	2	1	2
High-rate	2	2	2	2	2	2

Figure 3.3 presents the obtained experimental results. The temperature dependence of the quasi-static and high-rate compressive response of the material is depicted in Figure 3.3 (a) and (b), respectively. The experimental results show an evident temperature dependence of the compressive response for the epoxy-based syntactic foam. The compressive strength reduces from 14.8±1 MPa to 2.9±0.1 MPa from room temperature to 100°C; and increases to 23.1±2 MPa at 0°C for quasi-static loading. Similarly, high-rate experiments show that compressive strength reduces from 39.7±3 MPa to 12.1±0.1 MPa from room temperature to 100°C; and increases up to 49.2±2 MPa and 53.6±2 at 0°C and -25°C, respectively.

Figure 3.3 (c) illustrates the mechanical responses measured at room temperature at quasi-static and high-rate of strain. The material exhibits an evident rate dependency of

the compressive strength and initial stiffness. The compressive strength increases from 14.8±1 MPa to 39.7±3 MPa as the strain rate increases from 10^{-3} s^{-1} to approximately 2500 s^{-1}. Furthermore, it is evident that the epoxy-based syntactic foam displays the characteristic response of an elastic-plastic cellular material, manifesting distinct regions of elastic, plateau, and densification. It is characterised by ductile behaviour with an extensive plateau region prior to the onset of densification.

The validity of the experimental results obtained at high strain rate is supported by the achievement of dynamic force equilibrium conditions. These were attained for all experiments reported in this study. Figure 3.3 (d) shows the incident and transmitted forces and the strain rate history measured during a representative dynamic experiment conducted at room-temperature. It is apparent that the conditions of dynamic equilibrium were attained during the initial stages of deformation and that the strain rate was approximately constant in the plateau region, until densification.

Figure 3.3 (e) and (f) analyse and compare the densification strain and the absorbed energy density at densification measured at different temperatures and strain rates. The experimental findings suggest that densification strain does not exhibit any noticeable dependence on temperature or strain rate. In contrast, the absorbed energy density displays a clear dependence on both temperature and strain rate, with a discernible trend displayed on the plotted data. The experimental results indicate that the absorbed energy density in high-rate experiments is nearly twice that of quasi-static experiments, and it exhibits a decreasing trend with increasing temperature for both high-rate and quasi-static loadings.

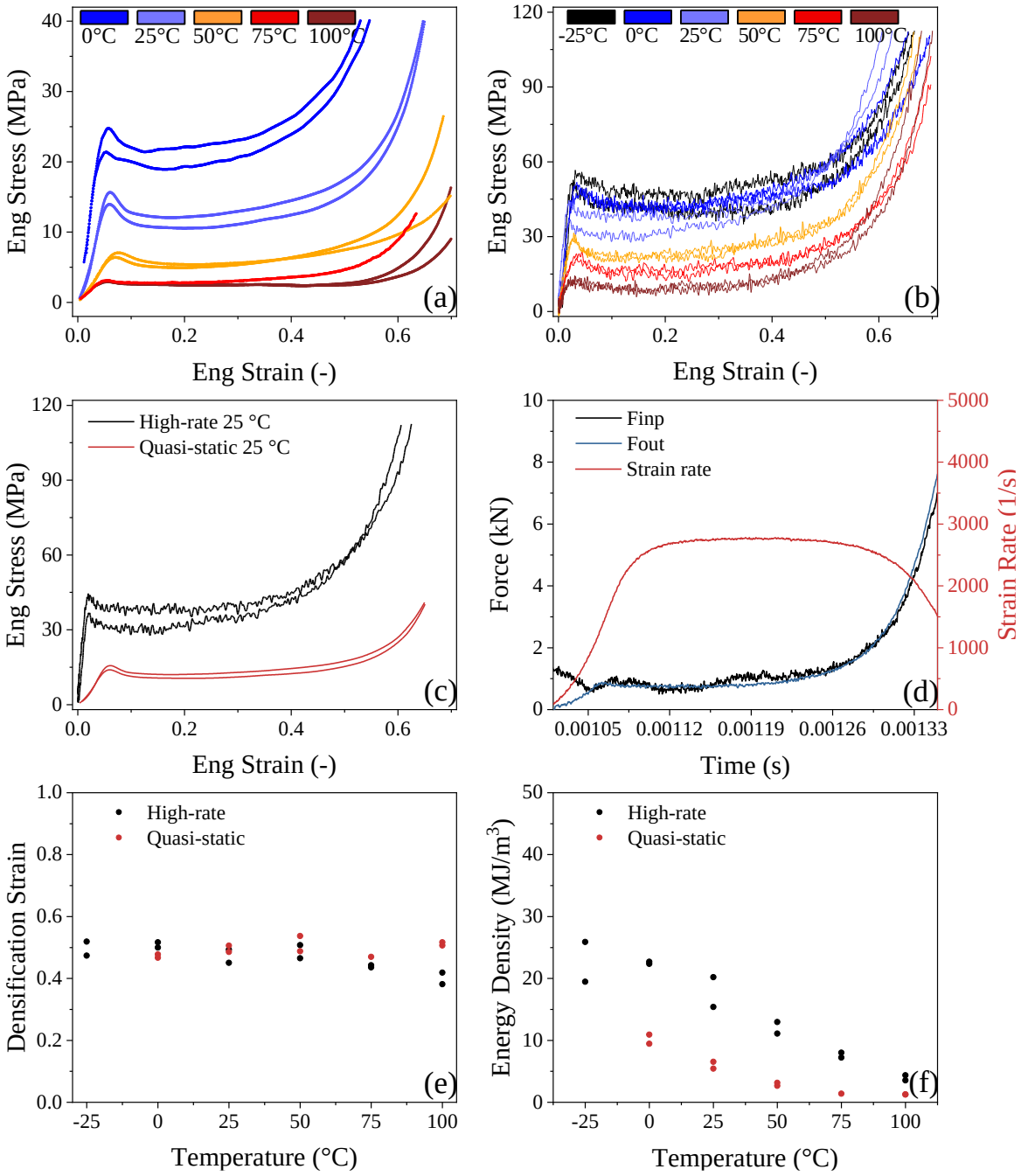


Figure 3.3. Summary of the experimental results obtained on the investigated epoxy syntactic foam: (a) temperature dependence of quasi-static and (b) high-rate mechanical responses; (c) rate dependence of room temperature compressive response; (d) attainment of dynamic equilibrium conditions; (e) densification strain and (f) absorbed

energy density at densification for quasi-static and high-rate experiments conducted at different temperatures.

3.3 Implementation of the Surrogate Models

3.3.1 Training data sets

Eight quasi-static and eight high-rate experiments were utilised to assemble training datasets for the development of two data-driven surrogate models. These experiments were conducted at 0°C, 25°C, 50°C, and 100°C and were repeated twice for each of the temperature and strain rate combinations as shown in Figure 3.3 (a) and (b). The remaining five experiments (carried out at -25°C and 75°C, Table 3.1) were stored to perform a validation of the predictions provided by the developed surrogate model.

Two surrogate models were developed with two different sets of data by using the same experiments. The first surrogate model provides stress outputs for different combinations of temperature, strain, and strain rate. The second surrogate model utilises the information enclosed in the experimental scatter of measured data to output the envelope of possible stresses for each combination of the same variables.

Figure 3.4 illustrates the training data set 1 and 2 used for the development of the surrogate model 1 and 2, respectively. Quasi-static and high-rate experiments are shown separately for both datasets for clear visualisation, however they were used together for the training.

Training set-1 was assembled using the original experimental stress-strain histories (shown in Figure 3.3 (a) and (b)) with the relevant strain-rate and temperature inputs. The data was smoothed using the adjacent-averaging signal processing method with the point of window 20. The final smoothed dataset is shown in Figure 3.4 (a) and (c). The data set comprised 13600 data points with a similar amount of data points for each experiment.

Training set-2 was assembled as a stochastic dataset to carry information on the variance of the stress histories for prescribed strain intervals. The original data (shown in Figure 3.3 (a) and (b)) was divided into strain intervals of 0.01. For each of these, mean strain, mean stress and the standard deviation of the stress were calculated. The dataset, shown in Figure 3.4 (b) and (d), was assembled with the error bars representing the stress variation in each strain interval, considering two repeated experiments for each temperature and strain-rate. The data set comprised a total of 521 data points, with a similar amount of data points (60-70) for each experiment.

The main purpose of this method was to store and utilise all the useful information, including the scatter, that comes from the experimental data. The accuracy can be increased by increasing the number of repetitions of the experiments.

3.3.2 Surrogate models

Feed forward neural networks (NNs) [24] were used to construct data-driven surrogate models based on the data presented in the previous section. Two different surrogate models are presented, and their architecture is summarised in Figure 3.5. Both models

perform a regression, however, they use different sets of data with different inputs and outputs. Model I uses direct strain values as input along with the temperature and the strain rate, providing the value of the direct stress as the output. On the other hand, Model II uses a stochastic dataset with mean strain as input, along with the temperature and strain rate, and provides mean stress and standard deviation of stress as outputs.

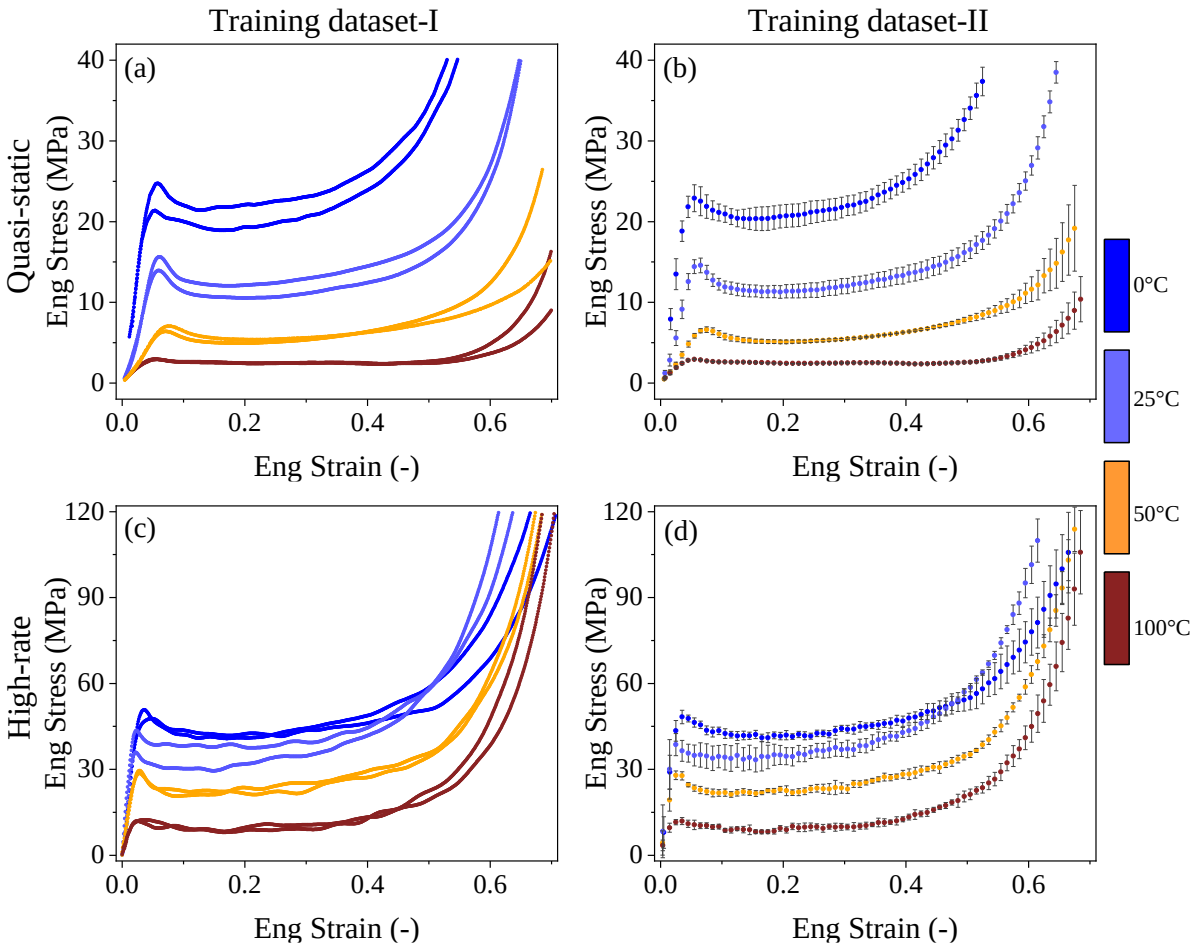
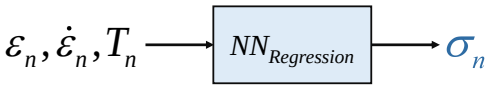


Figure 3.4. Experimental datasets utilised by the two data-driven models. Quasi static data, for surrogate model I (a) and II (b); high-rate data for surrogate model I (c) and surrogate model II (d).

Model I: Regression



Model II: Stochastic- Regression

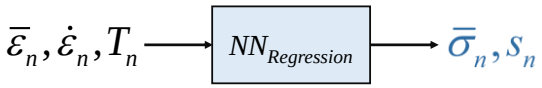


Figure 3.5. Schematic of the two surrogate models.

Model I performs the regression

$$(\sigma) = NN_R(\varepsilon, \dot{\varepsilon}, T). \quad (1)$$

Where σ represent the current stress state of the material while ε is the current strain, $\dot{\varepsilon}$ is the strain rate and T is the temperature.

Model II performs the regression

$$(\bar{\sigma}), (s) = NN_R(\bar{\varepsilon}, \dot{\varepsilon}, T). \quad (2)$$

Where $\bar{\sigma}$ represent the mean stress and s represents the standard deviation of the stress for the corresponding strain interval, as described in the previous section, while $\bar{\varepsilon}$ is the mean strain, $\dot{\varepsilon}$ is the strain rate and T is the temperature. The standard deviation of stress in each strain bin quantifies the envelope of possible stresses, by taking into account the useful information contained in the noise within the experimental data as well as in the multiple repetitions of the experiments.

The architecture of both the surrogate models were determined by trial and error; they comprised 2 hidden layers containing 100 and 64 neurons each for Model I and Model

II, respectively. The inputs and outputs were rescaled to values between 0 and 1 using the Minmax() function [25]; the ReLU [26] function was chosen as the activation function for the hidden layers, while the identity function was used for the output layer (i.e. no activation). The chosen loss function was the mean squared error (MSE) [25]. The NN was trained in TensorFlow 2.6 [27] via backpropagation, using the Adam optimiser [28] with a learning rate of 0.001. The number of epochs was set to 1,000, with a batch size of 400 for the Model I, while it was set to 2500 with a batch size of 26 for the Model II. The difference between the architecture of the two surrogate models was mainly caused by the different sizes of the data sets (specified in Section 3.3.1). The training data (shown in Figure 3.4) was split into two subsets for both models; one subset contained 90% of the total number of datapoints and was used for training, while the remaining data points (10% of the total) were used for testing.

3.3.3 Assessment of the accuracy of the surrogate model

To test the fidelity of the surrogate models, the data recorded in further 5 experiments (carried out at temperatures of -25°C and 75°C with the specified repetitions in Table 3.1) were stored as unseen data. These were processed as the remaining experiments, with the same methods utilised for Model I and Model II, to be used separately for the assessment of the accuracy of both surrogate models. The surrogate models were used to predict the stress versus strain responses corresponding to these five unseen strain histories. For each history, starting from the initial stress and strain free configuration ($\varepsilon = \sigma = 0$), the sequence of consecutive strain increments was provided as an input to the surrogate model along with the strain rate and temperature information. In each

increment, eqn. (1) and eqn. (2) were used to obtain the stress σ and $\bar{\sigma}$ with s for Model I and Model II, respectively. This allowed constructing predictions of the stress histories corresponding to the five unseen strain histories.

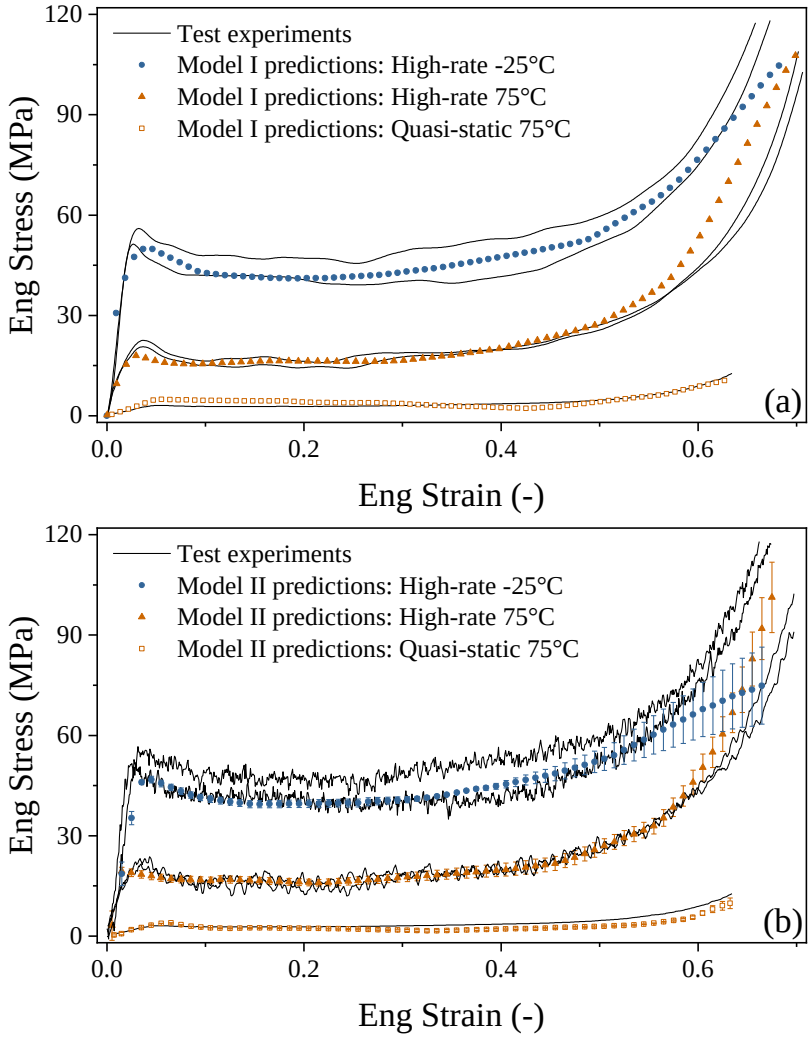


Figure 3.6. Comparison between the predictions of the surrogate models and the experiments; (a) Model I and (b) Model II. (For Model I only 10% of the datapoints is shown for clarity)

3.4 Results and Discussion

Figure 3.6 compares the predictions of the surrogate models to the five unseen experiments mentioned in the previous section, in terms of the stress versus strain response. The five experiments are grouped into three prediction families: the high-rate experiments conducted at 25 °C, the high-rate experiments carried out at 75 °C, and the quasi-static experiments conducted at 75 °C, as high-rate experiments are repeated twice. Figure 3.6 (a) presents the predictions of Model I. Figure 3.6 (b) presents the predictions of Model II with the experimental data in smoothed and noisy forms consistent with the information carried into training data set.

The surrogate models are found to be in good agreement with the experiments, accurately predicting the temperature and strain-rate dependent stress-strain characteristics of the material until densification in all three cases. Both surrogate models successfully predict the characteristic response of the epoxy-based syntactic foam, displaying distinct regions of elastic, plateau, and densification. It should be noted that although the -25°C high-rate experiment is outside of the training data set range, both surrogate models achieve reasonable accuracy in their predictions, extrapolating accurate stress outputs beyond the range of conditions included in the training dataset.

Both surrogate models are capable of predicting the clear transition between the plateau and the densification regimes for all cases, as seen in Figure 3.6. The densification strain is defined by the maximum energy absorptions efficiency (η) as given below [29-30], and schematically described in Figure 3.7 (a).

$$\eta = \frac{1}{\sigma(\varepsilon)} \int_0^{\varepsilon} \sigma(\varepsilon) d\varepsilon. \quad (3)$$

The densification strain and energy density at different temperatures and strain rates were analysed and compared for all performed experiments in Figure 3.3 (e) and (f). Figure 3.7 (b) compares the predictions given by the surrogate models with the validation experiments in terms of densification strain and energy density. It can be concluded that Model I outperforms Model II in both densification strain and energy density predictions for all three cases. Furthermore, the accuracy of the predictions for the high-rate experiments was found to be higher compared to the quasi-static case. This can be attributed to the clearer transition observed between the elastic, plateau, and densification regions in high-rate experiments. Specifically, the peak and collapse regions were found to be more distinct in high-rate experiments compared to quasi-static experiments.

To enhance the accuracy of Model II in the elastic-peak-collapse ($0 \leq \varepsilon \leq 0.1$) and post-densification ($\varepsilon \geq 0.5$) areas, a specialised binning method was employed. The primary objective was to reduce the dominating influence of the plateau regime in the training data. The classical binning method divided the data into evenly spaced strain intervals (0.01), as described in Section 3.3.1. However, the specialized binning method used a varying interval strategy for the elastic-peak-collapse ($0 \leq \varepsilon \leq 0.1$) and post-densification ($\varepsilon \geq 0.5$) areas, reducing the size of intervals in this region, where more accuracy is required, as shown in Figure 3.8 (a). The predictions of the surrogate model trained with the specialised binning method were compared with those of the classical

binning and with the high-rate experiments conducted at 75°C in Figure 3.8 (b). Significant improvements were observed in the targeted regions, and in particular, the accuracy of the model in predicting the peak and collapse regions was significantly enhanced.

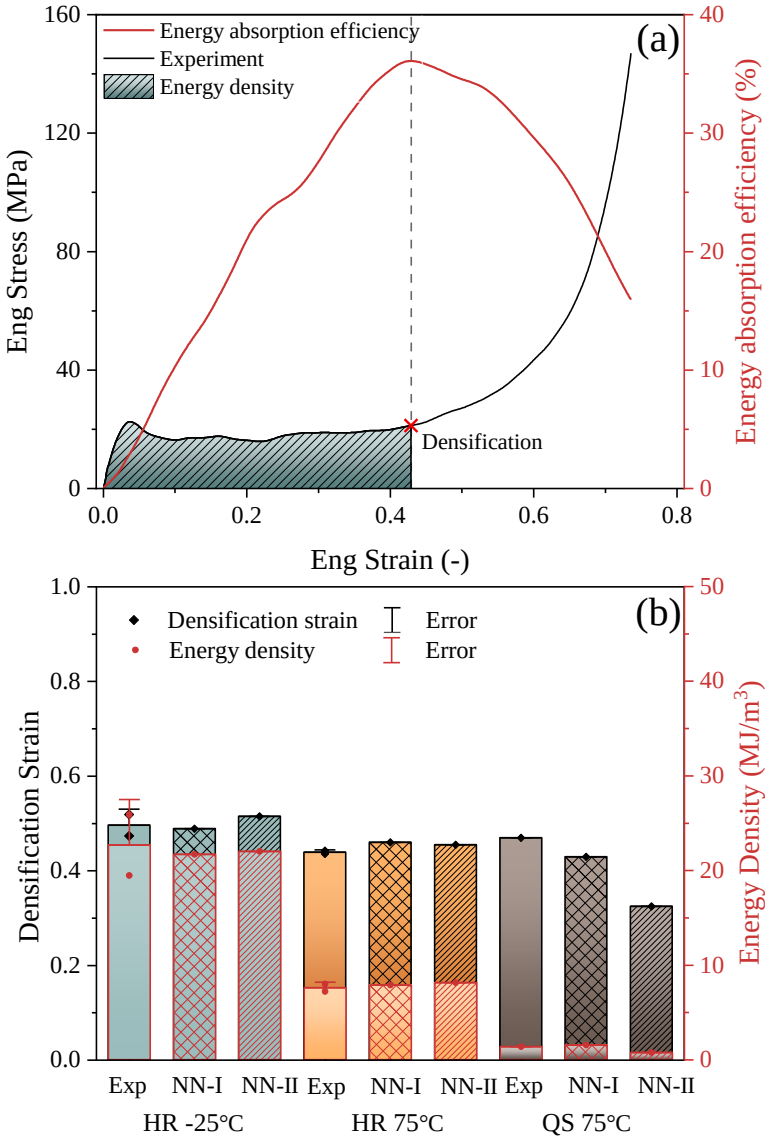


Figure 3.7. Definition of densification strain and energy dissipation (a) and (b) results provided by the surrogate models.

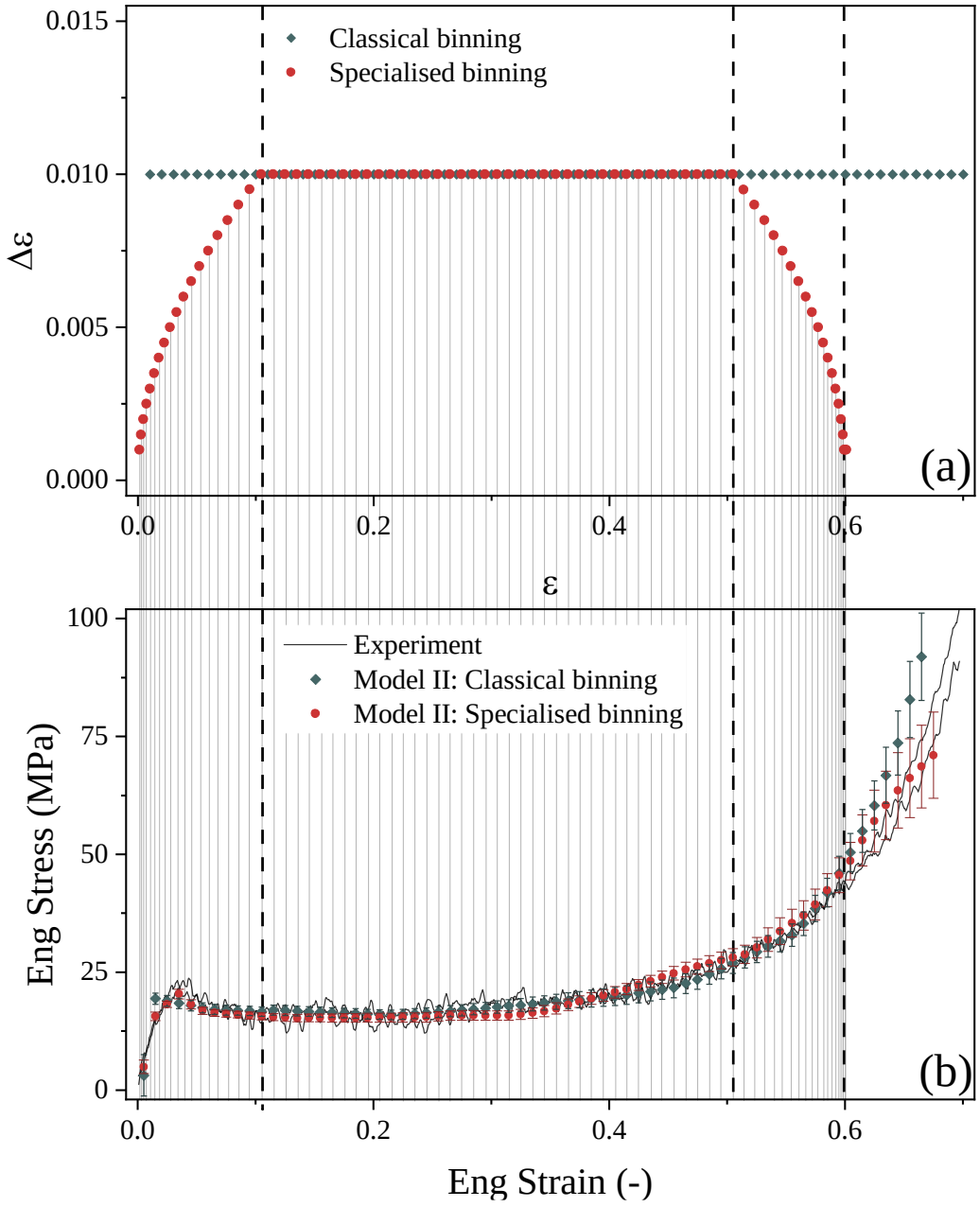


Figure 3.8. Comparison of classical binning and specialised binning; (a) description and (b) predictions of model II for a high-rate experiment conducted at 75 °C.

It is worth noting that the specialised binning data used for training was defined only up to $\varepsilon = 0.6$, whilst the predictions were obtained up to $\varepsilon = 0.7$. The surrogate model was allowed to extrapolate beyond the training region ($0.6 \leq \varepsilon \leq 0.7$). The predictions

within the extrapolation region were found to be in good agreement with the experiments and outperformed the classical binning method.

3.5 Conclusions

In this study, quasi-static and high-rate compression experimental data are used to train neural network models capable of predicting the stress-strain response of a syntactic foam as a function of stress, temperature and strain-rate. The stress-strain response is defined by inputs that contain information on the temperature and strain-rate dependency. The developed models are tested using three unseen experimental cases, and it is demonstrated that the obtained neural network models can successfully predict the stress-strain responses. Since the neural network model was trained using experimental data, it eliminates the need for the theoretical assumptions and constraints that characterise traditional models. The proposed method may provide researchers with an opportunity to accurately represent the temperature and strain-rate dependent stress-strain behaviour of engineering materials with potential savings in computational time and improvements in accuracy.

3.6 References

[1] Gupta N, Zeltmann SE, Shunmugasamy VC, Pinisetty D. Applications of polymer matrix syntactic foams. JOM 2014;66(2):245-254.

[2] Gupta N, Shunmugasamy VC. High strain rate compressive response of syntactic foams: Trends in mechanical properties and failure mechanisms. Materials Science and Engineering: A 2011;528(25-26):7596-7605.

[3] Song B, Chen W, Frew DJ. Dynamic compressive response and failure behavior of an epoxy syntactic foam. Journal of composite materials 2004;38(11):915-936.

[4] Pellegrino A, Tagarielli VL, Gerlach R, Petrinic N. The mechanical response of a syntactic polyurethane foam at low and high rates of strain. International Journal of Impact Engineering 2015;75:214-221.

[5] Song B, Chen WW, Lu WY. Mechanical characterization at intermediate strain rates for rate effects on an epoxy syntactic foam. International Journal of Mechanical Sciences 2007;49(12):1336-1343.

[6] Shunmugasamy VC, Gupta N, Nguyen NQ, Coelho PG. Strain rate dependence of damage evolution in syntactic foams. Materials Science and Engineering: A 2010;527(23):6166-6177.

[7] Bharath Kumar BR, Singh AK, Doddamani M, Luong DD, Gupta N. Quasi-static and high strain rate compressive response of injection-molded cenosphere/HDPE syntactic foam. JOM 2016;68(7):1861-1871.

[8] Fan Z, Miao Y, Wang Z, Zhang B, Ma H. Effect of the cenospheres size and internally lateral constraints on dynamic compressive behavior of fly ash cenospheres polyurethane syntactic foams. Composites Part B: Engineering 2019;171:329-338.

[9] Jakkula P, Ganzenmüller GC, Beisel S, Rüthnick P, Hiermaier S. The symmpact: A direct-impact Hopkinson bar setup suitable for investigating dynamic equilibrium in low-impedance materials. Experimental Mechanics 2022;62(2):213-222.

[10] Janoff D. Flexible, High Temperature Thermal Insulation Materials for Subsea Wellhead and Production Equipment. In: International Conference on Offshore Mechanics and Arctic Engineering. 2002, 36134.

[11] Wang W, Lou W. Syntactic foam thermal insulation for ultradeep high temperature applications. In: International Conference on Offshore Mechanics and Arctic Engineering. 2002, 36134.

[12] Gibson L J. Cellular solids. MRS Bulletin 2003;28:270-274.

[13] Tasdemir B, Pellegrino A, Tagarielli V. A strategy to formulate data-driven constitutive models from random multiaxial experiments. Scientific reports 2022;12(22248).

[14] Tasdemir B, Tagarielli V, Pellegrino A. A data-driven model of the yield and strain hardening response of commercially pure titanium in uniaxial stress. Materials & Design 2023;229(111878).

[15] Yanamandra K, Chen GL, Xu X, Mac G, Gupta N. Reverse engineering of additive manufactured composite part by toolpath reconstruction using imaging and machine learning. Composites Science and Technology 2020;198(108318).

[16] Siegkas P. Generating 3D porous structures using machine learning and additive manufacturing. Materials & Design 2022;220(110858).

[17] Chen CT, Gu GX. Machine learning for composite materials. MRS Commun. 2019;9:556–566.

[18] Gray III GT. Classic split-Hopkinson pressure bar testing. In: Kuhn H, Medlin D, editor. ASM handbook, Mechanical testing and evaluation. Ohio:ASM International, 2000. p.462-476.

[19] Pan B, Lu Z, Xie H. Mean intensity gradient: an effective global parameter for quality assessment of the speckle patterns used in digital image correlation. Opt Lasers Eng 2010;48:469–77.

[20] Quino G, Chen Y, Ramakrishnan KR, Martínez-Hergueta F, Zumpano G, Pellegrino A, Petrinic N. Speckle patterns for DIC in challenging scenarios: rapid application and impact endurance. Meas Sci Technol 2021;32:015203.

[21] Kolsky H. An investigation of the mechanical properties of materials at very high rates of loading. Proceedings of the physical society Section B 1949;62(11): 676.

[22] De Cola F, Pellegrino A, Glößner C, Penumadu D, Petrinic N. Effect of particle morphology, compaction, and confinement on the high strain rate behavior of sand. Experimental Mechanics 2018;58,223-242.

[23] Pellegrino A, Perez-Martin MJ, Dragnevski K, Zumpano G, Petrinic N. Temperature and strain rate dependent mechanical response of METCO 601 aluminium-polyester abradable seal coating. In: EPJ Web of Conferences 183, 2018, 04012.

[24] Goodfellow I, Bengio Y, Courville A. Deep Learning. The M.I.T. Press, 2016.

[25] Pedregosa F, Varoquaux G, Gramfort A, Michel V, Thirion B, Grisel O, Blondel M, Prettenhofer P, Weiss R, Dubourg V, Vanderplas J, Passos A, Cournapeau D, Brucher M, Perrot M, and Duchesnay É. Scikit-learn: Machine Learning in Python. the Journal of Machine Learning Research 2011;12:2825-2830.

[26] Nwankpa C, Ijomah W, Gachagan A, Marshall S. Activation functions: Comparison of trends in practice and research for deep learning. arXiv preprint arXiv 2018;1811.03378.

[27] Singh P, Manure A. Introduction to TensorFlow 2.0. In: Learn TensorFlow 2.0. Berkeley, CA: Apress, 2020. p.1-24.

[28] Kingma DP, Ba JL. Adam: A method for stochastic optimization. In: 3rd International Conference for Learning Representations. San Diego, 2015.

[29] Flores-Johnson EA, Li QM. Indentation into polymeric foams. International Journal of Solids and Structures 2010;47(16):1987-1995.

[30] Li QM, Magkiriadis I, Harrigan JJ. Compressive strain at the onset of densification of cellular solids. Journal of cellular plastics 2006;42(5):371-392.

CHAPTER 4

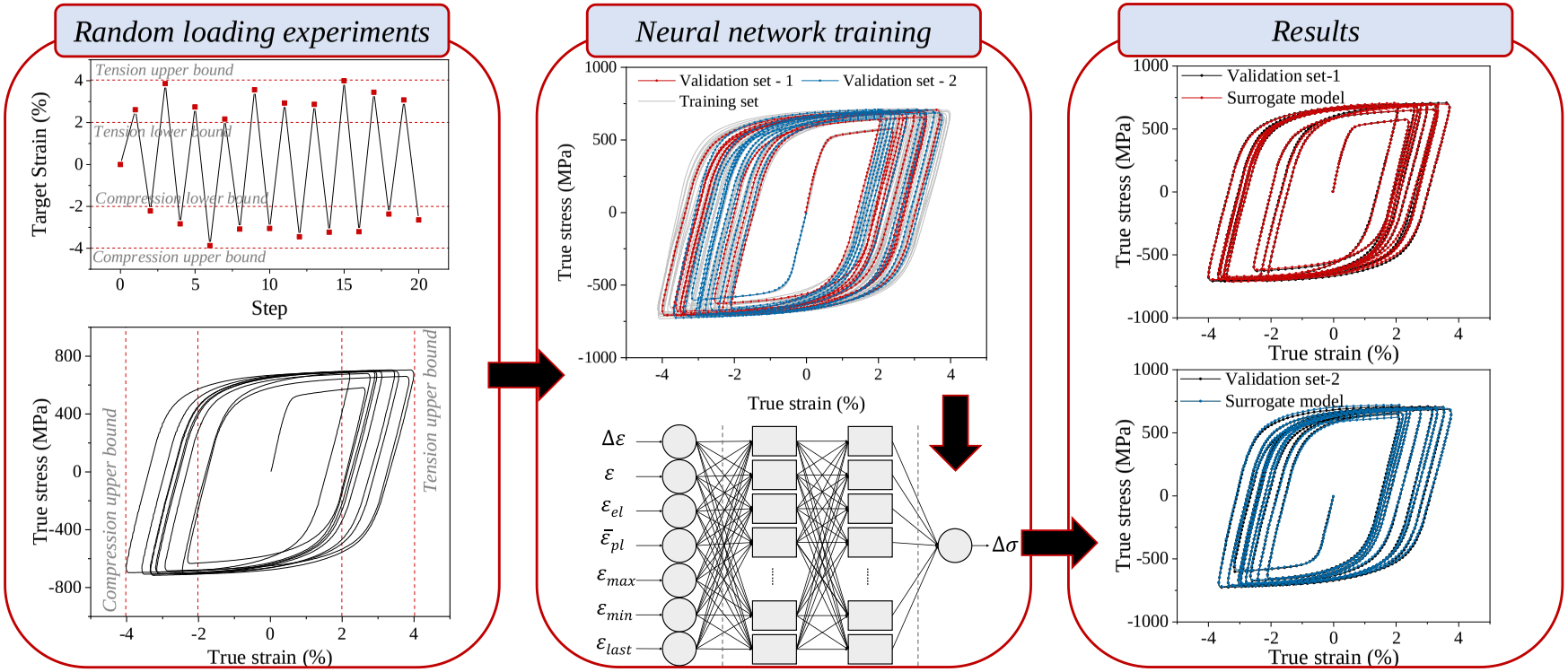
A DATA-DRIVEN MODEL OF THE YIELD AND STRAIN HARDENING RESPONSE OF COMMERCIALLY PURE TITANIUM IN UNIAXIAL STRESS

This Chapter focuses on modelling of uniaxial cyclic response of commercially pure titanium. A novel data-driven approach, utilizing actual experimental data, is employed to capture the complex material behaviour observed during reverse loading experiments, such as the smooth transition between elastic and plastic regions and the Bauschinger effect.

Abstract

This study presents a technique to develop data-driven constitutive models for the elastic-plastic response of materials, and applies this technique to the case of commercially pure titanium. The complex yield and strain hardening characteristics of this solid are captured for arbitrary non-monotonic uniaxial loading, without relying on any theoretical description. The surrogate model is obtained by supervised machine learning, relying on feed-forward neural networks trained with data obtained from random loading of titanium specimens in uniaxial stress. Uniaxial tests are conducted in strain control, applying random histories of axial strain in the range [-0.04, 0.04], to prevent the occurrence of significant damage. The corresponding stress versus strain histories are subdivided into a finite number of increments, and machine learning is applied to predict the change in stress in each increment. A suitable architecture of the

B. Tasdemir, V. Tagarielli, & A. Pellegrino, A data-driven model of the yield and strain hardening response of commercially pure titanium in uniaxial stress, Materials & Design 229(111878), 2023.



Keywords : Plasticity; Cyclic loading; Strain hardening; Machine learning; Surrogate model.

data-driven model, key to obtaining accurate predictions, is presented. The predictions of the surrogate model are validated by comparing to experiments not used in the training process, and compared to those of an established theoretical model. An excellent agreement is obtained between the measurements and the predictions of the data-driven surrogate.

4.1 Introduction

Accurate predictions of the elastic-plastic response of engineering materials are fundamental in structural design and failure analysis. For solids undergoing non-monotonic reversed loading, involving the sequential application of positive and negative plastic strains, accurate predictions can only be obtained if the details of the strain-hardening characteristic of the material are adequately captured. The theoretical models available to engineers often rely on simplifying assumptions, such as purely isotropic or kinematic hardening, or combinations of these. In this study, we model the complex strain hardening of commercially pure titanium using exclusively the results of carefully designed measurements, by applying supervised machine learning.

Plastic deformation is a dissipative mechanism and is therefore history-dependent; several researchers have applied machine learning techniques to predict this phenomenon [1-4]. In the presence of repeated and reversed plastic deformation, as for example in cyclic plasticity, the implementation of accurate constitutive models is complicated by the complex history-dependent strain hardening response of solids, which has been explored extensively for some metallic alloys [5,6].

Machine learning is being applied to solid mechanics to accelerate or enable complex material design and optimisation, including constitutive models for multiphysics problems [7,8], identification of material properties [9,10], inverse modelling and predictions of plastic flow as a function of temperature and strain rate [11,12]. Machine learning was also used to extend the experimentally measurable range of strains and enhance springback predictions in [13]. Most of the published work focuses on monotonic loading, in which it is not necessary to accurately capture the yield and strain hardening characteristic of the material investigated. Several authors (for example [14-16]) applied machine learning techniques to the case of reversed plasticity, developing surrogate models trained on datasets generated numerically, in which simple strain hardening characteristics (isotropic hardening) were assumed. Kinematic hardening was successfully predicted by data-driven models obtained using numerically generated data in [17,18].

In this study, we use data from actual experiments in uniaxial stress to construct a constitutive model that captures the details of the yielding and strain hardening response of a commercially pure titanium. The proposed technique is in principle applicable to any solid, but commercially pure titanium is chosen here for its ready availability and its well-studied strain hardening response, displaying a clear Bauschinger effect. Below we use feed-forward Neural Networks (a neural network is abbreviated below by NN) to construct a rate-independent surrogate model, also independent of any theoretical assumptions on the details of the material's yield and strain hardening. We use the surrogate model to predict the stress history consequent to the application of a random strain history.

The paper is structured as follows. In Section 4.2 we illustrate the details of the experiments conducted, while Section 4.3 presents the implementation of the data-driven surrogate model; results are presented and discussed in Section 4.4.

4.2 Mechanical Tests

4.2.1 Material and specimen geometry

Extruded bars of commercially pure titanium (Grade 3), of diameter 10 mm, were obtained from Smiths Metal Centres. Axisymmetric dogbone specimens were manufactured by turning, according to the geometry in Figure 4.1. The specimen geometry was designed considering previous research work ([19-20]) on cyclic plasticity tests, to ensure approximately uniform stress and strain in the gauge portion and to prevent buckling in presence of compressive loading.

4.2.2 Experimental setup and procedure

A portion of the specimen's gauge length was speckled to measure strain. The specimen was connected to a steel loading fixture by threaded connections. The fixture was loaded by a screw-driven testing machine via mounting pins, as shown in Figure 4.2. Uniaxial tension-compression cyclic experiments were conducted in real-time strain control; a video extensometer was used to measure the axial strain in the gauge portion and a feedback loop controlled such strain imposing a constant nominal strain rate of

$|\dot{\varepsilon}| = 10^{-3}\,\mathrm{s}^{-1}$ in all tests. The force was measured by a 20 kN resistive load cell. Strain and force measurements were recorded at a frequency of 10 Hz.

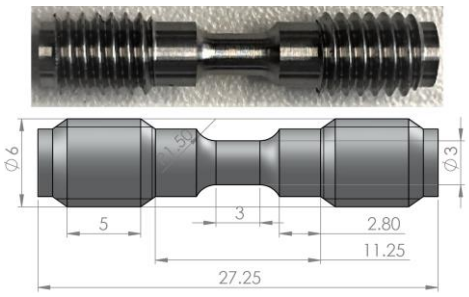


Figure 4.1. Specimen geometry (all dimensions in mm).

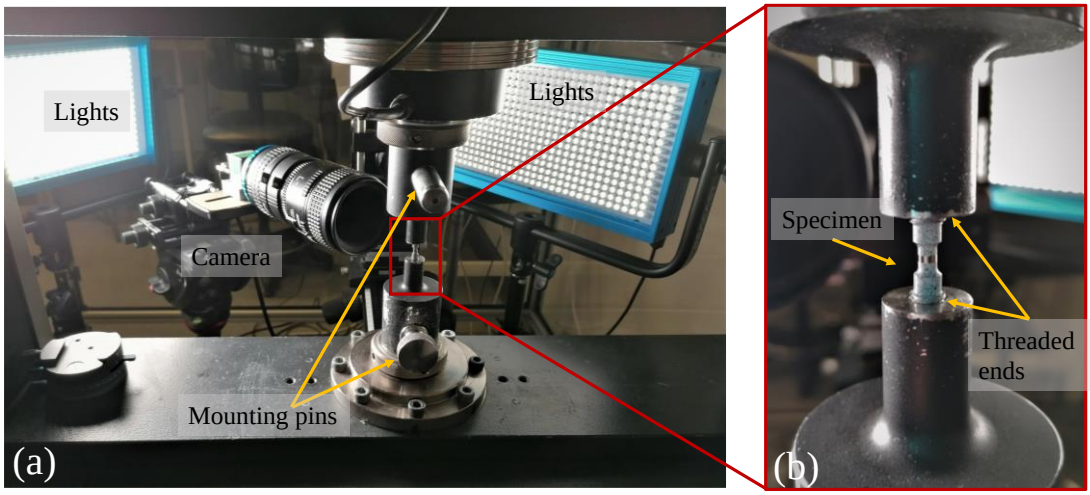


Figure 4.2. (a) View of the experimental setup; (b) close-up of the specimen and loading fixtures.

Nine random histories of reversed strain were imposed on different specimens. Each random history comprised 20 loading steps (10 cycles), and in each step a random change in axial strain $|\Delta\varepsilon_i| \in [\Delta\varepsilon_{\min}, \Delta\varepsilon_{\max}]$, $(i = 1, 2...20)$ was imposed on the specimen; the sign of the first change in strain was chosen randomly, while subsequent loading steps alternated positive and negative signs of the applied strain, i.e.

$$\Delta\varepsilon_{i=1} = \text{sign}\left(0.5 - r\right)\left[\Delta\varepsilon_{\min} + r\left(\Delta\varepsilon_{\max} - \Delta\varepsilon_{\min}\right)\right];$$
$$\Delta\varepsilon_{i} = -\text{sign}\left(\Delta\varepsilon_{i-1}\right)\left[\Delta\varepsilon_{\min} + r\left(\Delta\varepsilon_{\max} - \Delta\varepsilon_{\min}\right)\right], \quad (1)$$

where r is a uniformly random number between 0 and 1. We chose $\Delta\varepsilon_{\min} = 0.02$ and $\Delta\varepsilon_{\max} = 0.04$ to ensure that the material displayed both elastic and elastic-plastic responses in each step (note that the initial yield strain of pure titanium is less than 1%). The choice of having only 20 steps in each experiment was made to avoid low-cycle fatigue damage, as we will discuss quantitatively below. We note that some of the experiments were terminated before the 20th step, due to premature degradation of the speckling pattern during the test (and consequent inability to measure strain).

Figure 4.3 illustrates a representative random strain history imposed in one of the experiments. Figure 4.3 (a) shows the nominal strain versus time history, and Figure 4.3 (b) presents the corresponding true stress versus true strain measurement. The conversion between nominal and true stress and strain was conducted with the usual formulae for plastically incompressible solids (we note that the material used is practically void-free).

Titanium alloys containing a high volume fraction of the low temperature HCP α-phase typically display tension-compression yield strength asymmetry when subjected to uniaxial loading conditions at room temperature [21,22]. Previous studies have investigated the yield behaviour of commercially pure titanium of various purity grades and found that the tension-compression strength asymmetry is dependent on oxygen content and crystallite orientation distribution with respect to the loading axis [21], it is therefore not present in all grades of pure titanium. Titanium samples manufacture from

unidirectionally rolled plates show an appreciable tension compression yield strength asymmetry only in transverse direction [21,23]. The experimental data, obtained from samples made from an extruded bar, as expected displayed a stress versus strain response characterised by a Young's modulus of approximately 105 GPa, an initially approximately symmetric initial yield stress (the proof stress at a plastic strain of 0.2% was approximately 520 MPa in both tension and compression), and a noticeable Bauschinger effect upon reversed plasticity.

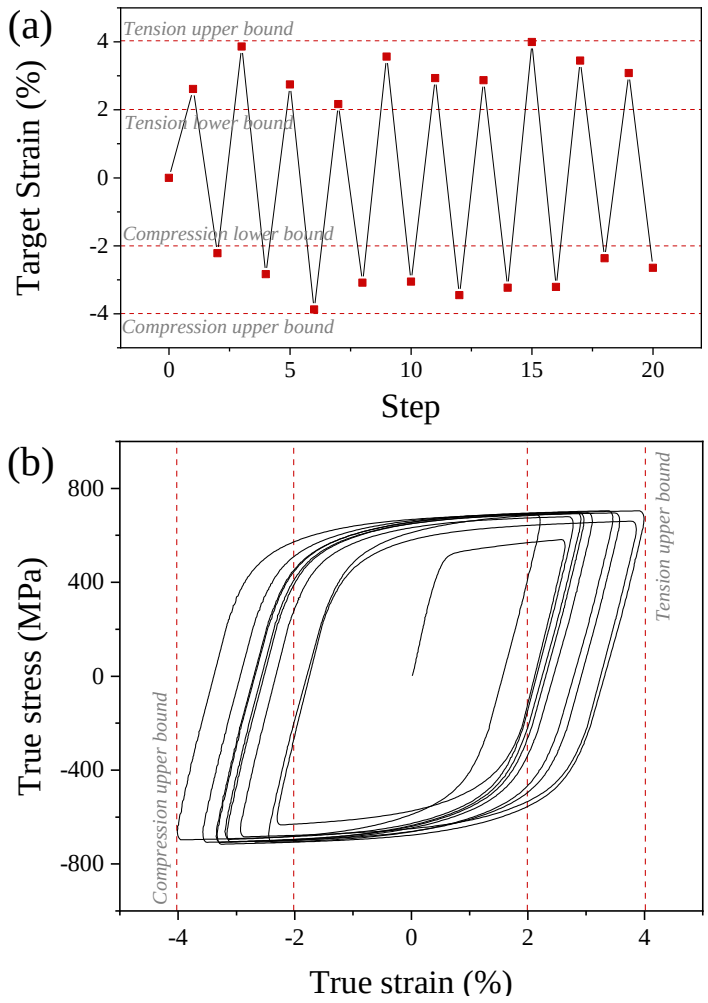


Figure 4.3. (a) Example of a random imposed nominal strain history; (b) stress-strain behaviour measured during the corresponding random cyclic loading experiment.

4.3 Implementation of the Surrogate Model

4.3.1 Training data set

Two of the nine experiments conducted (one starting with tensile loading and one with compressive loading) were stored to perform a validation of the predictions of our surrogate model; these are indicated as “Validation set” 1 and 2 in Figure 4.4. The remaining 7 experiments were used to assemble a training dataset. All data are visualised in Figure 4.4, with the 7 experiments used for training shown in grey and the 2 tests for validation shown in red and blue. The corresponding time histories of strain and stress to the data in Figure 4.4 are provided in Section 4.4. The stress versus strain measurements were used without further manipulations, with two exceptions: (i) not all recorded datapoints were used, but only 1/8 of the total were stored, as this number was sufficient to construct an accurate surrogate model; (ii) we removed the portions of the curves in the region $|\sigma| < 5\,\mathrm{MPa}$ (σ is the applied stress) to eliminate noisy stress/strain measurements due to the a small slack in the loading fixture. The data comprised 36457 increments, intended as portions of the loading and deformation history spanning the time comprised between two selected measurements; each increment, or more precisely the set of values of all variables at the beginning and end of the increment, represents one point of the training dataset.

In the implementation of the surrogate model, we assume that no damage (loss of stiffness) occurs during the tests. This is partially based on the existing literature on low-cycle fatigue of commercially pure titanium [24-27], some of which shows

negligible degradation of the material after 20 loading steps of strain amplitude up to 2.4%. To assess the likelihood of fatigue damage at higher strains (up to 4% was applied in this study), we measured the slope of the elastic unloading in our experiments, to assess the possible degradation of material stiffness. An example of such data is shown in Figure 4.5 for one selected experiment. It is observed that there is no evident degradation of the Young's modulus. Its variation, of at most 5% from step to step, is likely due to the experimental errors caused by the limited resolution of the video strain extensometer used.

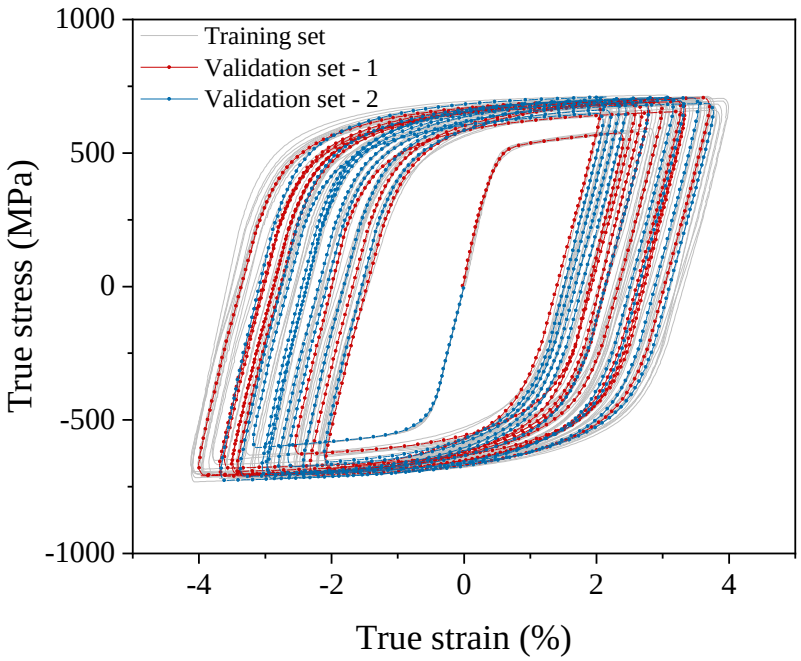


Figure 4.4. A summary of the data used in this study. The measurements used for training and testing are shown in grey; the experiments used for validation are in red and blue. Only 20% of the datapoints is shown for clarity.

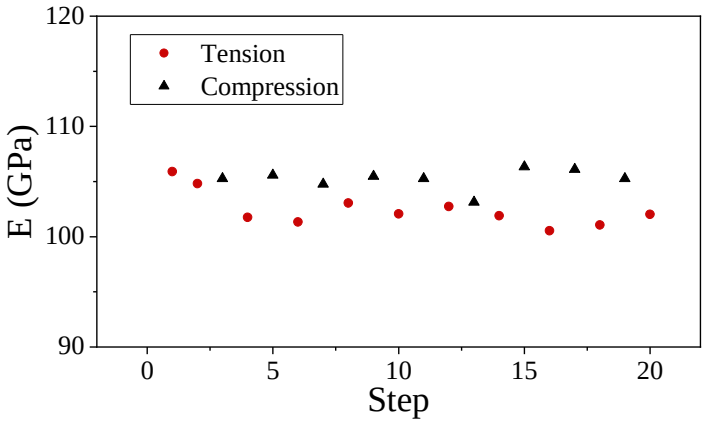


Figure 4.5. Evolution of the material's Young's modulus with increasing number of loading steps, for a selected experiment.

4.3.2 Surrogate model

A feed-forward regression neural network (NN_R) [28] is used in this study to implement the surrogate model. The network performs, at every increment, the regression

$$\Delta\sigma = NN_R\left(\Delta\varepsilon, \varepsilon, \varepsilon_{el}, \bar{\varepsilon}_{pl}, \varepsilon_{\max}, \varepsilon_{\min}, \varepsilon_{last}\right). \quad (2)$$

The variation of stress across one increment is taken to be a function of the increment in total strain $\Delta\varepsilon$, the total strain ε at the beginning of the increment, the elastic strain ε_{el} at the beginning of the increment (this is equivalent to the initial stress, as $\sigma = E\varepsilon_{el}$), the accumulated plastic strain $\bar{\varepsilon}^{pl}$, quantifying the extent of plastic deformation accumulated up to the current increment, and the additional parameters $\varepsilon_{\max}, \varepsilon_{\min}, \varepsilon_{last}$, quantifying the shift of the yield surface due to the history of plastic strains experienced.

The von Mises equivalent plastic strain reduces to the axial plastic strain in a uniaxial test; therefore the accumulated plastic strain can be calculated as the sum of the absolute

values of the increments in plastic strain in each loading step, i.e. $\bar{\varepsilon}_{pl} = \sum \left| \Delta \varepsilon_{pl} \right|$, where $\varepsilon_{pl} = \varepsilon - \varepsilon_{el}$, assuming additive strain decomposition.

The parameter $\varepsilon_{\max}$ is defined as the largest total tensile strain experienced by the material at the beginning of the current increment; it aims at quantifying the largest tensile plastic strain applied to the solid in its past deformation. Similarly, $\varepsilon_{\min}$ is the largest compressive strain experienced by the material at the beginning of the current increment; it has similar function as $\varepsilon_{\max}$ but focuses on compressive plastic strains.

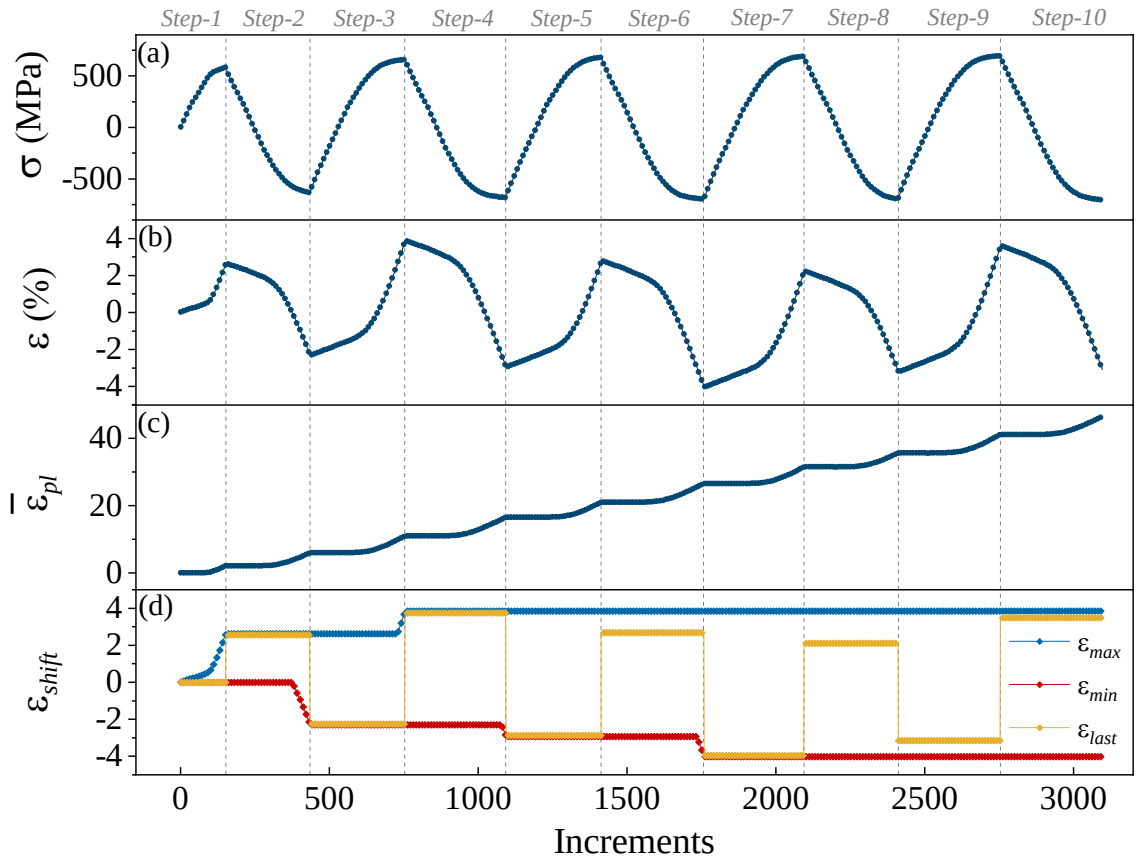


Figure 4.6. The evolution of NN inputs in a selected experiment (only the first 10 steps of the experiment are shown for clarity).

The parameter ε_{last} is defined, at any given point, as the total strain when the sign of $\Delta\varepsilon$ was last changed, i.e. when the direction of deformation was last reversed. Note that ε_{last} may or may not coincide with one between $\varepsilon_{\max}$ or $\varepsilon_{\min}$, but it cannot exceed (in absolute value) neither $\varepsilon_{\max}$ nor $\varepsilon_{\min}$. If ε_{last} does not coincide with $\varepsilon_{\max}$ or $\varepsilon_{\min}$, this indicates that the last time the deformation was reversed, the yield surface had not been shifted (or equivalently, $\varepsilon_{\max}$ or $\varepsilon_{\min}$ had not changed). Figure 4.6 illustrates the evolution in time of some of the inputs of the NN eqn. (2), for the same experiment shown in Figure 4.3.

The architecture of the NN was determined by trial and error; the final network comprised 2 hidden layers containing 100 neurons each. The inputs and outputs were rescaled to values between 0 and 1 using the minmax() function [29]; the ReLU [30] function was chosen as the activation function for the hidden layers, while the identity function was used for the output layer (i.e. no activation). The chosen loss function was the mean absolute error (MAE) [29]. The NN was trained in TensorFlow 2.0 [31] via backpropagation, using the Adam optimiser [32] with a learning rate of 0.001. The number of epochs was set to 3,000, with a batch size of 35. The data collected from the experiments shown in grey in Figure 4.4 was split into two subsets; one subset contained 90% of the total number of datapoints (increments) and was used for training, while the remaining datapoints (10% of the total) were used for testing; the increments in the two sets were randomly selected. At the end of the training, the explained variance score [29] was found to be equal to 0.996 (out of a maximum of 1 for a perfect regression).

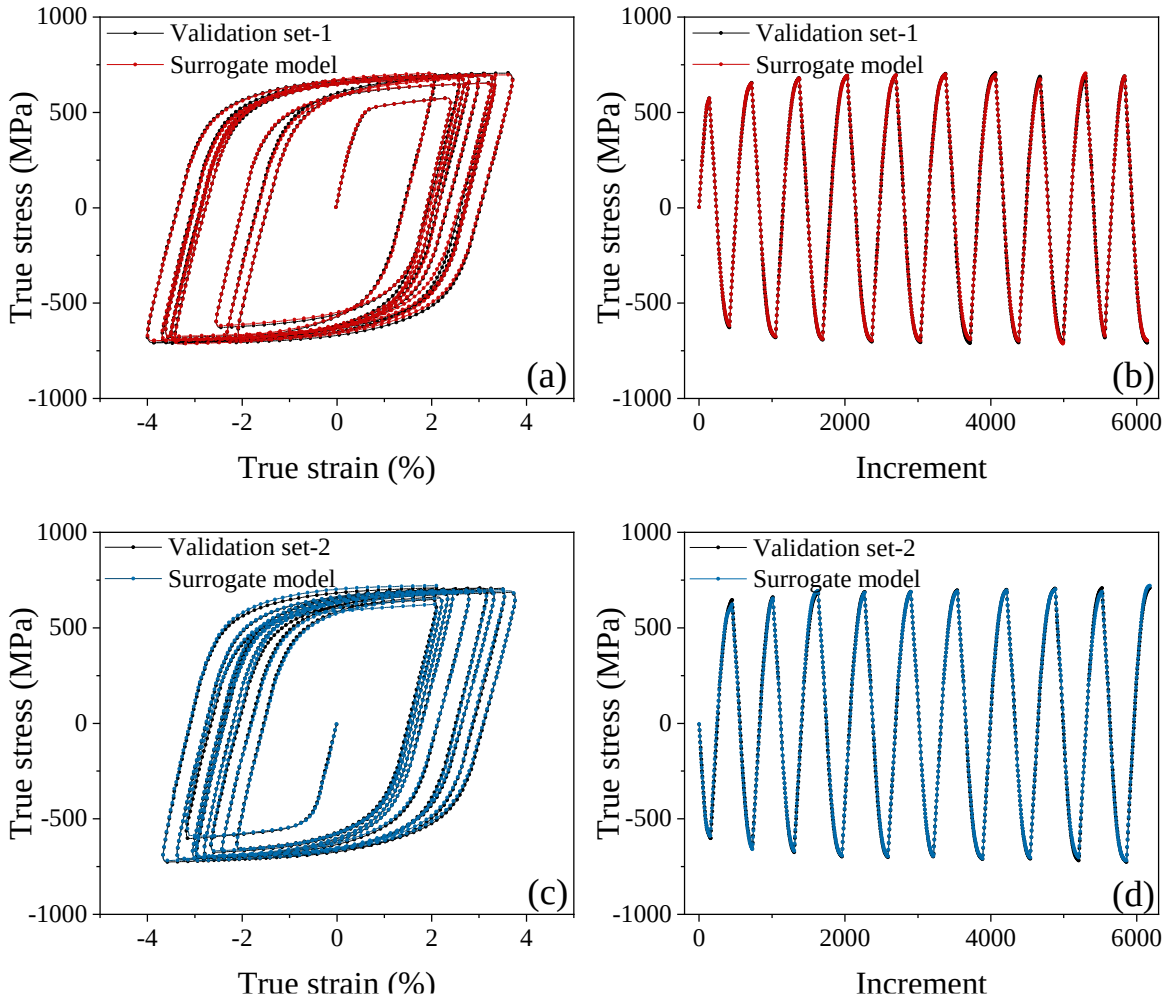


Figure 4.7. Comparison between the predictions of the surrogate model and the experiments; (a, b) validation set-1; (c, d) validation set-2.

4.3.3 Assessment of the accuracy of the surrogate model

To test the fidelity of the surrogate model, we focus on the data recorded in the 2 experiments shown in red and blue in Figure 4.4 these were processed as the remaining experiments, providing two strain histories, each split in sequences of consecutive applied strain increments. The surrogate model was used to predict the stress versus

strain responses corresponding to these two strain histories. For each history, starting from the initial stress- and strain-free configuration ($\varepsilon = \sigma = 0$), the sequence of consecutive strain increments was provided as an input to the surrogate model; in each increment, eqn. (2) was used to update the stress σ, and based on this, the accumulated plastic strain. The values of $\varepsilon_{\max}, \varepsilon_{\min}, \varepsilon_{last}$ were also updated, providing the input parameters for the subsequent increment. This allowed constructing predictions of the stress histories corresponding to the two unseen strain histories.

4.4 Results and Discussion

Figure 4.7 compares the predictions of the surrogate model to the two unseen experiments, in terms of the stress versus strain response and of stress versus time response (the strain versus time histories coincide for experiments and predictions). The NN predictions are in red and blue, while the measurements are shown in black; only 20% of the datapoints are shown for clarity of visualisation. The surrogate model is found in excellent agreement with the experiments, accurately predicting the strain hardening characteristic of the material loaded. The predictions deviate from the experiments by at most 5%, and such discrepancies only affect small portions of the deformation histories, consistent with the notion that the accuracy of the model is not uniform in input space, which can be consequent to the non-uniform distribution of the data in input space.

Figure 4.8 presents the distribution of the inputs. The comparison with experiments suggests that the proposed architecture of the surrogate model is effective in capturing

the physics of the material's yielding and strain hardening. Such architecture was determined by a trial and error procedure (omitted here for brevity), which showed that the inclusion as inputs of the accumulated plastic strain $\bar{\varepsilon}^{pl}$ and of the parameters $\varepsilon_{\max}, \varepsilon_{\min}, \varepsilon_{last}$ was essential in allowing an accurate regression with a small NN and limited data. The first parameters $\bar{\varepsilon}^{pl}$ carries two types of physically relevant information: its rate $\dot{\bar{\varepsilon}}^{pl}$ allows distinguishing between elastic ($\dot{\bar{\varepsilon}}^{pl} = 0$) and elastic-plastic ($\dot{\bar{\varepsilon}}^{pl} > 0$) deformation; its magnitude quantifies the accumulated permanent changes to the material's microstructure (e.g. dislocation density). The knowledge of $\varepsilon_{\max}, \varepsilon_{\min}, \varepsilon_{last}$ provides the model with information regarding the maximum strains experienced up to the current increment, and permits determining if the current deformation follows a shift of the yield surface in the opposite direction. The size of the NN, and therefore the speed of the surrogate model, could be reduced by optimising the network's architecture and separating elastic from elastic-plastic increments, as in [2].

We note that only 7 simple uniaxial tests were required to train the data-driven model presented here, and this is comparable to the number of tests typically used to calibrate theoretical models for the response of pure titanium. Data-driven constitutive models similar to that presented here are expected to be particularly effective in the case of recently developed materials, for which there could be lack of understanding of the physical response and of corresponding theoretical descriptions. In this case surrogate models could allow immediate predictions of the response of complex components, and more rapid deployment of new materials to engineering applications.

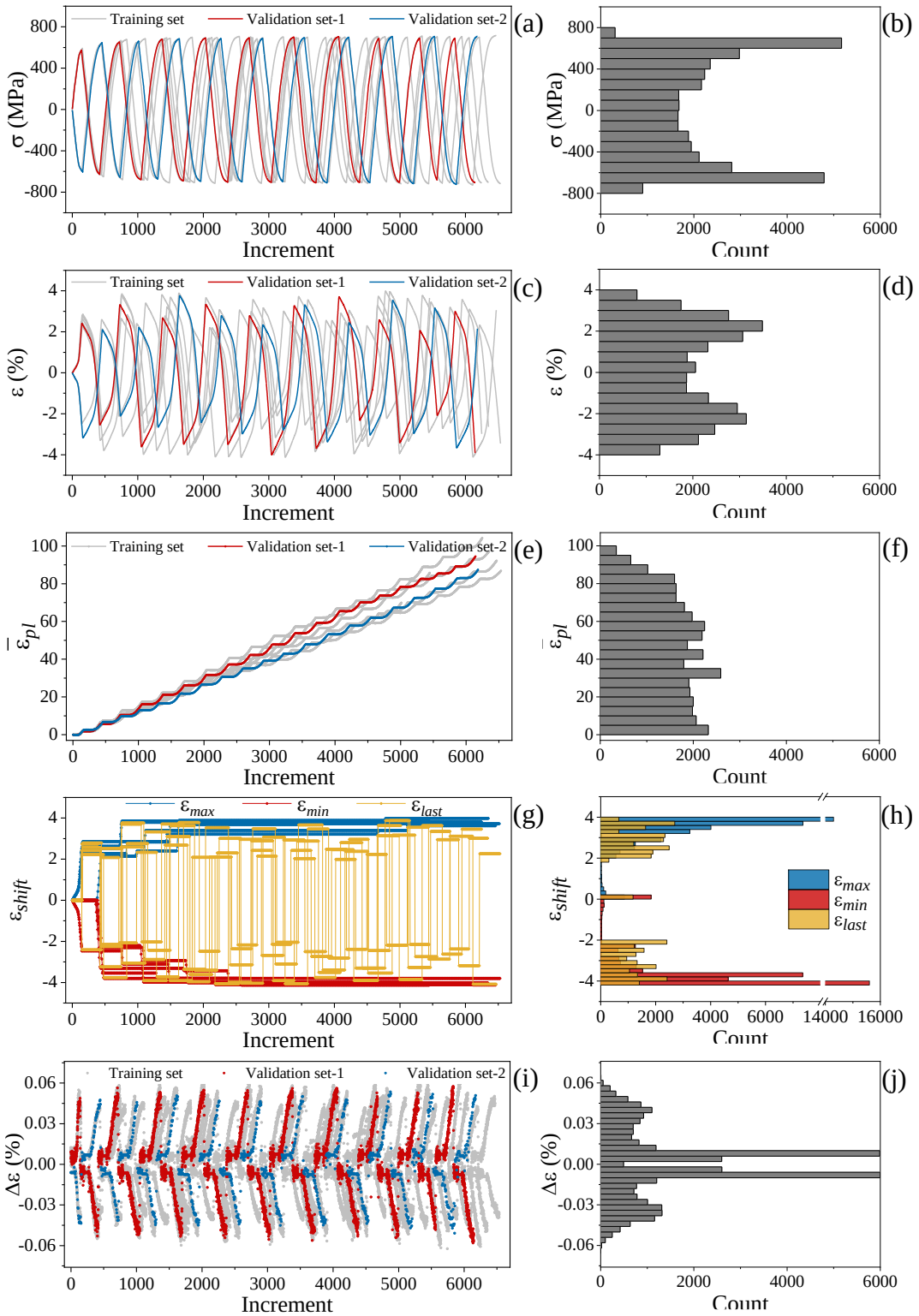


Figure 4.8. Evolution in time increments and probability density distributions of (a, b) true stress, (c, d) total true strain, (e, f) accumulated plastic strain, (g, h) ε_{min}, ε_{max}, ε_{last}, and (i, j) increments of strain.

In this study we have only explored the response of the material to deformation in uniaxial stress, therefore the surrogate predictions are only valid in such regime. For pure titanium, an extension to the case of multiaxial deformation could be attempted, by assuming and implementing appropriate constraints for a 3D surrogate constitutive model. However, for materials that are not as well understood as pure titanium, multiaxial experiments are required to assemble a suitable training dataset for a surrogate model of general applicability. The current approach assumes no damage and a rate-independent response of the material, which can be inappropriate assumptions in different strain regimes and for different solids. In our future studies we will work at overcoming the above limitations and at applying similar data-driven constitutive modelling to different materials.

To further assess the effectiveness of the surrogate model proposed, we proceed to compare its accuracy with that of a popular theoretical model for cyclic plasticity, i.e. the constitutive model proposed by Armstrong and Frederik [33] based on the von-Mises yield criterion with associative plasticity [34,35]. The above model is implemented in Abaqus [35] and can simulate non-linear isotropic and kinematic hardening in metallic alloys with a relatively modest number of hardening parameters. The evolution of the yield surface is decomposed in the isotropic part Q_{ISO}, i.e. the expansion of the yield surface, and the kinematic part Q_{KIN}, that is the shifting of the yield surface. These are functions of the accumulated plastic strain $\bar{\varepsilon}_{pl}$, as it follows:

$$\begin{aligned} \sigma_{ISO} &= Q_{\inf}\left(1-e^{(-\mathrm{b}.\bar{\varepsilon}_{pl})}\right) \\ \sigma_{KIN} &= \sigma_{KIN_1}+\sigma_{KIN_2} = \sum_{i=1,2}\frac{C_i}{\gamma_i}(1-\mathrm{e}^{-\gamma.\bar{\varepsilon}_{pl}}) \end{aligned} \tag{3}$$

where $Q_{\inf}$ denotes the maximum magnitude of the yield surface expansion and b is a parameter that controls the rate of expansion. The kinematic part of the nonlinear hardening, i.e. the translation of the yield surface resulting in the Bauschinger effect, was represented using two backstress tensors Q_{KIN_1} and Q_{KIN_2}, each corresponding to a component of translation of the yield surface. The use of two backstresses was found to be optimal to maximise the agreement between the model's predictions and the test results used to calibrate the same model. The parameters C_1, C_2, and γ_1, γ_2 govern the evolution of the backstress with respect to the accumulated plastic strain. For every step of deformation, the current yield stress is equal to the sum of initial yield stress and hardening stresses due to isotropic and kinematic hardening (eqn. (4), Figure 4.9).

$$\sigma_y = \sigma_0 + \sigma_{ISO} + \sigma_{KIN_1} + \sigma_{KIN_2} . \tag{4}$$

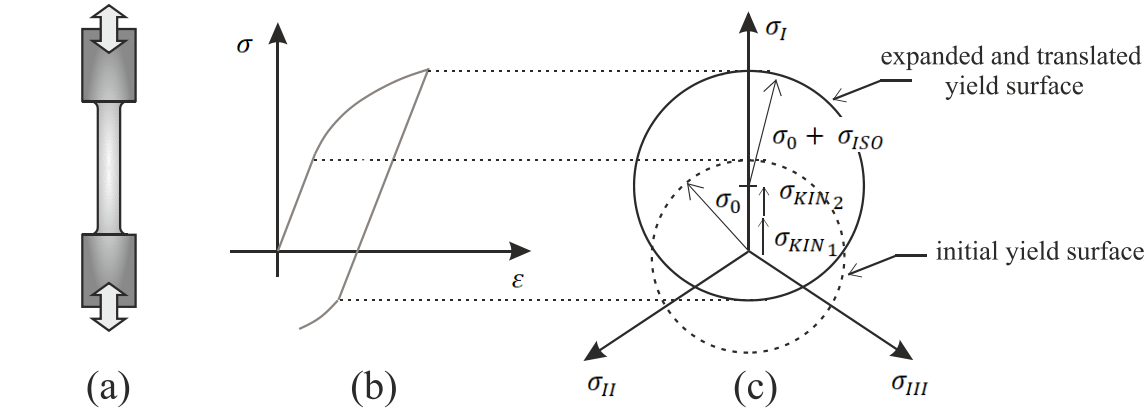


Figure 4.9. Armstrong and Frederik model: a) cyclically loaded specimen b) stress-strain response c) yield surface motion and expansion in the π plane.

The parameters of the Armstrong and Frederik constitutive equation were identified using the results of additional measurements on the same material. The constitutive

model required inputting the stabilised cyclic behaviour of the material in tension, as well as additional information on the variation of the yield stress during successive cycles until stabilisation. Details on the calibration of the employed combined isotropic-kinematic hardening model can be found in [35].

Additional cyclic straining experiments were conducted. The sample geometry and experimental setup were analogous to those described above, with the exception that these additional tests were conducted prescribing symmetric cycles of constant total strain amplitude (rather than a random amplitude between 0.02 and 0.04).

The experimental data, obtained from stabilised symmetric cycles, were inputted in Abaqus, which determined by optimisation the kinematic hardening parameters C_i, and γ_i. Two sets of these parameters were determined, using data from two cyclic straining experiments with different strain amplitudes of 0.02 and 0.04. Calibration parameters were determined from each experiment and then averaged to determine the set to be included in FE simulations; a summary of their value is presented in Table 4.1. We also note that multiple backstress terms can be considered in this model; a preliminary investigation revealed that the accuracy of the predictions is maximised when using two backstresses, therefore we make this choice in the following.

The measured stress-strain histories in these two additional cyclic tests are shown in Figure 4.10, together with the corresponding predictions of the Armstrong and Frederik model.

Table 4.1 Kinematic/isotropic hardening model parameters.

CURVE FITTING OF THE TEST DATA

Calibration Experiment Amplitude	Curve Fit Error	Yield Stress (MPa)	Backstress (i)	Parameter C_i (MPa)	Parameter γ_i (-)
2%	0.00419	439.53	1	17824.	129.59
			2	100747.	1169.5
4%	0.10236	465.89	1	4737.7	67213.
			2	67213.	407.08

NONLINEAR KINEMATIC/ISOTROPIC HARDENING MODEL

KINEMATIC COMPONENT

Yield Stress (MPa)	Backstress (i)	Parameter C_i (MPa)	Parameter γ_i (-)
400.00	1	11281.	90.311
	2	83980.	788.28

ISOTROPIC COMPONENT

Yield Stress (MPa)	Plastic Strain (-)
400.00	0.0000
669.55	12.601
682.71	25.347
683.99	37.933

Clearly the model fails to capture the initial yielding characteristic of the material, as such initial yielding is not part of the required inputs. It does capture reasonably well the stabilised response of the material, and it does this better in tension than in compression, as the model requires only tensile data and assumes an inherently symmetric response.

The accuracy of the proposed surrogate model is compared to that of the theoretical model [33], by testing both models when predicting the stress histories corresponding to random histories of strain. Figure 4.11 illustrates such comparison. Following the

first yield, the theoretical model overestimates the measured strain hardening. Upon load reversal, the theoretical model also overpredicts the stresses during the compressive yielding of the solid. With increasing number of random plastic straining steps, the theoretical model converges to a nearly stabilised response with smaller strain hardening than observed experimentally. The errors of the theoretical model are generally larger in compression than in tension, as the model cannot capture the asymmetric response. In contrast, the data-driven model captures all phases of the material's response.

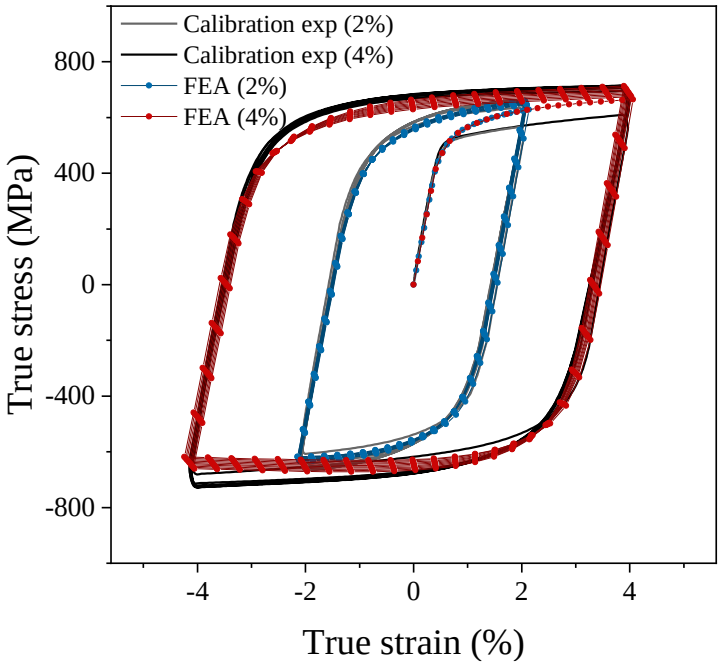


Figure 4.10. Calibration experiments and predictions of the theoretical hardening model.

The absolute value of the errors made by the two models at every strain increment are compared in Figure 4.12. It is evident that the absolute error of the data-driven surrogate model is negligible throughout all stages of deformation, while the error of the

theoretical model is initially approximately five times larger than that of the surrogate model, and this factor tends to increase with increasing accumulated applied strain.

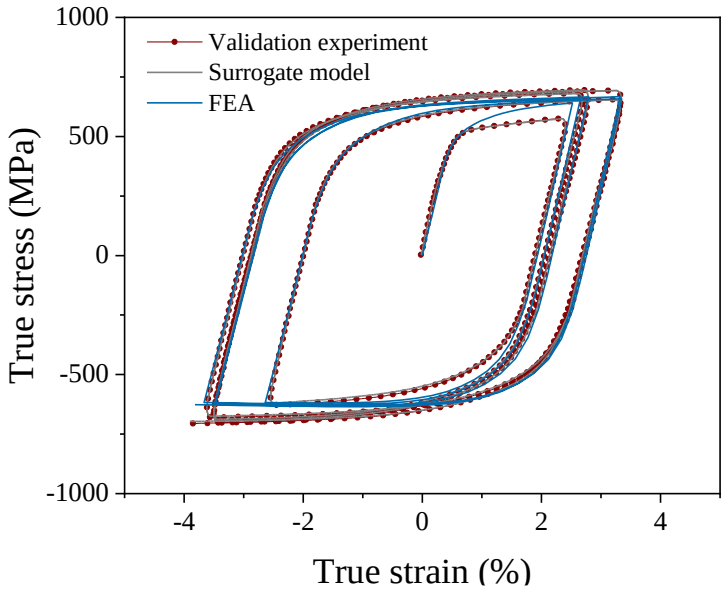


Figure 4.11. Comparison of the surrogate model and the cyclic hardening model of Abaqus.

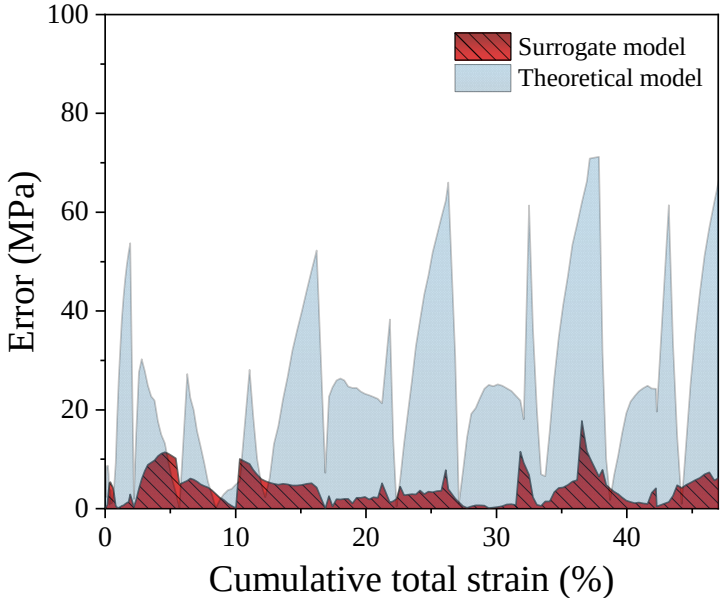


Figure 4.12. Comparison of the errors of the surrogate and theoretical models.

4.5 Conclusions

We presented a strategy to implement data-driven constitutive models for the uniaxial response of pure titanium. We used the results of seven experiments to train a surrogate constitutive model of the material response to random strain histories in uniaxial stress; such model predicts the change in stress over an increment of the imposed deformation. The predictions of the surrogate model were found to be computationally efficient, relying on a small feed-forward NN while achieving great accuracy. The complex yielding and strain hardening of pure titanium were captured correctly by including in the surrogate model specific inputs describing the effects of the past history of deformation, namely the accumulated plastic strain, quantifying the extent of the magnitude of past plastic deformation, and three additional parameters measuring the shift of the yield surface and the occurrence of reversed plasticity. The performance of the surrogate model was found to largely exceed that of an established theoretical model for the cyclic hardening of metals. The current approach is limited to the response of pure titanium in uniaxial stress and it assumes no loss of cohesion of the material and a rate independent response; we will explore the extension to the multiaxial response of general solids in our future studies.

4.6 References

[1] M. Mozaffar, R. Bostanabad, W. Chen, K. Ehmann, J. Cao, and M. A. Bessa ,Deep learning predicts path-dependent plasticity, Proceedings of the National Academy of Sciences, 116.52, 26414-26420, 2019.

[2] W. Ge, and V.L. Tagarielli, A computational framework to establish data-driven constitutive models for time- or path-dependent heterogeneous solids, Scientific reports, 11(15916), 2021.

[3] F. Ghavamian, and A. Simone, Accelerating multiscale finite element simulations of history-dependent materials using a recurrent neural network, 357,112594, 2019.

[4] B. Tasdemir, A. Pellegrino, and V. Tagarielli, A strategy to formulate data-driven constitutive models from random multiaxial experiments, Scientific reports,12(22248), 2022.

[5] M. Dahlberg and P. Segle, Evaluation of models for cyclic plastic deformation – A literature study, Sweedish Radiation Safety Autority, Technical Report no. 2010:45.

[6] S. K. Paul, S. Sivaprasad, S.Dhar, and S. Tarafder, Key issues in cyclic plastic deformation: experimentation, Mechanics of materials, 43(11), 705-720, 2011.

[7] M.A.S. Matos, S.T. Pinho, and V.L. Tagarielli, Application of machine learning to predict the multiaxial strain-sensing response of CNT-polymer composites, Carbon, 146, 265-275, 2019.

[8] M.A.S. Matos, S.T. Pinho, and V.L. Tagarielli, Predictions of the electrical conductivity of composites of polymers and carbon nanotubes by an artificial neural network, Scripta Materialia, 166, 112-12, 2019.

[9] J. Zhao and F. Wang, Parameter identification by neural network for intelligent deep drawing of axisymmetric workpieces, Journal of Materials Processing Technology, 166(3),387-391, 2005.

[10] M.V. Pathan, S.A. Ponnusami, J. Pathan, R. Pitisongsawat, B. Erice, N. Petrinic, and V.L. Tagarielli, Predictions of the mechanical properties of unidirectional fibre composites by supervised machine learning, Scientific reports, 9(13964), 1-10, 2019.

[11] Y.C. Lin, J. Zhang, and J. Zhong, Application of neural networks to predict the elevated temperature flow behavior of a low alloy steel, Computational Materials Science, 43, 752-758, 2008.

[12] X. Li, C.C. Roth, and D. Mohr, Machine-learning based temperature-and rate-dependent plasticity model: application to analysis of fracture experiments on DP steel, International Journal of Plasticity, 118, 320-344, 2019.

[13] Z. Liu, Y. Hou, R. He, Y. Ye, C. Niu, J. Min, Machine learning for extending capability of mechanical characterization to improve springback prediction of a quenching and partitioning steel, J. Mater. Process. Technol., 308(117737), 2022.

[14] D. Huang, J.N. Fuhg, C. Weißenfels, and P. Wriggers, A machine learning based plasticity model using proper orthogonal decomposition, Computer Methods in Applied Mechanics and Engineering, 365,113008, 2020.

[15] D.P. Jang, P. Fazily, and J.W. Yoon, Machine learning-based constitutive model for J-2 plasticity, International journal of plasticity, 138(102919),2021.

[16] M. Teranishi, Neural network constitutive model for uniaxial cyclic plasticty based on return mapping algorithm, Mechanics research communications, 119(103815), 2022.

[17] X. Liu, J. He, S. Huang, Mechanistically informed artificial neural network model for discovering anisotropic path-dependent plasticity of metals, Materials & Design, 226(111697), 2023.

[18] D. Liu, H. Yang, K.I. Elkhodary, S. Tang, W.K. Liu, X. Guo, Mechanistically informed data-driven modeling of cyclic plasticity via artificial neural networks. Computer Methods in Applied Mechanics and Engineering, 393(114766), 2022.

[19] N. C. Sole, N. Petrinic, and A. Pellegrino, An investigation on the Bauschinger effect in titanium alloys for aerospace applications: strain rate and pressure dependence, MSc Thesis, University of Oxford, 2021.

[20] S. Sivasubramaniam, The development of reverse loading split hopkinson pressure bar

systems for the study of the dynamic bauschinger effect, DPhil Thesis, University of Oxford, 2010.

[21] M.C. Brandes, M. Baughman, M.J. Mills, and J.C. Williams, The effect of oxygen and stress state on the yield behavior of commercially pure titanium, Materials Science and Engineering: A, 551, 13-18, 2012.

[22] P. Lin, Y. Hao, B. Zhang, S. Zhang, C. Chi, and J. Shen, Tension-compression asymmetry in yielding and strain hardening behavior of CP-Ti at room temperature, Materials Science and Engineering: A, 707, 172-180, 2017.

[23] B. Revil-Baudard, O. Cazacu, and E. Massoni, Room-temperature plastic behavior and formability of a commercially pure titanium: Mechanical characterization, modeling, and validation, International Journal of Solids and Structures, 228, 111121, 2021.

[24] S. Sinha, and N.P. Gurao, The role of crystallographic texture on load reversal and low cycle fatigue performance of commercially pure titanium, Materials Science and Engineering: A, 691, 100-109, 2017.

[25] Z.F. Zhang, H.C. Gu, and X.L. Tan, Low-cycle fatigue behaviors of commercial-purity titanium, Materials Science and Engineering: A, 252(1), 85-92,1998.

[26] G. Kim, S.A.A. Shams, J.N. Kim, J.W. Won, S.W. Choi, J.K. Hong, and C.S. Lee, Enhancing low-cycle fatigue life of commercially-pure Ti by deformation at cryogenic temperature, Materials Science and Engineering: A, 803, 140698, 2021.

[27] C.Q. Chenand S.X. Li, Tensile and low-cycle fatigue behaviors of commercially pure titanium containing γ hydrides, Materials Science and Engineering: A, 387, 470-475, 2004.

[28] I. Goodfellow, Y. Bengio, and A. Courville, Deep Learning, The M.I.T. Press, 2016.

[29] F. Pedregosa, G. Varoquaux, A. Gramfort, V. Michel, B. Thirion, O. Grisel, M. Blondel, P. Prettenhofer, R. Weiss, V. Dubourg, J. Vanderplas, A. Passos, D. Cournapeau, M. Brucher, M. Perrot, and É. Duchesnay, Scikit-learn: Machine Learning in Python, the Journal of Machine Learning Research, 12, 2825-2830, 2011.

[30] C. Nwankpa,W. Ijomah, A. Gachagan, and S. Marshall, Activation functions: Comparison of trends in practice and research for deep learning, arXiv preprint arXiv:1811.03378, 2018.

[31] Singh P., Manure A. Introduction to TensorFlow 2.0. In: Learn TensorFlow 2.0. Apress, Berkeley, CA., 1-24, 2020.

[32] D. P. Kingma and J.L. Ba, Adam: A method for stochastic optimization, ICLR 2015, 1412, 6980, 2014.

[33] Frederick, C. O., & Armstrong, P. J. (2007). A mathematical representation of the multiaxial Bauschinger effect. Materials at High Temperatures, 24(1), 1-26.

[34] Cooke, R. J., & Kanvinde, A. M. (2015). Constitutive parameter calibration for structural steel: Non-uniqueness and loss of accuracy. Journal of Constructional Steel Research, 114, 394-404.

[35] ABAQUS, ABAQUS/Standard User's Manual, version 6.14,Desault Systems, Providence (RI, USA) (2014).

CHAPTER 5

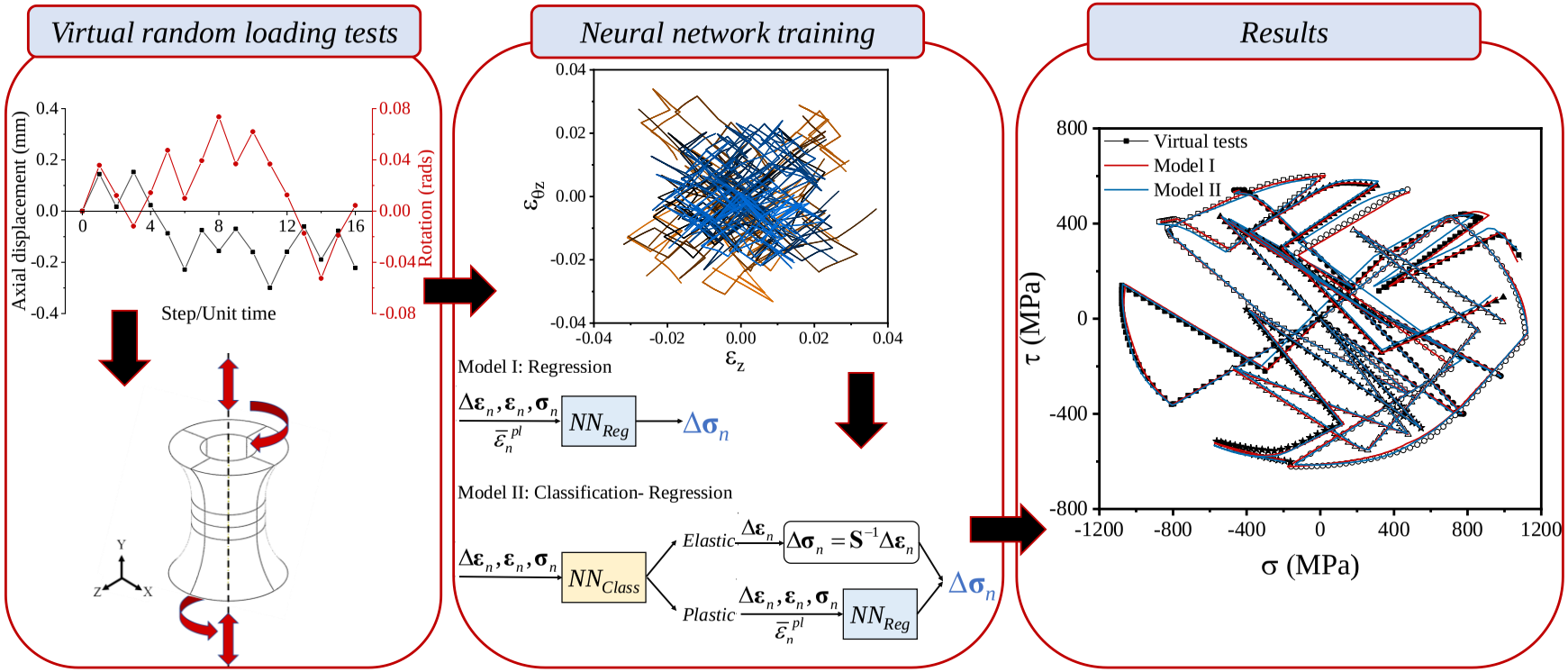
A STRATEGY TO FORMULATE DATA-DRIVEN CONSTITUTIVE MODELS FROM RANDOM MULTIAXIAL EXPERIMENTS

In this Chapter, a strategy to model the multiaxial non-monotonic and non-proportional response of a virtual material is presented. The main novelty of this study is the development of a data-driven model for predicting the multiaxial material behaviour in the context of real experiments, while also accounting for the complexities of real specimen geometries.

Abstract

We present a test technique and an accompanying computational framework to obtain data-driven, surrogate constitutive models that capture the response of isotropic, elastic-plastic materials loaded in-plane stress by combined normal and shear stresses. The surrogate models are based on feed-forward neural networks (NNs) predicting the evolution of state variables over arbitrary increments of strain. The feasibility of the approach is assessed by conducting virtual experiments, i.e. Finite Element (FE) simulations of the response of a hollow, cylindrical, thin-walled test specimen to random histories of imposed axial displacement and rotation. In these simulations, the specimen's material is modelled as an isotropic, rate-independent elastic-plastic solid obeying J2 plasticity with isotropic hardening. The virtual experiments allow assembling a training dataset for the surrogate models. The accuracy of two different

B. Tasdemir, A. Pellegrino, & V. Tagarielli, A strategy to formulate data-driven constitutive models from random multiaxial experiments, Scientific Reports 12 (22248), 2022.



Keywords : Machine learning; Surrogate models; Data-driven; Constitutive models.

surrogate models is evaluated by performing predictions of the response of the material to the application of random multiaxial strain histories. Both models are found to be effective and to have comparable accuracy.

5.1 Introduction

Applications of machine learning have exponentially increased in number during the last decade and have spread to different fields including image recognition, web search, voice recognition, financial services, healthcare, sales, and more. Recent research also explored applications of machine learning to the mechanics of solids, with the main objective of reducing the computational cost of simulations involving complex material behaviour, by the introduction of surrogate constitutive models or data-driven microstructure-properties relations ([1-3]). This exercise is particularly difficult in the presence of history-dependent responses [4]. Some authors have attempted using recurring NNs to capture non-linear, path-dependent constitutive responses of different types of solids [5]; considerable work has explored the response of heterogeneous solids, mainly two-phase composites, and used data-driven approaches to predict the effects of their microstructure upon the mechanical behaviour (e.g. [6]). Some researchers have worked on data-driven models for elastic-plastic solids, collecting training datasets from simulations or measurements of proportional loading histories [7,8,9] or from the results of structural tests [10]. We recently proposed a computational procedure to develop surrogate constitutive models for multiphase random composites [11] with time- and path-dependence response, suitable for arbitrary multi-axial and non-proportional loading.

Several of the data-driven models described above trained with numerical simulations of the response of Representative Volume Elements (RVEs) or of single FEs of known constitutive description. Similar approaches can in principle be developed using data obtained directly from measurements, to implement model-free simulations, as shown effectively by [10, 12-16]. No previous research however has focused on developing data-driven constitutive models for elastic-plastic materials starting from data obtained from measurements and including non-monotonic and non-proportional loading; this is the objective of the present study.

Here we follow similar steps as in [11] to obtain surrogate constitutive descriptions of the response of solid materials from measured data collected in lab-scale experiments. The objective is to develop numerical descriptions of the material behaviour which do not rely on any particular theory and are able to predict the material response subject to arbitrary loading, including complex non-monotonic and non-proportional deformation histories. To prove the feasibility of the approach, we conduct virtual tests by performing FE simulations of the response of a hollow, cylindrical, thin-walled test specimen to random histories of imposed non-proportional axial displacement and torsional rotation. The results of the simulations are processed in the same way as in actual experiments, obtaining time histories of the average direct and shear stresses and strains in the specimen's gauge portion. Repeated virtual experiments are conducted by imposing multiple random deformation histories, such to adequately sample the space of the applied deformation. Such strain and stress histories are subdivided in small time increments, and the stresses and strains at the beginning and at the end of each increment are used as inputs and outputs, respectively, for the surrogate models developed.

Additional history-dependent inputs are also included in the model. NNs are used to establish a correspondence between the inputs and the outputs, after appropriate training. The choice of obtaining the training dataset from virtual (rather than actual) experiments is driven by two reasons: i) the fact that in virtual experiments, the material's response is well-defined and known in detail and ii) the desire to perform a feasibility study for this approach, before embarking in an extensive experimental campaign.

The paper is structured as follows. In Section 5.2 we illustrate the design of the virtual test specimens, of the FE simulations of their response, and of the analysis of the simulation data; Section 5.3 presents the strategies to create the training dataset and to implement the surrogate models; results are presented and discussed in Section 5.4.

5.2 Design and Analysis of the Virtual Experiments

5.2.1 Virtual test specimen

Performing an accurate and complete characterisation of the multiaxial stress-strain response of solids is challenging, costly and requires equipment such as triaxial test machines, which are unavailable to most materials engineers. However, applying a combination of axial strain and torsional rotation to a thin-walled axisymmetric material specimen (which is the strategy pursued in this study) is relatively inexpensive and it results in approximately uniform normal and shear stresses on the specimen's gauge portion; this allows exploring the material's response in plane stress.

The design of the test specimen was performed to minimise the variability of the normal and shear strains and stresses within the gauge portion, and to prevent compressive and torsional buckling and wrinkling during the (virtual or real) experiments. The geometry of the specimen, sketched in Figure 5.1, was selected considering the existing literature on fatigue and cyclic plasticity testing [17-20]. The detailed sizing of the specimen was performed with the aid of FE simulations of its elastic-plastic response in pure tension, pure compression and pure torsion; the simulations served to assess and maximise the uniformity of the strains and stresses in the gauge portion; checks were performed to ensure that compressive and torsional elastic buckling did not occur, based on theoretical predictions for a thin-walled hollow cylinder (from [21]), with the conservative assumption of simply-supported boundary conditions at the ends of the cylinder. The final dimensions are indicated in Figure 5.1.

5.2.2 Finite Element analyses

All simulations were conducted using the commercially available software Abaqus Standard [22]. The material of the virtual specimens was taken as isotropic linear elastic (with Young's modulus of $100\,\text{GPa}$, Poisson's ratio $\nu = 0.3$), with rate-independent J2 plasticity and isotropic hardening (with initial yield stress $\sigma_Y = 1\text{GPa}$ and constant hardening modulus $H = \partial\sigma_Y / \partial\hat{\varepsilon}_{pl} = 5\text{GPa}$, where $\hat{\varepsilon}_{pl}$ represents the von Mises equivalent plastic strain).

The geometry of the FE model coincided with that shown in Figure 5.1, comprising the gauge portion and both specimen shoulders, but excluding the gripping portions of the

specimen. The domain was meshed by solid, 8-noded hexahedral elements with reduced integration (type C3D8R, in Abaqus). After a mesh convergence study, the gauge portion of the specimen was discretised by a structured mesh with elements of dimensions 0.3 and 0.5 mm in the radial and axial directions, respectively, and 80 elements along the circumferential direction, as shown in Figure 5.1 (c).

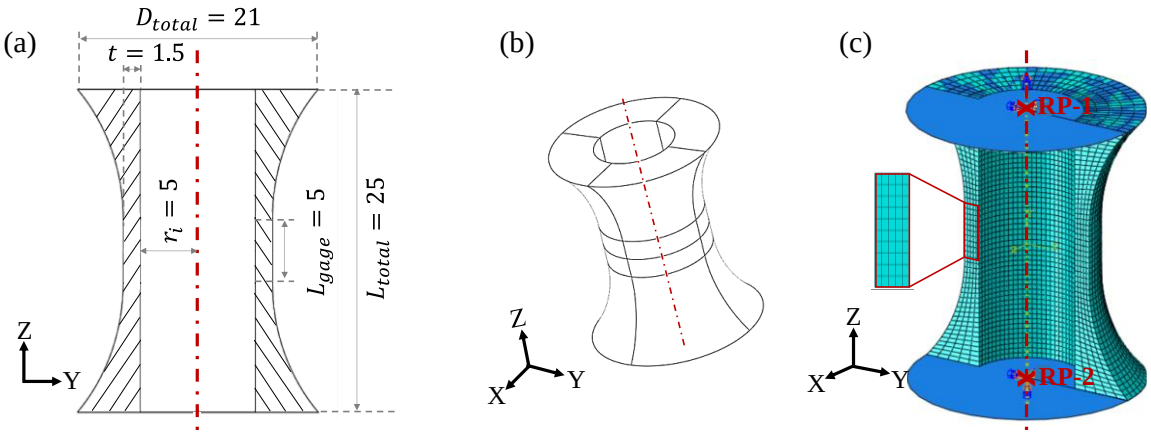


Figure 5.1. The geometry of the virtual specimen; (a) cross-sectional view; (b) 3-D view; (c) FE mesh and boundary conditions (all dimensions in mm).

Two analytical rigid surfaces were defined at the top and bottom of the specimen and connected to the nodes at the ends of the specimen via tie constraints. Reference points were introduced for both rigid surfaces; one of the reference points had all 6 degrees of freedom constrained to vanish; the other reference point had all degrees of freedom set to zero, with the exception of the translation along direction *y* and the rotation about the *y* axis. Although in principle they over-constrain the specimen's ends compared to a real test, these boundary conditions were chosen for the simplicity of their implementation, after a preliminary study which showed that the presence of the additional constraints on the radial displacements of nodes at the specimen's ends did not affect the stress versus strain histories recorded in the virtual tests. Axial and

torsional loading was applied by prescribing appropriate translation and rotation histories using the "amplitude" tool of Abaqus; details of this will be given below.

The axial force and torque applied to the specimen during the virtual tests coincided with the reaction force and torque at the loading reference point, and were recorded as a function of time during the simulations. Knowledge of the specimen's geometry allowed calculating the applied true stresses (axial stress σ_z and shear stress τ); the displacements of appropriate nodes on the surface of the specimen (within the gauge portion) were tracked and used to calculate the history of the normal strains in the axial and circumferential direction (ε_z and ε_θ, respectively) and of the shear strain $\varepsilon_{\theta z}$; we also checked that the radial strain ε_r was approximately equal to ε_θ, as expected for this isotropic material at small strains.

The results of the multiple virtual experiments conducted were in line with the expected response of the material, in terms of the elastic compliance, shape, magnitude and symmetries of the initial yield locus, as well as hardening characteristic. This reassures us that the design of the specimen was adequate to characterise the material's response.

5.3 Implementation of the Surrogate Models

5.3.1 Generation of the training data set

We now illustrate the assembly of the training dataset for the surrogate constitutive models. The objective was to sample, as uniformly as possible, the input space for the surrogate models; more precisely, to sample the space of the inputs that can be

controlled during the virtual tests, i.e. the average axial and shear strains ε_z and $\varepsilon_{\theta z}$ (respectively) in the gauge portion of the specimen. A further requirement was that such strains were sufficiently small to avoid the possibility of damage (in real measurements) and of strain localisation and other instabilities, as well as strain-induced anisotropy (in both virtual and real measurements).

Random histories of ε_z and $\varepsilon_{\theta z}$ were generated starting from an initial undeformed configuration; such histories comprise a random sequence of imposed deformation steps $\left(\Delta\varepsilon_z, \Delta\varepsilon_{\theta z}\right)$, each comprised between a minimum and maximum value, and terminating when one of the imposed strain components reached a limiting value, taken in this study as 0.04 for the engineering values of both ε_z and $\varepsilon_{\theta z}$. Mathematically:

$$\begin{aligned} \Delta\varepsilon_z &= \text{sign}\left(0.5-r\right)\left[\Delta\varepsilon_{\min} + r\left(\Delta\varepsilon_{\max} - \Delta\varepsilon_{\min}\right)\right]; \\ \Delta\varepsilon_{\theta z} &= \text{sign}\left(0.5-r\right)\left[\Delta\varepsilon_{\theta z\min} + r\left(\Delta\varepsilon_{\theta z\max} - \Delta\varepsilon_{\theta z\min}\right)\right]. \end{aligned} \tag{1}$$

where *r* is a random number generated from a uniform distribution in the interval $\left[0,1\right]$. In this study we choose $\Delta\varepsilon_{z\min} = \Delta\varepsilon_{\theta z\min} = 0.005$ and $\Delta\varepsilon_{z\max} = \Delta\varepsilon_{\theta z\max} = 0.01$, to avoid extremely small or extremely large deformation steps; this guarantees random stain histories that are not too long or too short (respectively), and it helps sampling wide ranges of imposed strain triaxiality. The term containing the sign() function in eqn. (1) applies a random sign to each of the strain increments. The histories of imposed axial displacement and torsional rotations were calculated assuming that the shoulder portions of the specimen were rigid.

An additional set of virtual tests was conducted to impose states of uniaxial stress (tension, compression and shear) on the specimen, with the objective of determining the compliance matrix of the material $\mathbf{S}$. This was defined as

$$\begin{pmatrix} \Delta\varepsilon_z \\ \Delta\varepsilon_r = \Delta\varepsilon_\theta \\ \Delta\varepsilon_{\theta z} \end{pmatrix} = \begin{bmatrix} S_{11} & S_{12} & 0 \\ S_{12} & S_{22} & 0 \\ 0 & 0 & S_{33} \end{bmatrix} \begin{pmatrix} \Delta\sigma_z \\ 0 \\ \Delta\tau \end{pmatrix} = \begin{pmatrix} S_{11}\Delta\sigma_z \\ S_{12}\Delta\sigma_z \\ S_{33}\Delta\tau \end{pmatrix}. \qquad (2)$$

The components of $\mathbf{S}$ were determined by a least square fit of eqn. (2) through the first 80 increments of each of these simulations, in which the response was purely elastic.

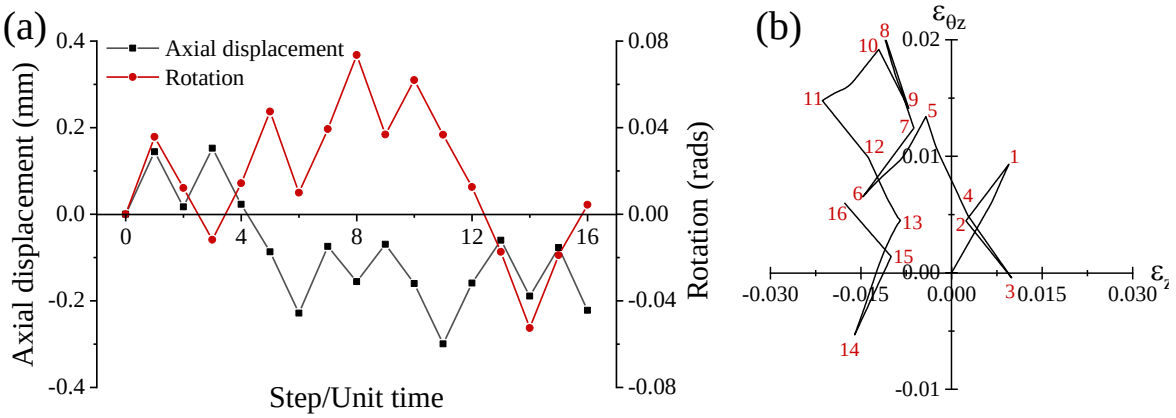


Figure 5.2. (a) Example of a 16-step history of imposed random displacement and rotation; (b) corresponding path in strain space.

Figure 5.2 illustrates a representative history of imposed random displacement/rotation and the corresponding path in the strain space. We note that each deformation step occurs over a time of 1. Fifty of such random strain histories were applied in the corresponding virtual experiments. The complete data set is shown in Figure 5.3 in strain space $(\varepsilon_z, \varepsilon_{\theta z})$ and stress space (σ_z, τ); the corresponding axial and shear strain

histories σ_z vs ε_z and τ vs $\varepsilon_{\theta z}$ are also presented. The time increment for the FE solution was set to 0.01, such that each deformation step (of time duration 1) comprised 100 time increments. The 50 random strain histories comprised a total of 552 deformation steps and therefore 55200 time increments. The number of random strain histories used to generate the training dataset was determined by analysing the sensitivity of the predictions to the size of the training dataset, as described in more detail in the Appendix (Supplementary material).

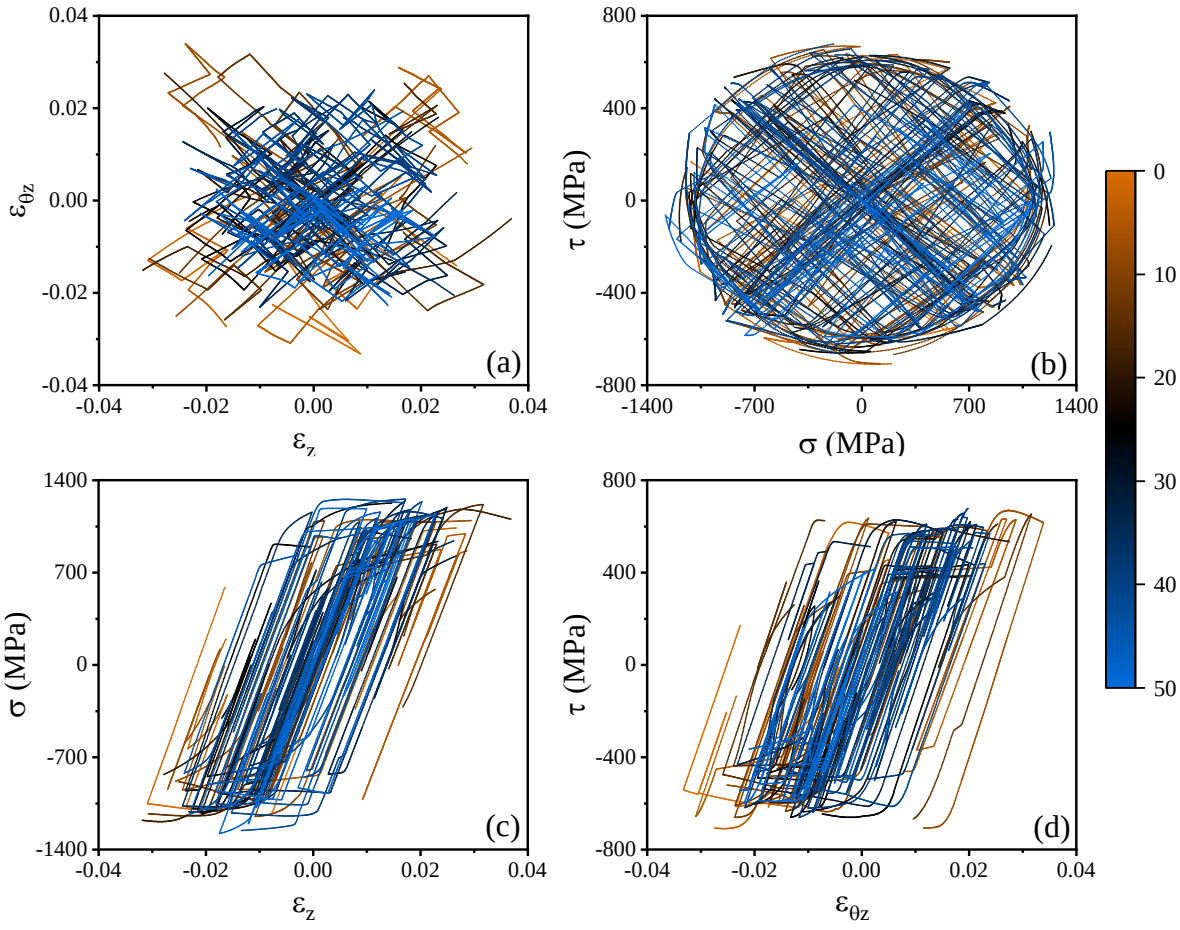


Figure 5.3. Visualisation of the training dataset (a) in strain space; (b) in stress space; (c) in axial stress versus strain space; (d) in shear stress versus strain space. Each of the

fifty different loading paths is associated to a different colour according to the colour code displayed on the right.

We note that the distribution of the data in true strain space (Figure 5.3 (a)) is not uniform in the square $\varepsilon_z, \varepsilon_{\theta z} \in [-0.04, 0.04]$; data are distributed more densely in the proximity of the origin, as all random strain histories start at the undeformed state; the density of data is also low near the boundary of the domain, due to the fact that deformation steps with ε_z or $\varepsilon_{\theta z}$ exceeding the maximum value of 0.04 were discarded and the corresponding random strain history was terminated. The probability density functions (PDF) and its cumulative counterparts (CDF) for ε_z and $\varepsilon_{\theta z}$ are shown in Figure 5.4. The uniformity of such distribution can be improved by creating additional random deformation histories and modifying the strategy (eqn.(1)), however the data in Figure 5.3 was found adequate to give a good accuracy of the surrogate models.

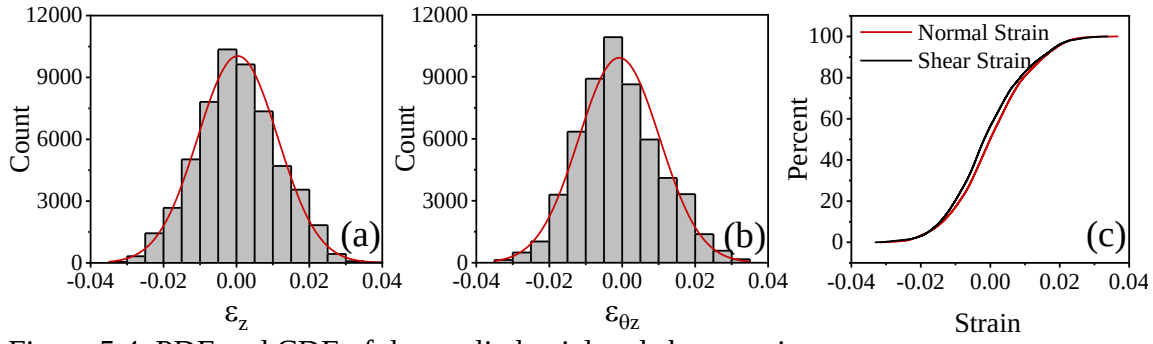


Figure 5.4. PDF and CDF of the applied axial and shear strains.

5.3.2 Separation of elastic and elastic-plastic increments

A further manipulation of the training dataset was performed in order to separate elastic from elastic-plastic increments. This was done by recording, for every increment, the

change in external work ΔW and dissipated plastic energy ΔPE, as obtained from the FE simulations. Each increment was then assigned a flag value Y given by

$$Y = \begin{cases} 1 & \Delta PE / |\Delta W| \geq 0.01 \\ 0 & \Delta PE / |\Delta W| < 0.01 \end{cases} \quad (3)$$

with $Y = 1$ corresponding to an elastic-plastic increment and $Y = 0$ corresponding to an elastic increment. The choice of using energies to perform such separation was dictated by convenience; in real mechanical tests, where such energies are not normally known, such separation can be performed by computing the plastic strain components. We note that the threshold of 0.01 used in eqn. (3) was determined by trial and error in a preliminary study, by assessing its effects on the accuracy of the classification. We found that very high values of the threshold imposed on ΔPE/|ΔW| caused a set of the elastic-plastic increments to be incorrectly categorised as elastic. Conversely, too small a threshold resulted in a portion of the elastic increments to be incorrectly classified as elastic-plastic. A range of values of such threshold resulted in a correct classification for all increments, and the value of 1% was chosen arbitrarily within such range.

Figure 5.5 visualises the same dataset as in Figure 5.3 after exclusion of the elastic increments with $Y = 0$; this comprises 16500 elastic-plastic increments.

5.3.3 Surrogate models

Feed-forward neural networks (NNs) are used here to construct surrogate constitutive models based on the data presented above. A summary of how NNs work can be found in [23]. The NNs were developed and trained in TensorFlow 2.0 [24]. Our objective is

to develop constitutive models that can be used in numerical simulations; these consist of computational frameworks receiving as input a tentative increment in the strain vector at a material point and returning the corresponding increment in the stress vector.

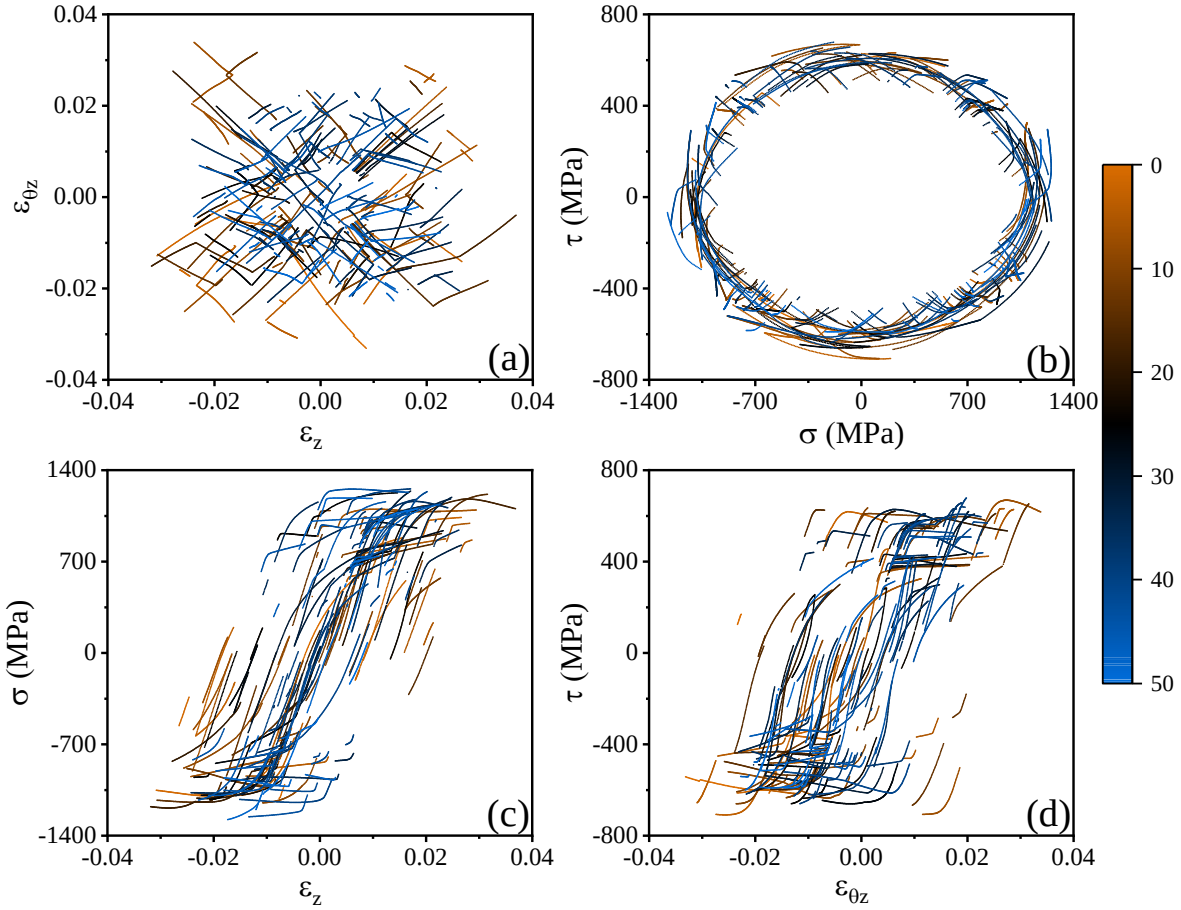


Figure 5.5. Visualisation of the plastic increments in the training dataset (a) in strain space; (b) in stress space; (c) in axial stress versus strain space; (d) in shear stress versus strain space. Each of the fifty different loading paths is associated to a different colour according to the colour code displayed on the right.

Two different surrogate models are presented in this study, and their architecture is summarised in Figure 5.6. Model I performs a simple regression to update the stress

state over each simulation increment. Model II first performs a classification step, to distinguish elastic from elastic-plastic increments; then, if the increment is elastic, it updates the stress according to the equations of elasticity; if the increment is elastic-plastic, it uses a NN to perform a regression similar as that in Model I.

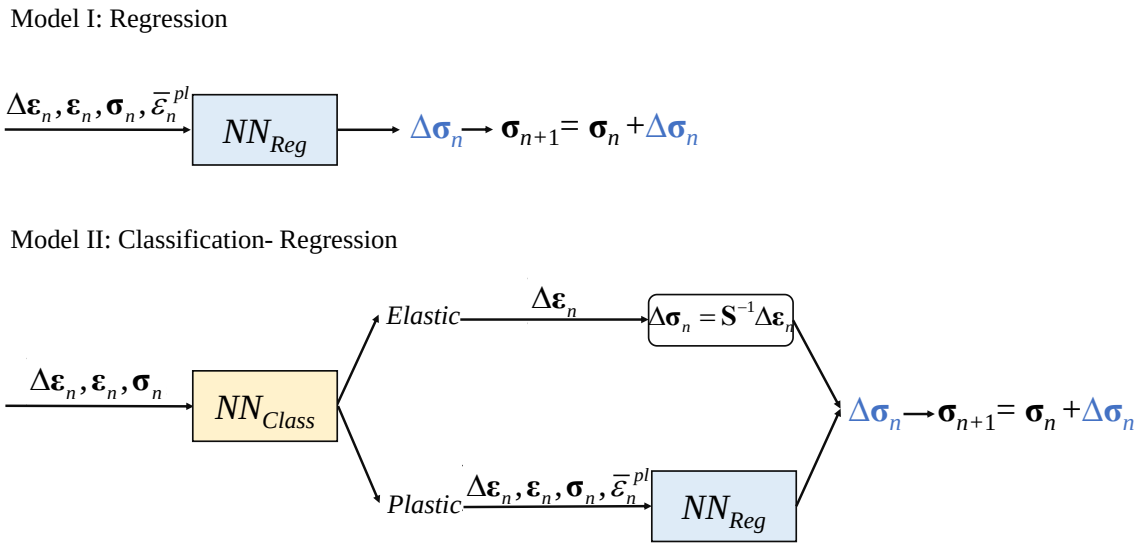


Figure 5.6. Schematic of the two surrogate models.

Before proceeding to describe the details the two surrogate models, we define

$$\boldsymbol{\varepsilon}_n = \begin{pmatrix} \varepsilon_z \\ \varepsilon_r = \varepsilon_\theta \\ \varepsilon_{\theta z} \end{pmatrix}; \quad \boldsymbol{\sigma}_n = \begin{pmatrix} \sigma_z \\ \sigma_r = \sigma_\theta = 0 \\ \tau \end{pmatrix}; \quad \Delta\boldsymbol{\varepsilon}_n = \boldsymbol{\varepsilon}_{n+1} - \boldsymbol{\varepsilon}_n; \quad \Delta\boldsymbol{\sigma}_n = \boldsymbol{\sigma}_{n+1} - \boldsymbol{\sigma}_n; \tag{4}$$

as the current strain vector, current stress vector, strain increment vector, and stress increment vector, respectively; here n is an index denoting the current state while $n+1$ denotes the state at the end of the simulation increment considered.

Considering the relatively small deformations applied to the specimens, we assume that additive strain decomposition applies, i.e.

$$\boldsymbol{\varepsilon} = \boldsymbol{\varepsilon}^{el} + \boldsymbol{\varepsilon}^{pl} = \mathbf{S}\boldsymbol{\sigma} + \boldsymbol{\varepsilon}^{pl} . \tag{5}$$

We shall also make use of the current accumulated von Mises plastic strain, defined as

$$\begin{aligned} \bar{\varepsilon}_n^{pl} &= \sum_{i=1}^{n} \Delta\bar{\varepsilon}_i^{pl} = \sum_{i=1}^{n} \sqrt{\frac{2}{3}\Delta\boldsymbol{\varepsilon}_i^{pl}\Delta\boldsymbol{\varepsilon}_i^{pl}} \\ &= \sum_{i=1}^{n} \sqrt{\frac{2}{3}\left[\left(\Delta\varepsilon_z^{pl}\right)_i^2 + 8\left(\Delta\varepsilon_{\theta z}^{pl}\right)_i^2 + 2\left(\Delta\varepsilon_r^{pl}\right)_i^2\right]}. \end{aligned} \tag{6}$$

Model I: This model performs, at every increment, the regression

$$\Delta\boldsymbol{\sigma}_n = NN_R\left(\Delta\boldsymbol{\varepsilon}_n, \boldsymbol{\varepsilon}_n, \boldsymbol{\sigma}_n, \bar{\varepsilon}_n^{pl}\right). \tag{7}$$

As the material studied is elastic-plastic, its response is expected to be history-dependent. In this model, $\boldsymbol{\varepsilon}_n, \boldsymbol{\sigma}_n$ represent the current state of the material while $\bar{\varepsilon}_n^{pl}$ quantifies the effects of the previous history of plastic deformation. After the regression (7), the increments in the plastic strain vector are calculated as

$$\Delta\boldsymbol{\varepsilon}_n^{pl} = \Delta\boldsymbol{\varepsilon}_n - \mathbf{S}\Delta\boldsymbol{\sigma}_n \tag{8}$$

and the new accumulated plastic strain is computed from eqn. (6). The hyperparameters of the network NN_R were decided by a trial and error procedure. The final network had two hidden layers with 128 neurons each. All inputs and outputs were scaled by the minmax() function [25], and ReLU [26] was the chosen activation function for all hidden layers. The training dataset was split into two portions, equal to 10% and 90% of the total, which were randomly selected as testing and training data, respectively. The Mean Absolute Error (MAE, [25]) was used as the loss function after a preliminary study. The training of the NN was performed by backpropagation using the Adam

optimiser [27], with a number of epochs set to 70,000, a batch size of 200 and a learning rate of 0.001.

Model II: In a general increment in an FE simulation, two distinct behaviours (elastic or elastic-plastic) can be activated at each material point. The elastic response is simple to predict from knowledge of the compliance matrix **S**, while predicting the non-linear and history-dependent elastic-plastic response represents the real challenge. In Model II, we separate the two types of predictions, in an attempt to improve the surrogate model and to reduce its computational cost.

As shown in Figure 5.6, the first step consists of a classification exercise to distinguish elastic from elastic-plastic increments. Mathematically

$$Y = NN_C\left(\Delta\boldsymbol{\varepsilon}_n, \boldsymbol{\varepsilon}_n, \boldsymbol{\sigma}_n\right) \tag{9}$$

where Y is the flag defined in eqn. (3) ($Y=1$ corresponding to an elastic-plastic increment and $Y=0$ corresponding to an elastic increment). NN_C comprises 2 hidden layers containing 64 neurons each. The inputs were scaled by the minmax() function; ReLU was the chosen activation function for the 2 hidden layers while sigmoid [26] was used for the output layer. A special dataset was assembled for this classification exercise, by selecting an equal number of datapoints (increments) with $Y=1$ and $Y=0$; the ratio of training to testing datapoints was again set to 90/10. The Binary Cross-Entropy (BCE) was the chosen loss function, as in [11]. The training of the NN was performed by backpropagation using the Adam optimiser [27], with 10,000 epochs, a

batch size of 100 and a learning rate of 0.001. The analysis of the confusion matrix [25] showed that the classification was accurate in 99.84% of the cases.

For increments classified as elastic ($Y = 0$), the stress vector was updated as

$$\Delta\boldsymbol{\sigma}_n = \mathbf{S}^{-1}\Delta\boldsymbol{\varepsilon}_n . \tag{10}$$

For elastic-plastic increments, NN_R was used to predict the increment in stress vector (eqn.(7)); the plastic strain increments were calculated according to eqn.(8), which allowed updating the accumulated plastic strain (eqn.(6)). In the case of Model II, NN_R was trained using all datapoints with $Y = 1$; with the exception of the batch size, now set to 100 due to the reduced size of the dataset, all other parameters were identical to those reported above for Model I.

5.3.4 Assessment of the accuracy of the surrogate models

To test the fidelity of the surrogate models developed above, we proceeded as follows. Twenty additional random strain histories were generated, and the corresponding virtual experiments were performed. This provided a set of datapoints (each corresponding to one increment from such simulations) which had not been seen by the surrogate models during their training. These were generated using the same procedure described in Section 5.3.1. An example of such unseen strain histories and the corresponding stress histories are shown in Figure 5.7, while Figure 5.8 simultaneously presents 7 of such random strain histories.

Both Model I and Model II were used to predict the stress versus strain responses corresponding to the unseen random strain histories. For each of such histories, starting from the initial stress- and strain free configuration ($\boldsymbol{\varepsilon}_{n=1} = 0$, $\boldsymbol{\sigma}_{n=1} = 0$), a sequence of strain increments $\Delta\boldsymbol{\varepsilon}_n$, coinciding with those in the FE simulations (or virtual tests, representing here the ground truth), was provided as an input to the surrogate models; in each increment, the procedure in Section 5.3.3 was used to update the corresponding increments in stress vector and accumulated plastic strain. This allowed constructing predictions of the stress histories corresponding to each unseen random strain history.

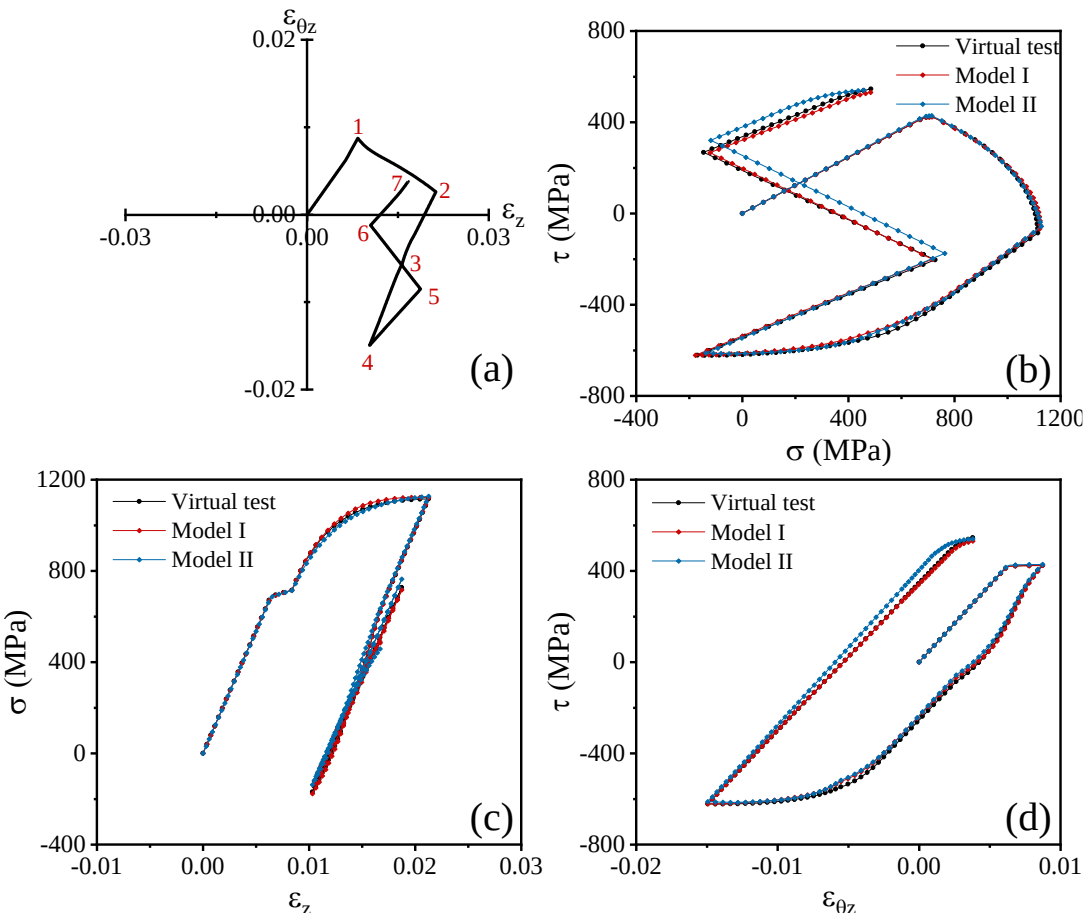


Figure 5.7. (a) One of the random strain histories used to assess the surrogate models; (b) Stress history corresponding to the strain history in (a), including the predictions of

the surrogate models; (c) normal stress versus strain history and predictions of the surrogate models; (d) shear stress versus strain history and predictions of the surrogate models.

5.4 Results and Discussion

The predictions of the surrogate models are compared to the ground truth (results of the virtual tests) in Figure 5.7 and Figure 5.8. Figure 5.7 presents the case of one selected random strain history; Figure 5.8 shows the same information as in Figure 5.7, but for the case of 7 selected random strain histories, to illustrate the accuracy of the models in wider regions of the strain and stress spaces.

We find that both surrogate models are in excellent agreement with the virtual tests. Both models capture the expected isotropy and symmetry of the material's response, the yield locus corresponding to von Mises plasticity, and the details of the strain hardening characteristic of the solid. The accuracy of the surrogate predictions persists along most of the complex, non-monotonic, non-proportional strain paths considered; minor errors can be seen in the final parts of the random strain paths, due to accumulation of the error after a large number of increments, but also due to the relative scarcity of training datapoints for the NNs in those final parts of the random strain paths. We refer the reader to the Appendix (Supplementary material) for a brief discussion of the computational time required for the training and the use of the surrogate model.

The accuracy of the predictions reassures us that the proposed architecture of the surrogate models, including the history-dependent evolution of the accumulated plastic

strain, is adequate to capture the material response of the isotropic von Mises solid considered in this study. We note that in [11] we showed that similar architectures of the surrogate models were also adequate for fully dense solids displaying a pressure-sensitive response.

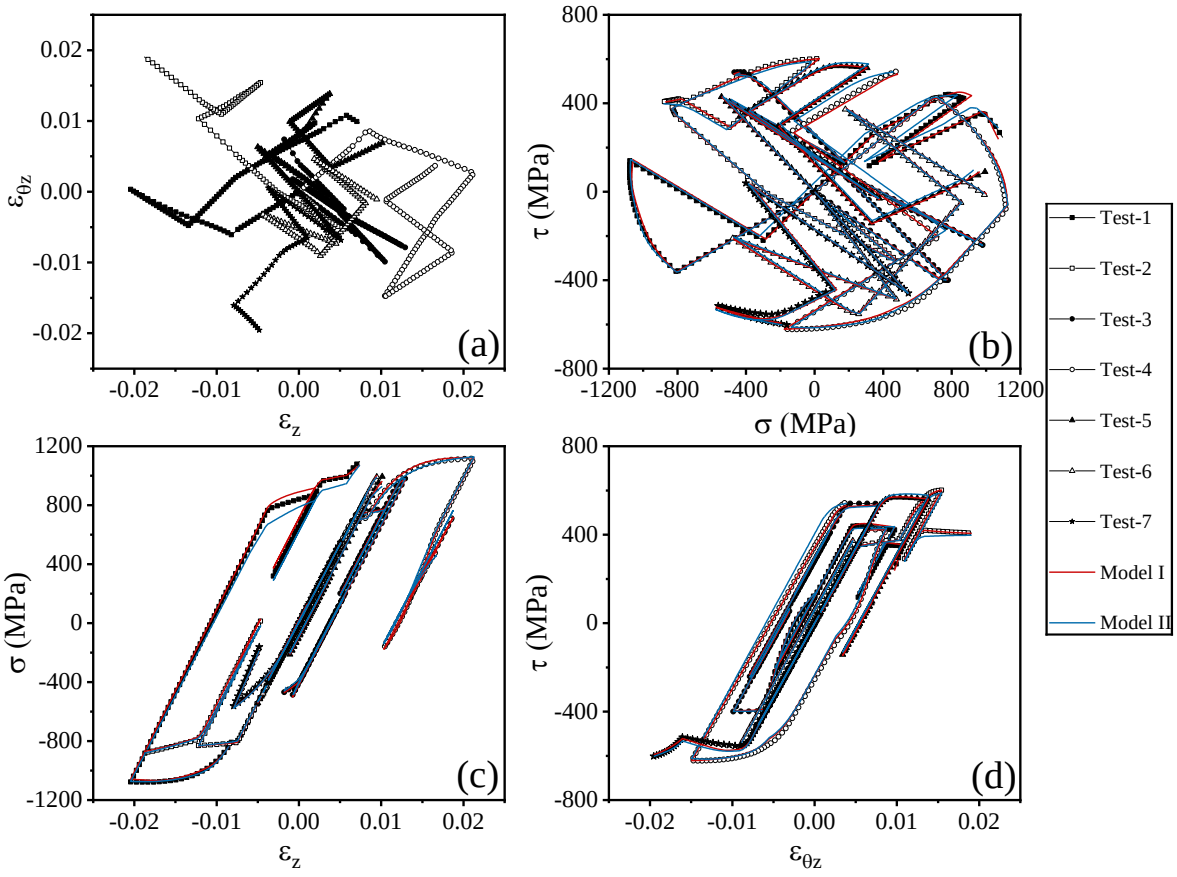


Figure 5.8. (a) Strain histories corresponding to seven random simulations used to assess the surrogate models; (b) Stress history corresponding to the strain history in (a), including the predictions of the surrogate models; (c) normal stress versus strain history and predictions of the surrogate models; (d) shear stress versus strain history and predictions of the surrogate models.

The obvious limitation of the surrogate models presented here that they are not necessary accurate in regions of the input space scarcely populated by training datapoints. Such limitation can, however, be overcome by including additional coupon-level tests (real or virtual) to those considered here, for example biaxial or triaxial experiments. A complementary strategy could be to resort to physics-informed neural networks [28,29]: this would involve modifying the architecture of the surrogate models by enforcing appropriate constraints (for example: isotropy, symmetry and pressure-independence of the plastic response), including additional terms in the loss-function; it would however imply assuming a priori some features of the constitutive response. An additional development could be to include in the training dataset data measured in experiments involving non-uniform stress and strain fields, such as instrumented indentation or bending tests. We discuss this in the Appendix (Supplementary material).

5.5 Conclusions

We proposed a methodology to develop data-driven surrogate constitutive models which do not rely on any constitutive theory and are informed exclusively from the results of carefully designed random non-proportional, non-monotonic multiaxial tests. The aim of this study is to develop accurate numerical tools to predict the elastic-plastic response of materials prior to establishing valid theories describing their behaviour, and without any knowledge of their microstructure.

We described a strategy to conduct relatively inexpensive experiments on the material of interest and to accurately capture its response by surrogate models based on small

feed-forward NNs, including the design of suitable specimens and of the imposed random strain histories.

We demonstrated that the proposed framework is very effective in the specific case examined, and that the surrogate models presented capture all details of the constitutive response assigned to the specimens in the virtual experiments.

5.6 Supplementary Material- Appendix

Dataset size and computational costs

The accuracy of the predictions was found to increase with the size of the training dataset, in the range investigated in this study. To illustrate such sensitivity of the predictions to the dataset size Figure.A.5.1 presents, for a selected test case, the evolution of the predictions when using datasets comprising 13800, 27600 and 55200 datapoints (i.e. 25%, 50% or 100% of the dataset produced). We progressively increased the training dataset size until the desired accuracy was achieved; we note however that even employing only 25% of the maximum number of training datapoints, the accuracy of the prediction would be more than adequate for a large range of applications. In this study the number of increments in the virtual tests was chosen to be the same as used by Abaqus. In real experiments more training datapoints could be extracted from each test, by just subdividing the measured histories of stress and strain in smaller or larger time increments.

The training time of the NN was of approximately 7 hours using the complete training dataset (55200 increments) and an ordinary computer (2 x 2.6 GHz Intel Xeon CPU E5-

2640 v3 processors, 64 GB of RAM). The time for training was approximately proportional to the size of the training dataset. With regards to the time required to perform the predictions, it is interesting to compare the performance of our surrogate model to that of the ordinary von Mises J2 isotropic plasticity model implemented in Abaqus. The ordinary model is slightly faster than the surrogate model in evaluating the stress update corresponding to a single prescribed increment in strain, as the surrogate model involves more complex algebraic operations. However, the evaluation of the stress increment corresponding to a given strain increment involves, when using the ordinary model, a number of iterations, while the surrogate model does not require this.

To quantify the relative speed of the ordinary and surrogate constitutive models, the surrogate model was implemented into a UMAT subroutine [22] suitable for beam elements. FE simulations were conducted considering a single beam element (element type B33 of Abaqus) fully constrained at one end and loaded by the application of combined axial displacement and torsional rotation at the opposite end. The beam had a thin-walled circular cross-section. The simulation time was set to 1 and the maximum time increment was set to 0.005. The simulation was run 2 times, describing the material's behaviour with either the ordinary or the surrogate model. Both simulations completed with exactly 200 increments, each of duration 0.005, indicating that it was never necessary, in both cases, to reduce the time step. The simulation using the ordinary model was completed in 64 s, while that employing the surrogate model finished in 72 s. We note that in its current version, the UMAT subroutine performed one disk access at every evaluation, to read weights and biases of the NN; this step could be eliminated by employing a different coding structure. From this preliminary analysis

we conclude that the surrogate model has similar computational cost as the analytical von Mises constitutive description.

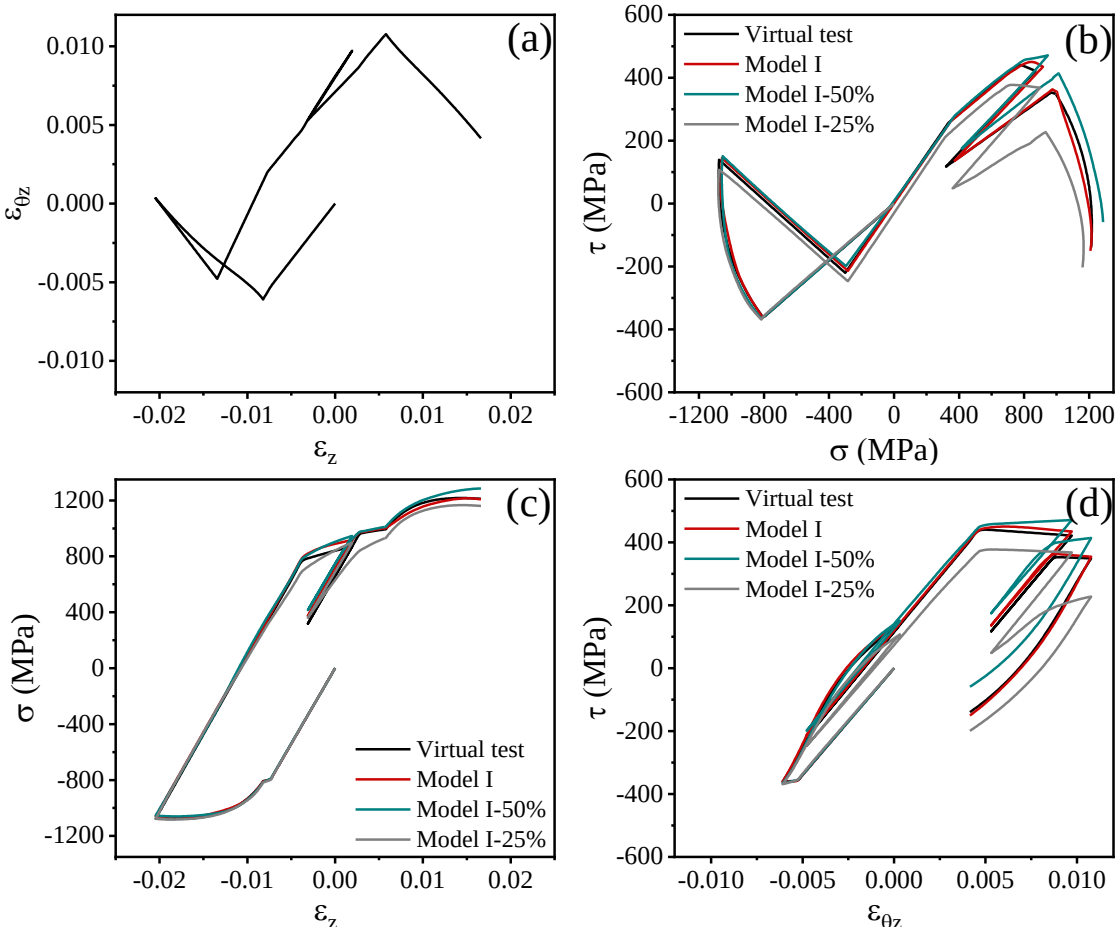


Figure A.5.1. Predictions of model I with different datasets. (a) Selected random strain history. (b) Resulting stress history. (c) Normal stress vs strain history and predictions (d) shear stress vs strain history and predictions.

Extension of the surrogate models to 6-dimensional stress and strain spaces

The surrogate models presented in this paper are expected to be accurate only in the input space defined by the training datapoints, in this case only for plane states of stress comprising one normal and one shear stress component. We note that, in numerous

engineering applications, components are typically subject to deformation and loading within such range (e.g. loading of 2D beams and thin plates and shells). In other applications however the strain and stress tensors possess up to 6 non-negligible components. The neural networks can be generalised to provide predictions outside the domain of the training datapoints, but such predictions would extrapolate from the training data and likely they would not be accurate. The domain of applicability of the surrogate constitutive models can be extended following at least two strategies, outlined below.

The first strategy would involve making assumptions on the constitutive behaviour of the material; for example, for the isotropic elastic-plastic materials subject of this study, one could postulate a certain form of the functional dependence of the yield locus upon the stress and strain tensors and history variables, effectively adopting a chosen theoretical response. This approach however would require human judgement and it could be successful only in presence of a detailed understanding of the microstructure and of the active deformation mechanisms of the solid under consideration; as such, it would not be applicable for recently developed materials of unknown constitutive behaviour.

To obtain theory-free constitutive models it would be necessary to extend the ranges of input data spanned by the training datapoints. In practice, designing lab-scale experiments to span arbitrary six-dimensional states of stress and strain is not possible. In this study we focused on tension-torsion tests on thin-walled cylindrical specimens, as these are relatively easy to perform and allow obtaining approximately uniform states

of strain and stress in the specimen, from which training datapoints can be directly obtained. The availability of biaxial and triaxial tests would somewhat extend the scope of the surrogate model, but not make it fully general; such tests (triaxial tests in particular) are also rare and costly. In contrast structural tests, in which the states of stress and strain are not uniform, are substantially easier to perform and it has been previously shown [10] that such tests can be used to train data-driven models.

Multiple structural tests could be designed to explore the stress and strain space as required. For example, non-monotonic random indentation tests would allow exploring states of (non-uniform) stress and strain with a high degree of hydrostatic compression; random combined bending/torsion tests on monolithic beams would allow further exploring 3D deformation and loading; tension/torsion tests on specimens of very low aspect ratio would allow obtaining data characterised by high hydrostatic tension; multiaxial loading of specimens and structures with large stress concentrators would interrogate the material's response in presence of fully six-dimensional states of strain and stress.

In all the structural tests described above, the time histories of multiple displacements could be prescribed on the structure. Measurements would include the histories of the corresponding reaction forces, but an additional arbitrary number of surface strains and displacements could also be measured. A sufficiently rich set of lab-scale tests and structural tests could be used to train a surrogate model like that presented in this study, as follows: i) Discretise the set of loads, displacements and surface strain histories into small time increments, and split data in appropriate subsets for training, testing and

validation. ii) Implement and initialise a general surrogate constitutive model, based on NNs with similar features as those described in this study (e.g a UMAT subroutine for Abaqus). iii) Conduct FE simulations of all the tests performed, describing the constitutive response of the material by the surrogate model. iv) Use a multi- or single-objective optimisation algorithm to determine the optimal weights and biases of the NN, based on the difference between measurements and FE predictions over each time increment. Appropriate loss functions could be devised to assign different relative importance to lab-scale tests (those resulting in uniform stress and strain histories), and the different measurements performed in the structural tests. Clearly, each evaluation of the loss function during the optimisation would require conducting multiple FE simulations, therefore the training times required would be substantially longer than those reported in this study, but we expect that these to be still within reach using relatively inexpensive hardware.

5.7 References

[1] Matos, M. A. S., Pinho, S. T. & Tagarielli, V. L. Application of machine learning to predict the multiaxial strain-sensing response of CNT-polymer composites. Carbon. 146, 265-275 (2019).

[2] Matos, M. A. S., Pinho, S. T. & Tagarielli, V. L. Predictions of the electrical conductivity of composites of polymers and carbon nanotubes by an artificial neural network. Scripta Mater. 166, 112-12 (2019).

[3] Pathan, M. V. et al. Predictions of the mechanical properties of unidirectional fibre composites by supervised machine learning. Sci. Rep. 9, 13964 (2019).

[4] Mozaffar, M. et al. Deep learning predicts path-dependent plasticity. Proc. Natl. Acad. Sci. 116(52), 26414-26420 (2019).

[5] Ghavamian, F. & Simone, A. Accelerating multiscale finite element simulations of history-dependent materials using a recurrent neural network. Comput. Methods Appl. Mech. Eng. 357, 112594 (2019).

[6] Liu, Z., Wu, C. T. & Koishi, M. A deep material network for multiscale topology learning and accelerated nonlinear modeling of heterogeneous materials. Comput. Methods Appl. Mech. Eng. 345, 1138-1168 (2019).

[7] Huang, D., Fuhg, J. N., Weißenfels, C. & Wriggers, P. A machine learning based plasticity model using proper orthogonal decomposition. Comput. Methods Appl. Mech. Eng. 365, 113008 (2020).

[8] Jang, D. P., Fazily, P. & Yoon, J. W. Machine learning-based constitutive model for J-2 plasticity. Int. J. Plast. 138, 102919 (2021).

[9] Ghaboussi, J. & Sidarta, D. E. New nested adaptive neural networks (NANN) for constitutive modeling. Comput. Geotech. 22(1), 29-52 (1998).

[10] Ghaboussi, J., Pecknold, D. A., Zhang, M. & Haj-Ali, R. M. Autoprogressive training of neural network constitutive models. Int. J. Numer. Methods Eng. 42(1), 105-126 (1998).

[11] Ge, W. & Tagarielli, V. L. A computational framework to establish data-driven constitutive models for time- or path-dependent heterogeneous solids. Sci. Rep. 11, 15916 (2021).

[12] Kirchdoerfer, T. & Ortiz, M. Data-driven computational mechanics. Comput. Methods Appl. Mech. Engrg. 304, 81-101 (2016).

[13] Stainier, L., Leygue, A. & Ortiz, M. Model-free data-driven methods in mechanics: material data identification and solvers. Comput. Mech. 64, 381-393 (2019).

[14] Kirchdoerfer, T. & Ortiz, M. Data-driven computing in dynamics. Int. J. Numer. Methods Eng. 113(11), 1697-1710 (2018).

[15] Eggersmann, R., Kirchdoerfer, T., Reese, S., Stainier, L. & Ortiz, M. Model-free data-driven inelasticity, Comput. Methods Appl. Mech. Engrg. 350, 81-99 (2019).

[16] Ibanez, R. et al. A manifold learning approach to data-driven computational elasticity and inelasticity. Arch. Comput. Methods Eng. 25(1), 47-57 (2018).

[17] Lamba, H.S. & Sidebottom, O.M. Cyclic Plasticity for nonproportional paths: Part 1- Cyclic Hardening, Erasure of Memory, and Subsequent Strain Hardening Experiments. J. Eng. Mater. Technol. 100(1), 96-103 (1978).

[18] Lamba, H.S. & Sidebottom, O.M. Cyclic Plasticity for nonproportional paths: Part 2- Comparison with Predictions of Three Incremental Plasticity Models. J. Eng. Mater. Technol. 100(1), 104-111 (1978).

[19] Zhang, J., Shi, X., Bao, R. & Fei, B. Tension-torsion high-cycle fatigue failure analysis of 2A12-T4 aluminum alloy with different stress ratios. Int. J. Fatigue. 33, 1066-1074 (2011).

[20] Mayer, H. Ultrasonic torsion and tension-compression fatigue testing: Measuring principles and investigations on 2024-T351 aluminum alloy. Int. J. Fatigue. 28, 1446-1455 (2006).

[21] Young, W. C. & Budynas R. G. Roark's Formulas for Stress and Strain 709-742 (McGraw-Hill, 2012).

[22] Dassault Systemes. Abaqus/CAE User's Guide 2017 (2016).

[23] Goodfellow, I., Bengio, Y. & Courville, A. Deep Learning (MIT Press, 2016).

[24] Singh, P. & Manure, A. Introduction to TensorFlow 2.0. In: Learn TensorFlow 2.0 1-24 (Apress Berkeley, 2020).

[25] Pedregosa, F. et al. Scikit-learn: machine learning in Python. J. Mach. Learn. Res.12, 2825-2830 (2011).

[26] Nwankpa, C., Ijomah, W., Gachagan, A., & Marshall, S. Activation functions: Comparison of trends in practice and research for deep learning. arXiv preprint arXiv:1811.03378 (2018).

[27] Kingma, D. P. & Ba, J. Adam: A method for stochastic optimization. arXiv preprint arXiv:1412.6980 (2014).

[28] Karniadakis, G. E. et al. Physics-informed machine learning. Nat. Rev. Phys. 3(6), 422-440 (2021).

[29] Wen, J., Zou, Q. & Wei, Y. Physics-driven machine learning model on temperature and time-dependent deformation in lithium metal and its finite element implementation. J. Mech. Phys. Solids. 153, 104481 (2021).

CHAPTER 6

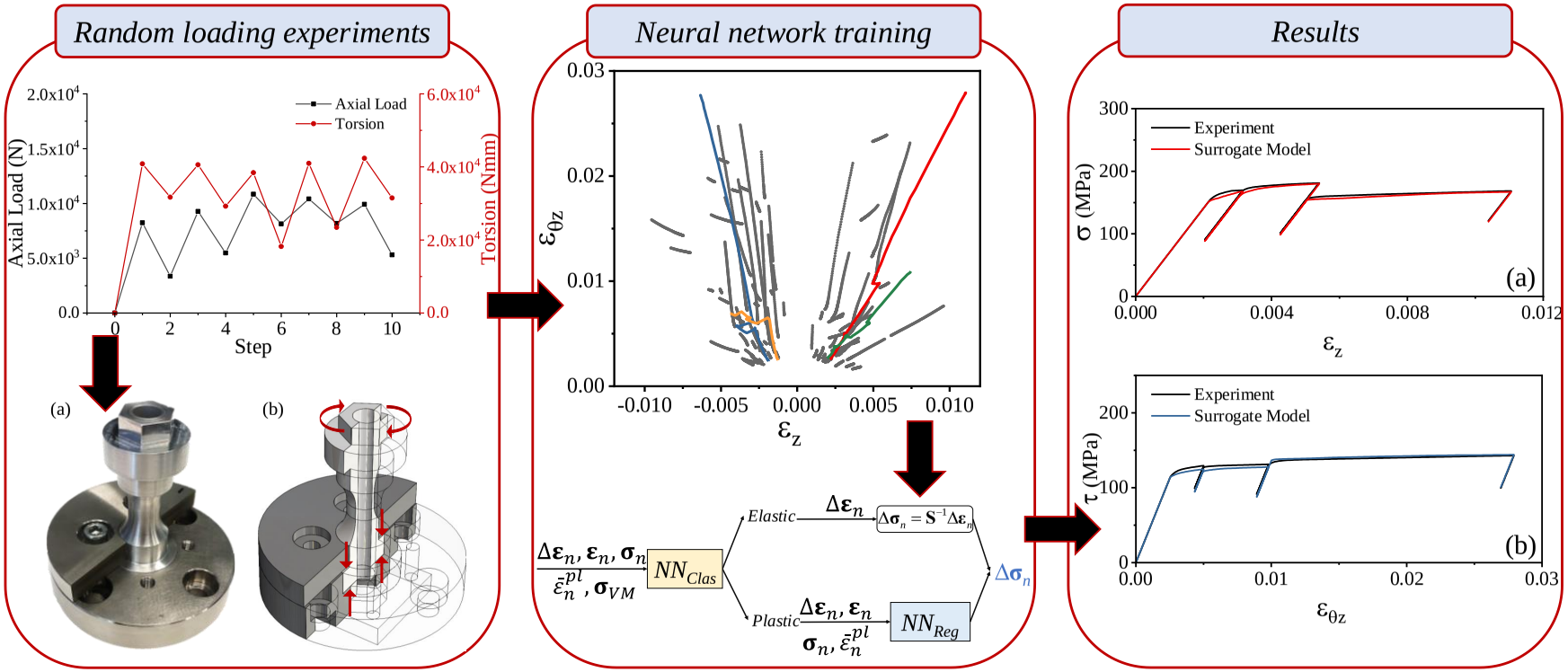
AN EXPERIMENTALLY GENERATED MACHINE LEARNING-BASED MATERIAL MODEL FOR NON-MONOTONIC AND NON-PROPORTIONAL LOADING

This Chapter presents a data-driven model of the multiaxial non-monotonic and non-proportional response of a metallic material. The main novelty of this study is the direct utilisation of experimental data corresponding to the real behaviour of the material.

Abstract

A surrogate constitutive model has been developed to predict the elastic-plastic behaviour of aluminium under combined non-proportional random loading. The proposed model, based on feed-forward neural networks, predicts how the materials will respond to random strain increments. The experimental data used to train the surrogate model comes from experiments in which a hollow, cylindrical test specimen is subjected to arbitrarily imposed levels of axial and torsional displacement. The data was divided into increments and machine learning was used to predict the change in stress in each strain increment. The neural networks were trained using stochastic gradient descent and backpropagation, and their accuracy was evaluated by predicting the material's response to different strain histories. The predictions of the model were validated by comparing them to experiments that were not used in the training process,

B. Tasdemir, A. Pellegrino, & V. Tagarielli, An experimentally generated machine learning-based material model for non-monotonic and non-proportional loading.



Keywords :Machine learning; Plasticity; Experimental mechanics; Surrogate models; Constitutive models; Neural network.

and it was found that the model predictions were in excellent agreement with the measurements.

6.1 Introduction

In recent years, the integration of machine learning techniques in materials science and engineering has demonstrated promising outcomes. It has been applied to the mechanics of solids with the goal of reducing the computational cost of simulations involving complex material behaviour by creating surrogate constitutive models or data-driven microstructure-properties relations [1-4].

Some researchers have focused on the response of heterogeneous solids, specifically two-phase composites, using data-driven approaches to predict the effects of their microstructure on mechanical behaviour [5]. Other researchers have worked on data-driven models for elastic-plastic solids, collecting training data from simulations or measurements of proportional loading histories [6,7,8] or from the results of structural tests [9].

More recently, researchers have begun leveraging a vast amount of information obtained from a combination of load cell measurements, experimental footage, and digital image correlation analyses to create a machine learning-based model utilizing experimental data. Li et al. [10] developed a modified Johnson-Cook plasticity model to accurately capture the unconventional temperature and strain rate dependencies of dual-phase steel specimens manufactured from steel sheets. The model comprises a von Mises yield surface, an anisotropic flow rule, a reference stress-strain curve defining

the rate-independent behaviour at room temperature, and a neural network function that depends on plastic strain, strain rate, and temperature. The authors demonstrated that machine-learning-based Johnson-Cook plasticity was capable to describe accurately all experimental data, including both global variables, i.e., forces and displacements, and local surface strain measurements. The model was subsequently further expanded in [11] introducing a new state variable to separate the influences of positive strain rate effect and strain aging (negative strain rate effect). Their research emphasised the potential of machine learning based approaches for the development of accurate phenomenological constitutive models. However, in these works the neural networks were developed and trained using an inverse procedure, which necessitates the execution of non-linear finite element analyses.

Cai et al [12] investigated the concurrent effects of printing parameters and strain rate on the dynamic response of additively manufactured fibre reinforced bio-composites with different layer thicknesses and hatch spacings. The experimental data showed a complex interaction between the manufacturing parameters and the strain rate. The authors used the obtained measurements to train and validate machine learning models correlating the dynamic strength with the printing parameters. The generated data-driven models were utilised to predict the strength of AM bio-composites produced with different parameters. The results highlight a good agreement between the experimental data and the predictions. However, the machine learning models predict the strength measured during monotonic experiments and do not provide information on the stress-strain characteristics.

Hamel et al [13] used full field synthetic digital image correlation data to calibrate hyperelastic constitutive models via Physics Informed Neural Networks (PINNs). In their work the authors demonstrated that physics informed machine learning can revolutionize the way full field surface displacement and force-displacement data from experiments are utilised for the calibration of constitutive models. Their method proved to be effective and insensitive to a reasonable amount of surface displacements data loss. However further investigation is needed to test the method on real experimental data.

Previously, we presented a test technique and computational framework for obtaining data-driven, surrogate constitutive models that capture the response of isotropic, elastic-plastic materials under combined normal and shear stresses. The models are based on feed-forward neural networks and are evaluated through virtual experiments simulating the response of a hollow, cylindrical, thin-walled test specimen to random strains. The study proposes a methodology for developing accurate numerical tools to predict the elastic-plastic response of materials without any knowledge of their microstructure through relatively inexpensive experiments. The proposed framework was found to be effective in the specific case studied and the surrogate models captured all details of the constitutive response [14].

In this study, the goal is to develop a surrogate constitutive model of solid materials that can predict the material's response to any type of combined shear-axial loading, including complex,non-monotonic and non-proportional deformation histories, by using experimental data. The developed methodology utilising the virtual experiments

in the previous work is applied to the real experimental data [14]. Experiments are conducted to measure the response of a hollow cylindrical thin-walled test specimen to random histories of imposed non-proportional axial displacement and torsional rotation. The results of these experiments are processed in the same way as in the established method, resulting in time histories of the average direct and shear stresses and strains in the specimen's gauge portion. In order to develop a comprehensive understanding of the material's response, experiments are conducted using multiple random deformation histories. These histories are broken down into small time increments and the stresses and strains at the beginning and end of each increment are used as input and output data for the surrogate models being developed. Neural networks are then used to establish a relationship between the inputs and outputs after training.

The paper is structured as follows: Section 6.2 provides information about the design and analysis of the experiments. Section 6.3 explains the process of creating the data-driven model, and the results are presented and discussed in Section 6.4.

6.2 Design and Analysis of the Mechanical Tests

6.2.1 Material and specimen geometry

Bars of Aluminium Grade 6082 T6 of 30mm diameter were obtained from Smiths Metal Centres. Hollow, cylindrical, thin-walled specimens with axisymmetric geometry were manufactured using Computer Numerical Controlled (CNC) machines following the design in Figure 6.1. The inclusion of upper and lower cylindrical shoulders, along with hexagonal ends, served the purpose of facilitating the secure connection of the

specimens to the designated fixture. The middle section is carefully designed to enable the reliable measurement of normal and shear strain histories.

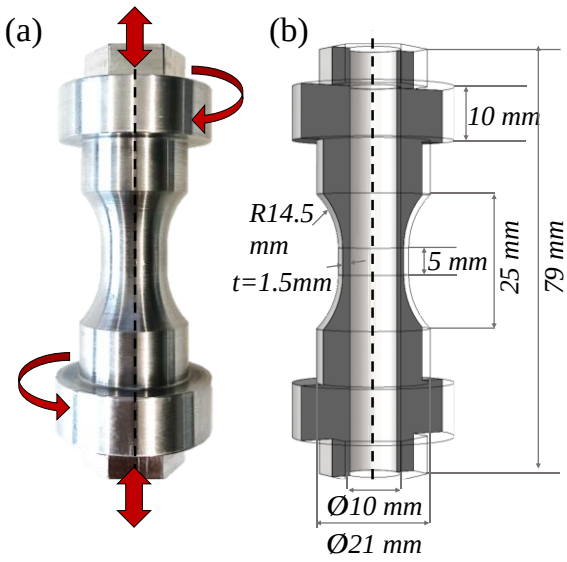


Figure 6.1. Specimen geometry.

Obtaining the multiaxial stress-strain response of a material is challenging, expensive, and requires specialized equipment such as triaxial testing machines. Therefore, in this study, an alternative cost-effective method was used by applying a combination of axial strain and torsional rotation to a thin-walled, axisymmetric specimen. This method results in approximately uniform normal and shear stresses on the specimen's gauge portion, enabling the exploration of the material's response in plane stress conditions.

The geometry of the specimen, as depicted in Figure 6.1, was chosen in consideration of existing literature pertaining to combined axial-torsional loading experiments [15-18]. The final design of the specimen was accomplished by employing finite element simulations to analyse its elastic-plastic response under pure tension, pure compression, and pure torsion. These simulations were instrumental in evaluating and optimizing the uniformity of strains and stresses within the gauge portion.

The geometry of the specimen was meticulously designed with the objective of minimizing the variability of normal and shear strains and stresses within the gauge portion, while also mitigating compressive and torsional buckling as well as wrinkling during the experiments. Additionally, thorough assessments were performed to ensure that compressive and torsional elastic buckling were avoided, employing theoretical predictions for a thin-walled hollow cylinder [19]. Conservative assumptions were made; these considered simply-supported boundary conditions at the ends of the cylinder.

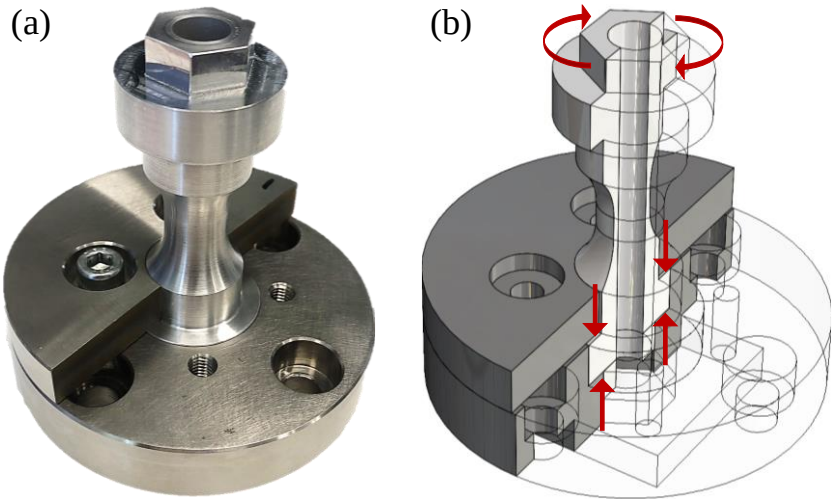


Figure 6.2. (a) View of the combined loading fixture; (b) CAD drawing of the combined loading fixture depicting the details.

6.2.2 Experimental setup and procedure

The aluminium specimen was mounted to a steel loading fixture using hexagonal ends and circular shoulders on both extremities, as depicted in Figure 6.2. The hexagonal ends were specifically designed to facilitate the transmission of torsional loading, while

the cylindrical shoulders were intended for the transmission of tension and compression loadings. The half-circle cylindrical caps of the fixture were bolted to the lower portion, sandwiching the circular shoulders of the specimen. The identical procedure was applied to both ends of the axisymmetric specimen. The fixture was loaded by an electro-mechanical screw-driven testing machine via mounting pins. Axial and torsional loadings were applied in load control, and the digital image correlation (DIC) method was employed to measure the axial and rotational strains within the gauge portion. DIC images were captured at a rate of 1 frame per second, while load measurements were recorded at a frequency of 20 Hz. The correlation between the images and the load measurement was performed during post-processing. The load was measured by resistive 100kN axial and 1000 Nm torsional load cells.

Fourteen different specimens were subjected to random axial-torsional strains. Each experiment consisted of 10 loading steps, in each of which a random loading history of tension-torsion or compression-torsion was imposed on the specimen. Each loading step was followed by an unloading step. Loadings were designed to incrementally reach a specified level of equivalent Von Mises Stress $(\boldsymbol{\sigma}_{VM})_{2i-1}$, $(i = 1,2,\ldots,5)$ in an increasing manner ensuring an expansion in the yield surface during each loading step. Likewise, each unloading step aimed to reach a predetermined level of equivalent Von Mises Stress $(\boldsymbol{\sigma}_{VM})_{2i}$, $(i = 1,2,\ldots,5)$. For each of these steps, a random combination of average axial and shear stresses (σ_z and $\sigma_{\theta z}$, respectively) was calculated, and the specimen was subjected to corresponding axial and torsional loads as follows.

$$
\begin{aligned}
&(\sigma_{VM})_{2i-1} = (\sigma_{VM})_{2i-3} + 10MPa;\\
&(\sigma_{VM})_{2i} = r[-20,0] + 200MPa;\\
&(\Delta\sigma_z)_i = r[\Delta\sigma_{zmin}, (\sigma_{VM})_i];\\
&\Delta\sigma_{\theta z} = \sqrt{\frac{(\sigma_{VM})_i{}^2 - (\Delta\sigma_z)_i{}^2}{3}}.
\end{aligned}
\tag{1}
$$

where r is a random number function that defines the values in the specified interval. The first value of the Von Mises Stress value is defined as $(\sigma_{VM})_1 = 270\ MPa$. We chose $\Delta\sigma_{zmin} = 20\ MPa$. Rates of axial and torsional loadings were defined in a random yet dependent manner as it was aimed for the axial and torsional loads to reach their target values at each loading /unloading step simultaneously. The rotary loading rate was defined randomly between 200 Nmm/s and 350 Nmm/s and the corresponding axial loading rate was calculated accordingly.

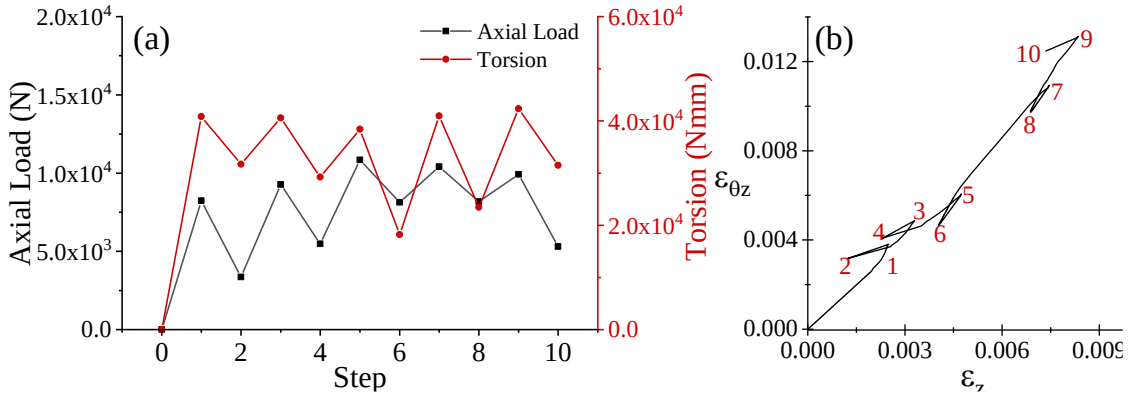


Figure 6.3. (a) Example of a 10-step history of imposed random displacement and rotation; (b) corresponding path in strain space.

Figure 6.3 (a) illustrates a representative random axial-torsion loading history applied in one of the tension-torsion experiments, and Figure 6.3 (b) depicts the corresponding true strain path in the strain space. The conversion between nominal and true stresses

and strains was conducted with the usual formulae for plastically incompressible solids (we note that the material used is virtually pore-free). The material exhibited the expected stress versus strain response, exhibiting a Young's modulus of approximately 71 GPa, and a shear modulus of 24 GPa.

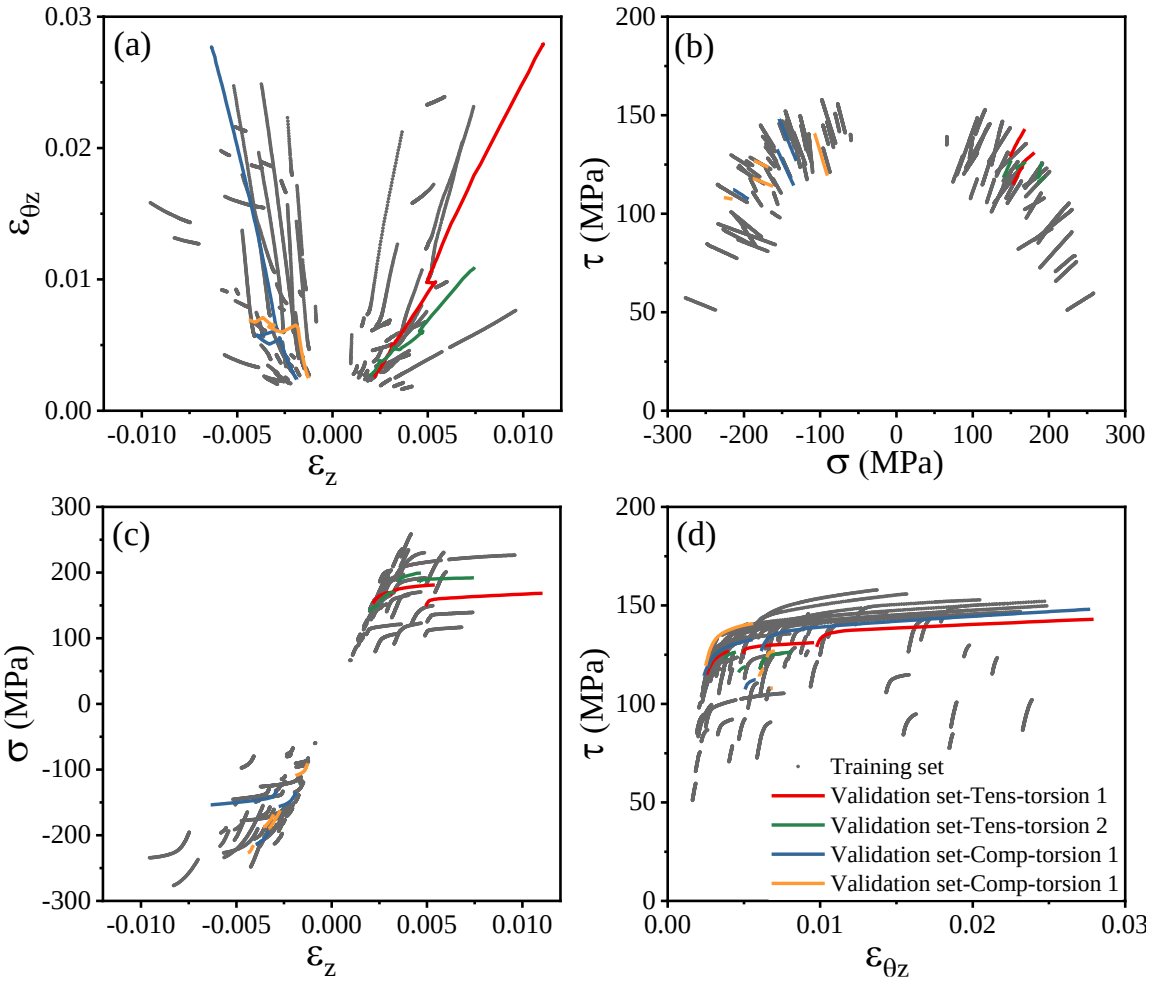


Figure 6.4. Visualisation of the plastic increments composing the training dataset and the validation experiments (a) in the strain space; (b) in the stress space; (c) in axial stress versus axial strain space; (d) in shear stress versus shear strain space.

6.3 Implementation of the Surrogate Models

6.3.1 Training data set

Out of the total fourteen experiments conducted, four of them (two tension-torsion and two compression-torsion) were set aside and stored for validation purposes. The remaining ten experiments, consisting of five tension-torsion and five compression-torsion experiments, formed the training dataset. Figure 6.4 depicts the plastic increments that constitute the training dataset (in grey) and the validation experiments (in different colours). The stress-strain measurements were utilized without additional manipulations, except for necessary adjustments related to the occurrence of large strain increments. In cases where the increments $\Delta\varepsilon_z$ exceeded $6{\cdot}10^{-5}$ and/or $\Delta\varepsilon_{\theta z}$ exceeded $2.5\ 10^{-4}$ an additional data point was generated using linear interpolation. This procedure was implemented to mitigate any inconsistencies in the dataset and to enhance the accuracy of the prediction results.

To differentiate between increments that were purely elastic and those that were elastic-plastic, an additional information was added to the experimental data. This was achieved by keeping track of the change in accumulated plastic strain $\bar{\varepsilon}_n^{pl}$ for each increment. Each increment was then assigned a flag value Y given by

$$Y = \begin{cases} 1 & \Delta\bar{\varepsilon}_n^{pl} \geq 9.10^{-6} \\ 0 & \Delta\bar{\varepsilon}_n^{pl} < 9.10^{-6} \end{cases} \tag{2}$$

with $Y = 1$ corresponding to an elastic-plastic increment and $Y = 0$ corresponding to an elastic increment. The value 9.10^{-6} used in the eqn (2) was determined through trial

and error in an earlier study by evaluating its impact on the accuracy of the classification. It was found that using very high values for the threshold in $\bar{\varepsilon}_n^{pl}$ led to some elastic-plastic increments being incorrectly categorized as elastic. On the other hand, using a threshold that was too low caused some elastic increments to be mistakenly classified as elastic-plastic.

Figure 6.4 visualises the elastic-plastic training dataset after exclusion of the elastic increments flagged with Y=0; this comprises 3718 tension-torsion and 4039 compression-torsion elastic-plastic increments.

6.3.2 Surrogate models

A surrogate constitutive model based on experimental data is developed by utilising feed-forward neural networks (NNs) [20]. The NNs were developed and trained in TensorFlow 2.6 [21]. The proposed surrogate model first separates increments into elastic and elastic-plastic categories using a preliminary classification NN, then uses the equations of elasticity to update the stress vector if the increment is elastic, or a regression neural network if it is elastic-plastic, as shown in Figure 6.5.

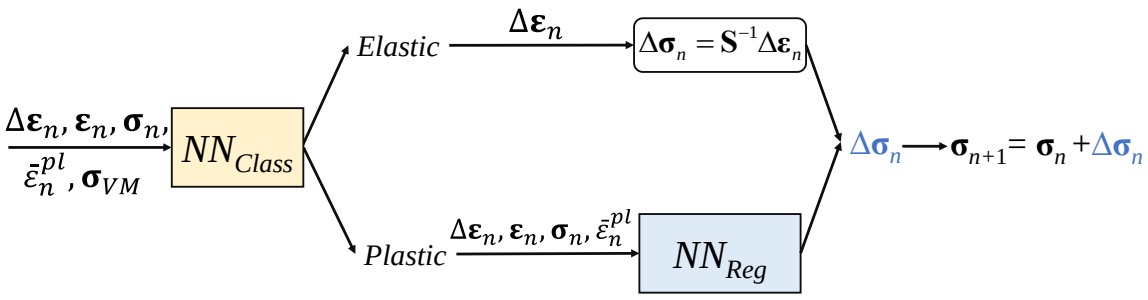


Figure 6.5. Schematic of the surrogate model.

The current strain vector, stress vector, strain increment vector, and stress increment vector are defined as follows:

$$\boldsymbol{\varepsilon}_n = \begin{pmatrix} \varepsilon_z \\ \varepsilon_r = \varepsilon_\theta \\ \varepsilon_{\theta z} \end{pmatrix}; \boldsymbol{\sigma}_n = \begin{pmatrix} \sigma_z \\ \sigma_r = \sigma_\theta = 0 \\ \tau \end{pmatrix}; \Delta\boldsymbol{\varepsilon}_n = \boldsymbol{\varepsilon}_{n+1} - \boldsymbol{\varepsilon}_n; \Delta\boldsymbol{\sigma}_n = \boldsymbol{\sigma}_{n+1} - \boldsymbol{\sigma}_n; \quad (3)$$

where n is a label to identify the current state and n+1 represents the state at the end of the increment being considered.

Considering the relatively small deformations applied to the specimens, it is assumed that additive strain decomposition applies, i.e.

$$\boldsymbol{\varepsilon} = \boldsymbol{\varepsilon}^{el} + \boldsymbol{\varepsilon}^{pl} = \boldsymbol{S}\boldsymbol{\sigma} + \boldsymbol{\varepsilon}^{pl}. \quad (4)$$

The current accumulated von Mises plastic strain is defined as:

$$\begin{aligned} \bar{\varepsilon}_n^{pl} &= \sum_{i=1}^{n} \Delta\bar{\varepsilon}_i^{pl} = \sum_{i=1}^{n} \sqrt{\frac{2}{3}\Delta\boldsymbol{\varepsilon}_i^{pl}\Delta\boldsymbol{\varepsilon}_i^{pl}} \\ &= \sum_{i=1}^{n} \sqrt{\frac{2}{3}\left[\left(\Delta\varepsilon_z^{pl}\right)_i^{\,2} + 8\left(\Delta\varepsilon_{\theta z}^{pl}\right)_i^{\,2} + 2\left(\Delta\varepsilon_r^{pl}\right)_i^{\,2}\right]} \end{aligned} \quad (5)$$

The developed surrogate model distinguishes the tension-torsion and compression-torsion increments simply according to the sign of the current stress and strain values. Once the type of the loading is defined, the classification and regression NNs trained with tension-torsion or compression-torsion experiments carry out the prediction.

As shown in Figure 6.5, the first step consists of a classification exercise to distinguish elastic from elastic-plastic increments.

$$Y = NN_C(\Delta\boldsymbol{\varepsilon}_n, \boldsymbol{\varepsilon}_n, \boldsymbol{\sigma}_n, \bar{\varepsilon}_n^{pl}, \boldsymbol{\sigma}_{VM}) \quad (6)$$

where Y is the flag defined in eqn.(2) ($Y = 1$ corresponding to an elastic-plastic increment and $Y = 0$ corresponding to an elastic increment). $\boldsymbol{\varepsilon}_n, \boldsymbol{\sigma}_n$ represent the current state of stress and strain of the material, $\Delta\boldsymbol{\varepsilon}_n$ denotes the increments in total strain, $\boldsymbol{\sigma}_{VM}$ is the equivalent Von Mises stress and $\bar{\varepsilon}_n^{pl}$ is the accumulated plastic strain. NN_C comprises 2 hidden layers containing 32 neurons each for both tension-torsion and compression-torsion NNs. The inputs were scaled using the minmax() function, ReLU was the chosen activation function for the 2 hidden layers, while sigmoid [22] was used for the output layer. A special dataset was assembled for the classification network, by selecting an equal number of datapoints for elastic and elastic-plastic increments with $Y = 1$ and $Y = 0$; the ratio of training to testing datapoints was set to 90/10. The Binary Cross-Entropy (BCE) was the chosen loss function. The training of the NN was performed by backpropagation using the Adam optimiser [23]; 5,000 and 3,000 epochs with a batch size of 100 and a learning rate of 0.001 were used for the tension-torsion and the compression-torsion classification NNs, respectively. The analysis of the confusion matrix [24] showed that the classification was accurate in 99.97% of the cases.

For increments classified as elastic ($Y = 0$), the stress vector was updated as

$$\Delta\boldsymbol{\sigma}_n = \boldsymbol{S}^{-1}\Delta\boldsymbol{\varepsilon}_n. \tag{7}$$

For elastic-plastic increments, NN_R was used to predict the increment in the stress vector.

$$\Delta\boldsymbol{\sigma}_n = NN_R\left(\Delta\boldsymbol{\varepsilon}_n, \boldsymbol{\varepsilon}_n, \boldsymbol{\sigma}_n, \bar{\varepsilon}_n^{pl}\right). \tag{8}$$

As the material studied is history-dependent, $\boldsymbol{\varepsilon}_n, \boldsymbol{\sigma}_n$ represent the current state of the material while $\bar{\varepsilon}_n^{pl}$ quantifies the effects of the previous history of plastic deformations. After the regression, the increments in the plastic strain vector are calculated as

$$\Delta\boldsymbol{\varepsilon}_n^{pl} = \Delta\boldsymbol{\varepsilon}_n - \boldsymbol{S}\Delta\boldsymbol{\sigma}_n \tag{9}$$

and the new accumulated plastic strain is computed from eqn. (5). The hyperparameters of the network NN_R were decided by a trial and error process. The network had two hidden layers with 128 neurons each, for both the tension-torsion and the compression-torsion regression NNs. All inputs and outputs were scaled by the minmax() function [24], and ReLU [22] was the chosen activation function for all hidden layers. The training dataset was split into two portions, equal to 10% and 90% of the total, which were randomly selected as testing and training data, respectively. The Mean Absolute Error (MAE, [24]) was used as the loss function after a preliminary study. The training of the NN was performed by backpropagation using the Adam optimiser [23], with a number of epochs set to 70,000, a batch size of 100 and a learning rate of 0.001.

6.3.3 Assessment of the accuracy of the surrogate models

The accuracy of the surrogate model was evaluated by creating additional four random loading histories and performing the corresponding experiments. These experiments, which the surrogate models had not seen during training, were conducted using the same method as described earlier.

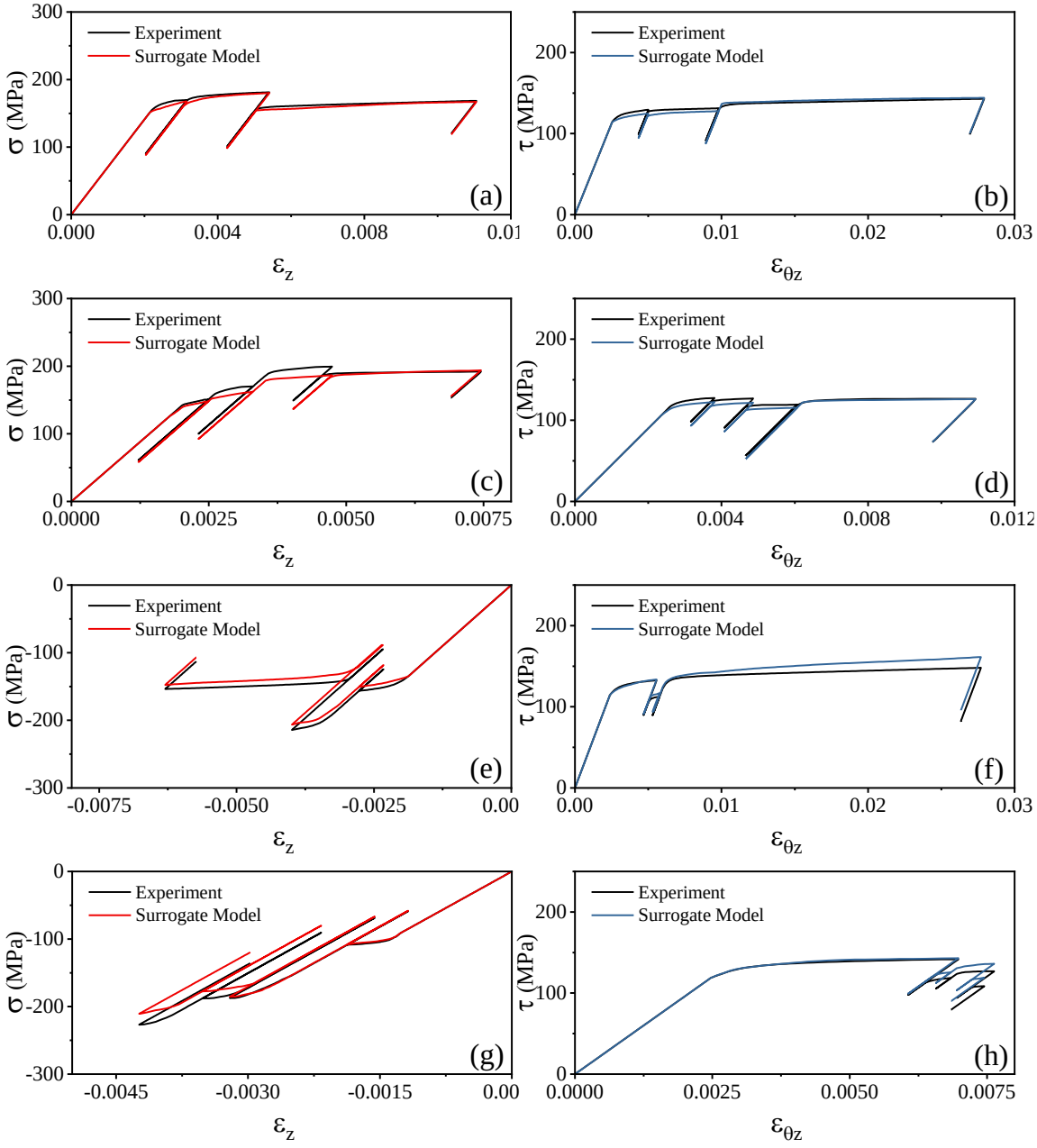


Figure 6.6. Stress-strain histories corresponding to the four validation experiments (two tension-torsion and two compression-torsion) used to assess the surrogate models; (a),(c),(e),(g) normal stress versus normal strain histories and predictions of the surrogate models; (b),(d),(f),(h) shear stress versus shear strain histories and predictions of the surrogate models.

The surrogate model was employed to predict the stress versus strain responses of the unseen random strain histories corresponding to the validation experiments. For each of these validation experiments, a series of strain increments $\Delta\boldsymbol{\varepsilon}_n$, aligned with those in the experiments, were utilized as input for the surrogate models, commencing from the initial stress- and strain-free configuration ($\boldsymbol{\varepsilon}_{n=1} = 0, \boldsymbol{\sigma}_{n=1} = 0$). In each increment, the methodology described in Section 6.3.2 was applied to update the corresponding stress vector and the accumulated plastic strain increments. This enabled the creation of incremental stress predictions corresponding to each of the unseen random strain histories.

6.4 Results and Discussion

To assess the accuracy of the surrogate models, their predictions were compared to the experimental results obtained from the four additional random loading experiments. Figure 6.6 displays the predictions of the surrogate model on stress-strain plots for two tension-torsion and two compression-torsion experiments. The predictions were made by inputting strain increments into the surrogate models and updating the corresponding increments in the stress vector and accumulated plastic strain. Subsequently, the results of these predictions were compared to the ground truth represented by the experimental data.

The model was found to be in good agreement with the combined, non-monotonic, non-proportional strain paths of the validation experiments. Some minor errors were observed in portions of the random strain paths; These are ascribed to the relative

scarcity of training data points in these regions, expected to cause incremental errors in the updates of the stress vector. In tension-torsion experiments, the average absolute error is approximately 3% with peaks of 4-7% in the areas of stress-strain space scarcely populated by the experimental data. On the other hand, in compression-torsion experiments, the average error is measured roughly 5% with peaks of 10-12%. It should be noted that only five tension-torsion and five compression-torsion experiments were used in the training dataset. With an increase in the amount of training experiments, the accuracy of the surrogate model is expected to increase, as demonstrated in the previous research utilising virtual experiments [14].

The prediction results demonstrate that the proposed surrogate model, incorporating the accumulated plastic strain, effectively captures the history-dependent elastic-plastic behaviour of the aluminium alloy employed in this study. However, it is important to note that the surrogate model presented in this study may exhibit reduced accuracy in regions of the input space that are inadequately represented by the training data. To overcome this limitation, one potential approach is to include more coupon-level tests, such as biaxial or triaxial experiments, in order to enhance the diversity of the training dataset. Alternatively, an approach involving physics-informed neural networks [25] could be considered. This would entail adapting the architecture of the surrogate models to encompass appropriate constraints, such as isotropy, symmetry, and pressure-independence of the plastic response, while incorporating supplementary terms into the loss function.

6.5 Conclusions

In this study, combined, non-monotonic, non-proportional experimental data are used to train a surrogate constitutive model able to predict the history-dependent stress path of metallic materials as a function of the current total stresses, total strains, the increments in strain, and the accumulated plastic strain. The goal of this approach is to create data-driven material models that do not rely on any specific theory and are able to predict the material response under arbitrary loading conditions.

The developed model is tested using four unseen experiments. It is demonstrated that the obtained neural network-based model is capable of predicting successfully the stress paths corresponding to the imposed random strain histories. Since the neural network model was trained using experimental data, it does not require the theoretical assumptions and constraints of traditional models. The proposed method may provide researchers with a great opportunity to represent accurately the history-dependent behaviour of engineering materials with potential savings in computational time and significant improvements in terms of accuracy.

6.6 References

[1] Mozaffar M., Bostanabad R., Chen W., Ehmann K., Cao J., and. Bessa M. A, Deep learning predicts path-dependent plasticity, Proceedings of the National Academy of Sciences, 116.52, 26414-26420, 2019.

[2] Ge W. and Tagarielli V.L., A computational framework to establish data-driven constitutive models for time- or path-dependent heterogeneous solids, Scientific reports, 11(15916), 2021.

[3] Ghavamian F.and Simone A., Accelerating multiscale finite element simulations of history-dependent materials using a recurrent neural network, Computer Methods in Applied Mechanics and Engineering, 357 (112594), 2019.

[4] Tasdemir B, Tagarielli V, Pellegrino A. A data-driven model of the yield and strain hardening response of commercially pure titanium in uniaxial stress. Materials & Design, 229(111878), 2023.

[5] Liu Z., Wu C. T. & Koishi M. A deep material network for multiscale topology learning and accelerated nonlinear modeling of heterogeneous materials. Comput. Methods Appl. Mech. Eng. 345, 1138–1168, 2019.

[6] Huang D., Fuhg J. N., Weißenfels C. & Wriggers P. A machine learning based plasticity model using proper orthogonal decomposition. Comput. Methods Appl. Mech. Eng. 365, 113008,2020.

[7] Jang D. P., Fazily P. & Yoon J. W. Machine learning-based constitutive model for J-2 plasticity. Int. J. Plast. 138, 102919,2021.

[8] Ghaboussi J. & Sidarta D. E. New nested adaptive neural networks (NANN) for constitutive modeling. Comput. Geotech. 22(1), 29–52,1998.

[9] Ghaboussi J., Pecknold D. A., Zhang M. & Haj-Ali R. M. Autoprogressive training of neural network constitutive models. Int. J. Numer. Methods Eng. 42(1), 105–126, 1998.

[10] Li X., Roth C. C., & Mohr D. Machine-learning based temperature-and rate-dependent plasticity model: Application to analysis of fracture experiments on DP steel. International Journal of Plasticity, 118, 320-344,2019.

[11] Li X., Roth C. C., Bonatti C., & Mohr D. Counterexample-trained neural network model of rate and temperature dependent hardening with dynamic strain aging. International Journal of Plasticity, 151, 103218, 2022.

[12] Cai R., Lin H., Cheng P., Zhang Z., Wang K., Peng Y., ... & Ahzi, S. Investigation on dynamic strength of 3D-printed continuous ramie fiber reinforced biocomposites at

various strain rates using machine learning methods. Polymer Composites, 43(8), 5235-5249, 2022.

[13] Hamel C. M., Long K. N., & Kramer S. L. Calibrating constitutive models with full-field data via physics informed neural networks. Strain, 59(2), e12431, 2023.

[14] Tasdemir B, Pellegrino A, Tagarielli V. A strategy to formulate data-driven constitutive models from random multiaxial experiments. Scientific reports, 12(22248), 2022.

[15] Bache M. R., & Evans,W. J. Tension and torsion fatigue testing of a near-alpha titanium alloy. International journal of fatigue, 14(5), 331-337, 1992.

[16] Portier L., Calloch S., Marquis D., & Geyer P. (2000). Ratchetting under tension–torsion loadings: experiments and modelling. International journal of plasticity, 16(3-4), 303-335, 2000.

[17] Papasidero J., Doquet V., & Mohr D. Determination of the effect of stress state on the onset of ductile fracture through tension-torsion experiments. Experimental Mechanics, 54, 137-151, 2014.

[18] Bache,M. R., Evans W. J., & Davies H. M. Electron back scattered diffraction (EBSD) analysis of quasi-cleavage and hydrogen induced fractures under cyclic and dwell loading in titanium alloys. Journal of Materials Science, 32, 3435-3442, 1997.

[19] Young, W. C. & Budynas, R. G. Roark's Formulas for Stress and Strain 709–742 (McGraw-Hill, 2012).

[20] Goodfellow I., Bengio Y., and Courville A., Deep Learning, The M.I.T. Press, 2016.

[21] Singh P., Manure A. Introduction to TensorFlow 2.0. In: Learn TensorFlow 2.0. Apress, Berkeley, CA., 1-24, 2020.

[22] Nwankpa C., Ijomah W., Gachagan A., and Marshall S., Activation functions: Comparison of trends in practice and research for deep learning, arXiv preprint arXiv:1811.03378, 2018.

[23] Kingma D. P. and Ba J.L., Adam: A method for stochastic optimization, ICLR 2015, 1412, 6980, 2014.

[24] Pedregosa F., et.al. Scikit-learn: Machine Learning in Python, the Journal of Machine Learning Research, 12, 2825-2830, 2011.

[25] Karniadakis G. E. et al. Physics-informed machine learning. Nat. Rev. Phys. 3(6), 422–440,2021.

CHAPTER 7

CONCLUSIONS

This section serves as a comprehensive summary and provides the concluding remarks of the presented integrated format PhD thesis.

The thesis comprises four main chapters, each constituting an independent self-contained scientific paper. The content included within these four papers is presented below as a comprehensive summary.

Paper 1

- Data from quasi-static and high strain rate compression experiments are used to train neural network models capable of predicting the stress-strain response of a polymer syntactic foam as a function of stress, temperature and strain rate.

- The developed models are tested using unseen experimental loading cases. It is demonstrated that the obtained neural network models can successfully predict the stress-strain responses obtained under unseen temperature and strain rate combinations.

Paper 2

- This paper proposes a strategy to implement data-driven constitutive models for the uniaxial cyclic response of commercially pure titanium.

- Seven experiments are used to train a surrogate constitutive model able to predict the material response to random cyclic strain histories in uniaxial stress.

- The complex yielding and strain hardening of pure titanium were captured correctly by including in the surrogate model specific inputs. The developed surrogate model is tested using unseen experiments.

- The performance of the surrogate model was found to largely exceed that of an established theoretical model for the cyclic hardening of metals.

Paper 3

- This paper proposes a methodology to develop data-driven surrogate constitutive models which do not rely on any constitutive theory and are informed exclusively by the results of carefully designed random non-proportional, non-monotonic multiaxial virtual tests.

- The accuracy of the developed surrogate models is validated using unseen random loading histories.

- A strategy is outlined for performing cost-effective experiments on the material of interest and precisely capturing its response using surrogate models built upon compact feed-forward neural networks. The methodology also encompasses the design of appropriate specimens and of suitable random strain histories.

Paper 4

- The methodology devised in Paper 3 is applied to real experimental data in this paper.

- Data from combined, non-monotonic, non-proportional experiments are used to train a surrogate constitutive model able to predict the history-dependent stress path of

metallic materials as a function of the current total stresses, strains, the increments in strain, and the accumulated plastic strain.

- A data-driven material model that does not rely on any particular theory and is able to predict the material response under arbitrary loading conditions is proposed.
- The developed model is tested using four unseen experiments.
- It is demonstrated that the obtained neural network model is capable of predicting successfully the stress paths corresponding to random imposed strain histories. Since the neural network model was trained using experimental data, it eliminates the need for the theoretical assumptions and constraints of traditional models.

In summary, within this PhD research, material models for various categories of materials and loading modes have been formulated by employing machine learning techniques. A novel approach is introduced to data analytics and materials constitutive modelling based on machine learning techniques fed with actual experimental data. The adoption of data-based machine learning-driven models obtained from mechanical loading experiments allows for the accurate and computationally efficient prediction of the mechanical behaviour of materials. Accurate predictions of the mechanical behaviour of materials have been obtained while concurrently reducing or eliminating the reliance on extensive theoretical assumptions.